PRINTED MICROSCALE MONO-CRYSTALLINE SILICON ON FLEXIBLE SUBSTRATES FOR PHOTOVOLTAIC, STRAIN SENSORS, AND NEURAL INTERFACE APPLICATIONS

BY

KI JUN YU

DISSERTATION

Submitted in partial fulfillment of the requirements
for the degree of Doctor of Philosophy in Electrical and Computer Engineering
in the Graduate College of the
University of Illinois at Urbana-Champaign, 2015

Urbana, Illinois

Doctoral Committee:

Professor John A. Rogers, Chair
Professor Joseph W. Lyding
Professor Xiuling Li
Associate Professor Gang L. Liu

ABSTRACT

In recent years, research in flexible electronic systems has increased due to its potential to create and manipulate new classes of applications (e.g., foldable and flexible display, flexible photovoltaic, epidermal electronics, and other systems) that can be integrated outside of conventional wafer-based electronics. With suitable choice of materials and design strategies, inorganic semiconductors (e.g., Si and GaAs) can be used on unconventional substrates for mechanical flexibility and high electrical performance. This dissertation presents the fabrication of mono-crystalline Si electronics by using top-down approaches. We describe five related topics of ultra-thin Si electronics which involve forming structures and assembling them by structured or non-structured elastomeric stamps or bulk wafer etching techniques. Furthermore, this dissertation demonstrates a strategy in which modules consist of large-scale arrays of interconnected high-performance ultra-thin Si electronics that are mechanically flexible, stretchable, and semitransparent, along with in-depth studies of their electrical and mechanical properties and applications.

To my parents and family

ACKNOWLEDGMENTS

First of all, I would like to acknowledge my research advisor, Prof. John A. Rogers, for his support and guidance throughout my graduate study as well as my senior year during undergraduate study. He has taught me not only great knowledge and techniques during the research work but also how to wisely deal with my life. His vision and guidance changed my life. I always appreciate his dedication, enthusiasm, and work ethic in bringing scientific solutions to society. I am very proud to be his student, and I will keep that honor for the rest of my life. I am also honored by the Department of Electrical and Computer Engineering at the University of Illinois Urbana-Champaign for giving me the opportunity to pursue my B.S., M.S. and Ph.D. studies. I would also like to express my sincere gratitude to my doctoral committee, Professor Xiuling Li, Professor Joseph W. Lyding, and Professor Logan G. Liu, for providing me with insightful comments and constructive criticisms that inspired my growth as a researcher. I thank my current group mates Dr. Bong Hoon Kim, Dr. Jung Woo Lee, Dr. Kyung-in Jang, Dr. Ahyun Koh, Dr. Daeshik Kang, Dr. Gun Chul Shin, Dr. Hui Fang, Dr. Matt Phar, Sang Min Won, Yoon Kyeong Lee, and all of my colleagues for providing good ideas and inspiration. I also thank my former group members and many friends at UIUC. Also, my gratitude to former and current undergraduate students, Woo Jung Shin, Hyo Jung Shim, Seul-hee Jung, Jae-suk Park, Byung Gaun Lee, Nam Heon Kim, Kyung Jin Seo, Hee Nam Lee, Jin Hyuk Choi, and Seowoo Park.

During my Ph.D. study, I worked with many outside collaborators from the University of Pennsylvania, Duke University, and New York University. I would like to express my appreciation to Prof. Brian Litt, Prof. Jonathan Viventi, Prof. Bijan Persaran, Ken Chiang, Charles Wang, Amy Osborne, Duygu Kuzum, and Michael Trumpis.

My sincere gratitude goes to my parents, Tak Hi Yu and Jeom Soon Yang, sister Ka Young Yu, and brother Ki Kwan Yu, for their endless love and support during my entire life.

Lastly, I would like to thank my wife, Yu Ri Lee, for her understanding, friendship, and support and for being a wonderful mother to our treasure. I always think it was destiny that I and Yu Ri met in Urbana-Champaign, and all her love and support brought me to the final destination of my Ph.D. journey. I am also very happy that our daughter, Caroline Ha-Eun Yu, came in to our life and brought us endless joy and happiness.

TABLE OF CONTENTS

Chapter 1. INTRODUCTION

1.1 Research Motivation

During the last half century, aggressive research in the Si electronics industry has focused on improving performance and cost, and developing better mechanical properties, in which lightweight, flexible substrates facilitate system transport and use [1-14]. These efforts have created substantial interest in materials and fabrication techniques that enable electronic devices to be formed, in scalable ways, directly on flexible substrates such as metal foils or ideally on thin sheets of plastic [15-21]. Flexible electronics can offer various advantages such as intimate, conformal contacts to complex curvilinear surfaces and great endurance to high levels of strain compared to rigid form of electronics. Flexible electronic devices fabricated with lightweight and low-cost plastic substrates have provided great potential in unconventional electronic application areas, such as RFID tag [22], wearable electronics, flexible displays [23, 24], and health monitoring system. Inorganic semiconductors are widely used as active materials for electronic devices. Many electronic applications based on inorganic materials provide superior performance to that of organic materials, such as high field-effect mobility, lifetime, and long-term stability under harsh environments [25-26]. Especially, single-crystal Si is the most famous and well-proven material for recent electronic devices. Substantial efforts were made for the fabrication of Si flexible electronics recently. However, the main challenge of the device fabrication is that the characteristics of the device performance and the large area requirements often induce limitations on materials choices and fabrication processes. For example, most polymer substrates cannot be compatible with high-temperature fabrication, which always requires inorganic semiconducting materials. With suitable choices of materials, design, and integrating strategies, inorganic semiconductor, especially ultra-thin Si, can be utilized for active components with high electrical

performance, and assembled with flexible formats. The deterministic transfer printing technique or various Si etching techniques enable this outcome where the single-crystalline semiconductor active components retain their original properties, thereby offering a flexible electronic system with performance comparable to or better than those of conventional inorganic or organic based electronics. Following this current research trend, my research group reported Si electronic devices with high performance, reducing the usage of Si, and mechanical flexibility and stretchability and their applications. This thesis will explore a combination of theoretical and experimental studies for the development, characterization and optimization of Si electronic applications using large-area electronics fabrication techniques. The overall theme of my research is to fabricate unconventional electronics using ultra-thin single-crystalline Si for various electronic applications and to use elastomeric stamps for the assembly. In particular, one of the goals of my thesis research is to study and develop new, versatile form factors which can be used as active layers in macroelectronic type devices, and to demonstrate their applications. The overall theme of my research is to fabricate semiconductor microstructures for various electronic applications and to use elastomeric stamps for the assembly and fabrication of unusual electronics by top-down approaches. This dissertation will explore various flexible electronic devices such as photovoltaics, strain sensors, and neural monitoring sensors all based on ultra-thin single-crystalline Si as an active material.

1.2 Overview of Thesis

Chapter 2 describes more recent work on the fabrication of robust, high-quality Si form factors by optimizing processing steps. These detailed systematic studies enabled new Si form factors (ribbons, bars and platelets), which developed into a new Si solar cell technology. This

chapter also presents the use of these optimized Si bars as active microcell photovoltaic devices. Their spatial dimensions and manipulability via elastomeric stamps lead to the production of unconventional Si PV modules that cannot be obtained using wafer-based approaches.

Chapter 3 describes the use of Si microcells to produce PV modules with high-voltage outputs for applications in wearable PV technologies. The details of the doping schemes and interconnection design are investigated, and detailed analysis of the electrical characteristics and response of these systems during flexing and bending experiments are presented.

Chapter 4 presents current work on the fabrication of Si PV modules with mechanically stretchable designs. The details of the fabrication, assembly and electrical characterization of these systems are investigated. Detailed finite element modeling leads to predictions of optimal layouts and designs for stretchable and bendable PV technologies.

Chapter 5 describes current work on the fabrication of ultra-thin (~3 μm thick) Si PV modules, patterned with light-trapping structures, with mechanically flexible designs. The details of the fabrication, assembly and electrical characterization of these systems are investigated.

Chapter 6 describes printed assemblies of ultrathin single-crystalline Si with the multiplexed addressing capability. The details of the fabrication, assembly, and electrical characterization of the system are investigated.

Chapter 7 describes a Si-based bioresorbable electronics technology for high performance electrophysiological recording from the cortical surface and the subgaleal space, *in vivo*, extending to arrays of active sensors with multiplexed addressing capabilities. The details of the fabrication, assembly, and electrical characterization of the system are investigated. Also, *in vitro* and *in vivo* experiments are summarized.

Chapter 8 describes a new type of neural monitoring device that is capable of high-resolution capacitive neural interfaces over a large area for chronic recording *in vivo*. The details of the fabrication, assembly, and electrical characterization of the system are investigated.

1.3 References

[1] S. Lacour, J. Jones, S. Wagner, Teng Li, and Zhigang Suo, Proceedings of the IEEE **93**, 1459 (2005).

[2] D. -H. Kim, J. -H. Ahn, W. M. Choi, H. -S. Kim, T. -H. Kim, J. Song, Y. Y. Huang, Z. Liu, C. Lu, and J. A. Rogers, Science **320**, 507 (2008).

[3] Y. Sun and J. A. Rogers, Advanced Materials Weinheim, Germany **19**, 1897 (2007).

[4] M. Wu *et al.*, IEEE Transactions on Electron Devices **49**, 1993 (2002).

[5] M. C. McAlpine *et al*., Nano Letter **3**, 1531 (2003).

[6] D. V. Talapin and C. B. Murray, Science **86**, 310 (2005).

[7] H. O. Jacobs *et al*., Science **296**, 323 (2002).

[8] H.-C. Yuan *et al.*, Journal of Applied Physics 100, 100, 013708 (2006).

[9] J.-H. Ahn *et al*., Science **314**, 1754 (2006).

[10] T. Serikawa *et al*., Japanese Journal of Applied Physics **39**, L393 (2000).

[11] D.-H. Kim *et al*., Science **333**, 838 (2011).

[12] D.-H. Kim *et al*., Small **5**, 2841 (2009).

[13] J. Viventi *et al*., Science Translational Medicine **2**, 24ra22 (2010).

[14] J. Viventi *et al.*, Nature Neuroscience **14**, 1599 (2011).

[15] R. H. Reuss *et al*., Proceedings of the IEEE **93**, 1239 (2005).

[16] R. H. Reuss, D. G. Hopper, and J.-G. Park, MRS Bulletin **31**, 447 (2006).

[17] J. A. Rogers *et al*., Proceedings of the National Academy of Sciences **98**, 4835 (2001).

[18] G. H. Gelinck *et al*., Nature Materials **3**,106 (2004).

[19] T. Someya *et al*., IEEE Transactions on Electron Devices **52**, 2502 (2005).

[20] T. Someya *et al*., Proceedings of the National Academy of Sciences **102**, 12321 (2005).

[21] T. Someya *et al*., Proceedings of the National Academy of Sciences **101**, 9966 (2004).

[22] Y. Wantanbe and K. Kudo, Applied Physics Letter **87**, 223505 (2001).

[23] S. R. Forrest, Nature **428**, 911 (2004).

[24] H. Sirringhaus, N. Tessler, and R. H. Friend, Science **280**, 1741 (1998).

[25] Y. Amin *et al*., Progress in Electromagnetics Research **130**, 15 (2007).

[26] H. Sirringhaus, N. Tessler, and R. H. Friend, Science **280**, 1741 (1998).

Chapter 2. ULTRATHIN FLEXIBLE SI PV

2.1 Introduction

Single-crystal Si represents the dominant cell material for PV devices. The current trend in Si PVs is to reduce the amount of Si usage, because the use of high-quality Si wafers contributes a substantial fraction (~ 50 %) to the overall cost of mono-crystalline Si solar modules. Therefore, there is significant interest in reducing the thickness of conventional 'bulk' Si solar cells. For example, current bulk Si devices have an average thickness of 300 μm and recently various attempts have been demonstrated that reduce this thickness to 150 μm; however, it is impractical to handle and process wafers in this thickness range using conventional fabrication strategies [1]. Current research in Si photovoltaic devices focuses on developing thin film PV devices, preferably from low-cost materials or processing methods [1, 2]. We find a way to reduce the cost of Si solar cells and enable the fabrication of mechanically flexible solar arrays that are semitransparent and lightweight by using a top-down approach and transfer printing techniques [3- 5].

2.2 Experimental

For instance, implementing the processing procedures depicted in Figure 2.1 (a) [3], begins with a p-type (111) Czochralski Si wafer (3 inch diameter, 1–10 Ω-cm, 450 mm thickness, Virginia Semiconductor) deposited with a layer of SiO_2 (600 nm) formed by plasma-enhanced chemical vapor deposition (PlasmaTherm SLR). The SiO_2 was lithographically patterned to expose regions of the Si in narrow parallel stripes. Inductively coupled plasma reactive-ion etching (STS ICP-RIE) formed trench structures in the Si, with experimentally optimized typical depths of 15–20 μm,

widths of 50 μm, and length of 1.55 mm. Selective doping of emitter and bottom contact areas used solid-state sources of boron (BN-1250, Saint Gobain) and phosphorus (PH-1000N, Saint Gobain) at 1000 °C under N_2 atmosphere for 30 min (boron) and 10 min (phosphorus). Protecting the top surfaces and sidewalls with a bilayer of SiO_2/Si_3N_4 mask, KOH solution etches Si <110> much faster than the other directions, and fronts proceed in anisotropic horizontal fashion until they meet to complete the undercut and release freestanding single-crystal Si. Boron solid-state source doping performed repeatedly at the exposed bottom side after KOH anisotropic etching [6] created a lateral p-n junction. Completely KOH etched micro-bar cells can be selectively picked up with a soft elastomeric polydimethylsiloxane (PDMS) stamp, then printed onto a glass substrate using photo-cured polymer (NOA61, Norland Product Inc.) to serve as a planarizing layer and as an adhesive layer for the transfer printing process. Figure 2.1 (b) gives the lateral dimension of an individual microcell. An individual cell (L = 1.55mm) consists of phosphorus-doped (L_{n+} = 1.4mm), boron-doped (L_{p+} = 0.1mm), and intrinsic regions respectively.

2.3 Basic Theory of Solar Cells

The basic theory [7, 8] of any solar cell is that when it is illuminated with photons with energy hv greater than E_g, the band gap of a material, the photon is absorbed and causes electron-hole pairs (EHPs) to be generated. The separation of these charge carriers is driven towards the end of the contacts by the built-in spatial asymmetry. This separation of charge gives rise to an open circuit voltage in the case of an open circuit, and generation of a photocurrent in a short circuit. When the load is connected to an external circuit, power output can be generated through the load.

The efficiency (η) and the fill factor (FF) are parameters that show the performance of a

solar cell. The higher these two values, the better the cell performance. The efficiency of the solar cells is expressed as

$$\eta = \frac{J_m V_m}{P_s}$$

and the fill factor is

$$FF = \frac{J_m V_m}{J_{sc} V_{oc}}$$

where J_m and V_m are the current density and voltage at the maximum power point ($J_m V_m = P_m$, the maximum power), P_s is the incident light power density, J_{sc} is the short circuit current density, and V_{oc} is the open circuit voltage. The short circuit current can be defined as

$$J_{sc} = J_0(\exp\left(\frac{qv}{nkT}\right) - 1)$$

V_{oc} also can be determined as

$$V_{oc} = \frac{nkT}{q}\ln(\frac{J_{sc}}{J_D} + 1)$$

One of the unique characteristics of these solar cells is that there is sidewall emitter doping for an increased junction area, and the basic idea for the inverse design is to increase the area even more by reducing shadowing by metal interconnects, which will improve the cell performance.

2.4 Results and Discussion

The J-V measurements were made using a DC source meter (model 2400, Keithley), and a 1000W full-spectrum solar simulator (model 91192, Oriel). The power of the light from the solar simulator was measured with a broadband detector (model 70268, Newport) and a power meter

(model 70260, Newport). 500 data points were collected by sweeping from -0.5V and +0.6V, and these data points were used to calculate the efficiency and fill factor values. J-V measurements were done under AM 1.5D illumination. The efficiency of the p-n junction design ranged from 6 to 8%. Figure 2.2 (a) illustrates the initial light illumination test results, where the best efficiency is 9.5% (Figure 2.2 (b)) and the maximum fill factor is 0.72 (Figure 2.2 (c)), and Figure 2.2 (b) shows the many-cell efficiency data. This result shows that ultrathin Si PV gives higher volumetric efficiency than conventional Si since the maximum reported efficiency of conventional rigid base solar cells is 25.9%, but the material thickness is around 250~500 μm.

2.5 Conclusion

The micro-scale solar module presented here may create new possibilities for monocrystalline Si photovoltaics, namely thin, lightweight construction, mechanical flexibility, semitransparency or the unusual optical properties of the μ-CPV designs. In most cases, we chose materials that have the potential for long lifetime and high reliability. This type of solar cell can be applicable to transparent power sources. Low-cost processing for high-performance μ-cell and module fabrication, together with other means to reduce cost or increase performance, are important areas for further work.

2.6 Figures

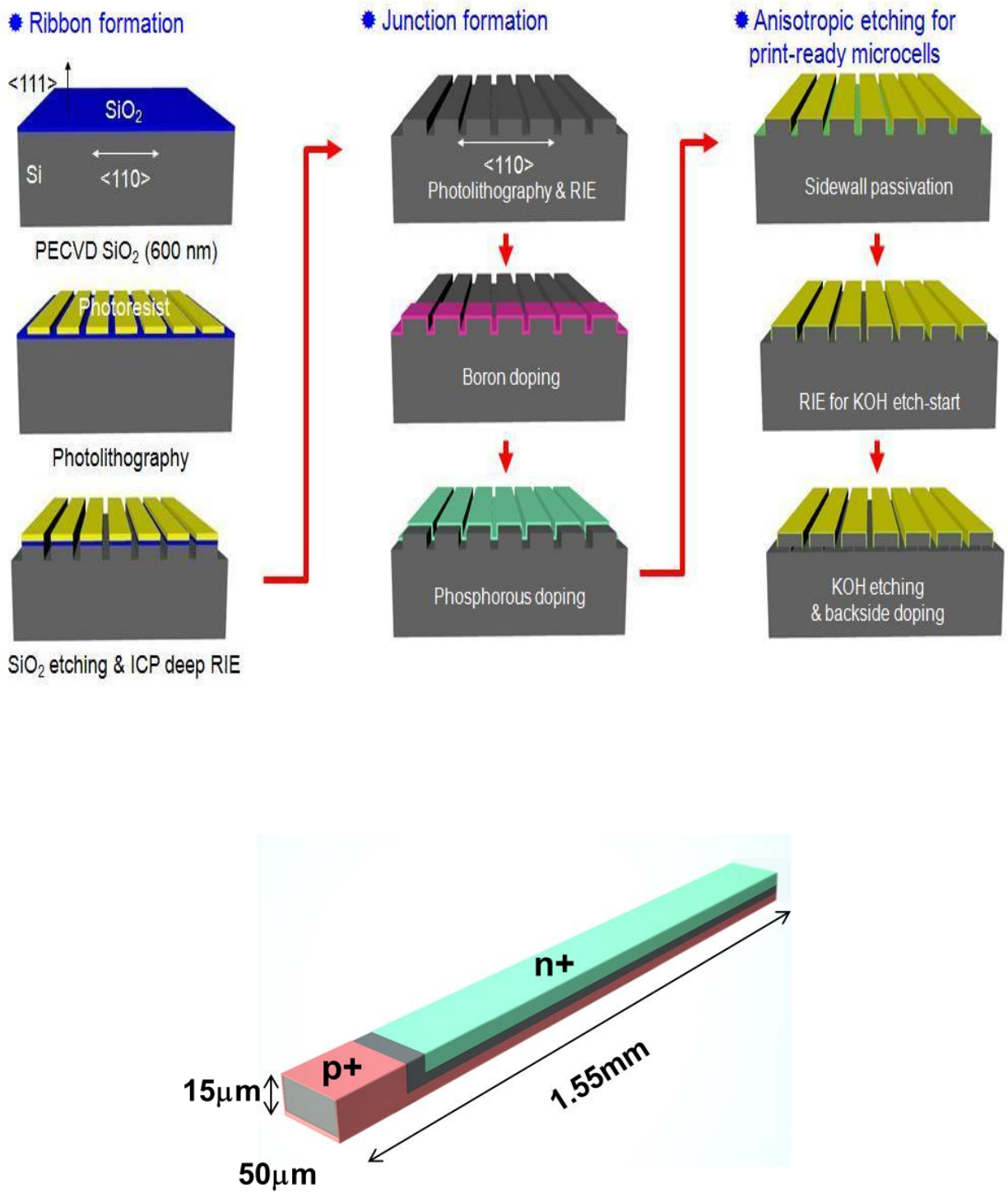

Figure 2.1 (a) Si microcells fabrication process. (b) Lateral dimension of Si microcell.

a)

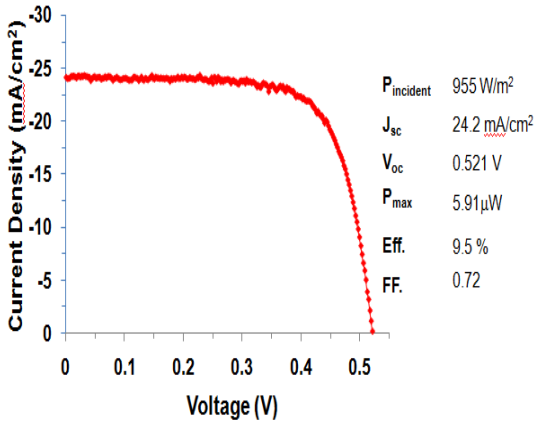

b)

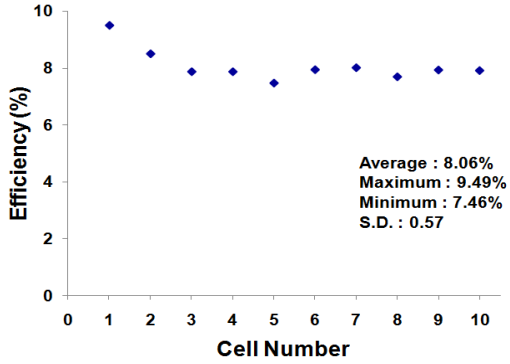

c)

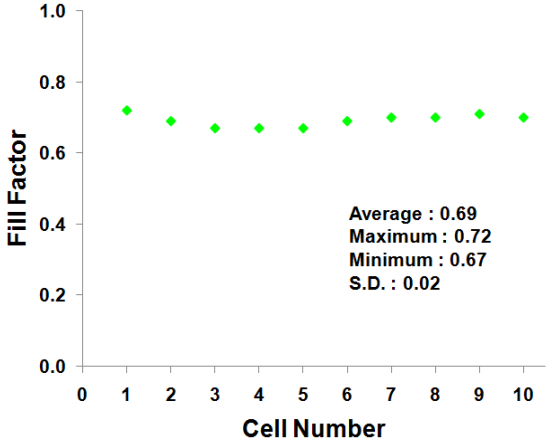

Figure 2.2 (a) J-V data from an individual cell with the microcell design. (b) Statistical data of efficiency measurement. (c) Statistical data of calculated fill factor.

2.7 References

[1] L. L. Kazmerski, Journal of Electron Spectroscopy **150**, 105 (2006).

[2] R. B. Bergmann, Applied Physics A **69**, 187 (1999).

[3] J. Yoon *et al*., Nature Materials **7**, 907 (2008).

[4] R. H. Reuss et al., Proceedings of the IEEE **93**, 1239 (2005).

[5] J. A. Rogers et al., Proceedings of the National Academy of Sciences **98**, 4835 (2001).

[6] A. J. Baca *et al*., Advanced Functional Materials **17**, 3051 (2007).

[7] J. Nelson, *The Physics of Solar Cells*, (Imperial College Press, 2003) pp. 7-15.

[8] B.G. Streetman and S.K. Banerjee, *Solid State Electronic Devices*, Prentice Hall, 2006. pp. 398-405.

Chapter 3. MECHANICALLY STRETCHABLE SI PV

3.1 Introduction

This chapter describes the design, fabrication and electrical characterization of a type of Si solar cell module that uses aligned arrays of ultrathin (10 μm) Si microcells fabricated by patterning and anisotropic etching of bulk Si (111) wafers. Stretchable solar modules that incorporate Si microcells show good electrical properties with solar cell efficiencies as high as 8% for an individual Si microcell and 8% for arrays of microcells connected in parallel. We also present an analytical model used to predict the levels of strain experienced in the critical layers of these systems and the corresponding I-V characteristics under mechanical deformation. These results may represent important steps toward a low-cost approach to large-area and wearable solar applications.

Conventional photovoltaic modules and devices typically exist in planar layouts on flat rigid surfaces such as expensive semiconductor wafers and fragile high-quality glass plates [1, 2]. Ease of fabrication is the primary reason for implementing these substrates and configurations for solar cell fabrication. Advantages of these substrates include high thermal stability and high performance due to the high quality and control over the interfaces of the individual layers. The disadvantages of these substrate configurations include their unattractive mechanical properties and their bulky layout which make these systems incompatible for use in rugged environments or in situations that require curvilinear surfaces or other niche applications. Solar cells formed on thin flexible plastic substrates [3, 4], ultrathin Si strips [5], and metal foil substrates [6] are all possible alternatives that alleviate some the aforementioned issues, but they can only be applied on a narrow class of surfaces, thereby limiting application possibilities.

Stretchable photovoltaics represent a new and much more technically complex class of solar cells in comparison to solar modules that offer only simple bendability. A stretchable solar module is defined as a module that can accommodate high levels of strain (>>1%) without mechanical failure or significant changes to its electro-optical properties. This requirement is critical for modules that operate on and are conformally wrapped around complex curvilinear surfaces such as structural components of an aircraft or a warship, military war fighter uniforms and tents, mobile devices and enclosures, and others.

Here we introduce design concepts for stretchable photovoltaic modules that use ultrathin Si microcells fabricated from bulk wafers, in mechanically neutral plane mesh layouts integrated on elastomeric substrates. These layouts and systems were inspired by our recent work on stretchable electronic circuits [7-9]. Experimental and theoretical studies of their electrical and mechanical properties illustrate their mode of operation and provide guidelines for materials choices for the fabrication of this type of module.

3.2 Experimental

Si microcell fabrication processes begin with a p-type (111) Czochralski Si wafer (3 inch diameter, 1-10 Ω cm), 450 μm thick (Virginia Semiconductor), that was coated with a layer of SiO_2 (600 nm) formed by plasma-enhanced chemical vapor deposition. Inductively coupled plasma reactive-ion etching was used to form trench structures of 10 μm thickness. Selective area doping of emitter and bottom contact area was conducted using solid-state sources of boron (BN-1250, Saint Gobain) and phosphorus (PH-1000N, Saint Gobain) at 1,000 ℃ under N_2 atmosphere for 30 min (boron) and 15 min (phosphorus) with a doping resist mask for boron and phosphorous

doping. Anisotropic etching in KOH followed by back surface field formation (boron doping at 1000 ℃ for 10min) completes the processing.

Stretching tests were performed with automated assemblies that can apply tensile or compressive strains in x, y, or diagonal directions. Light and dark I–V measurements of μ-cells were carried out at room temperature using a dc source meter (model; 2400, Keithley) operated by LabVIEW5, and a 1,000W full-spectrum solar simulator (Oriel model 91192, 100 mm source diameter, ±4 collimation) equipped with AM 0 and AM 1.5 direct filters. The input power of light from the solar simulator was measured with a power meter (Newport model 70260). The solar-energy conversion efficiencies and related calculations reported here rely on the spatial dimensions of the microcells rather than the surface area of the test structure and do not explicitly account for the light entering the edges of the cells. In some measurements light piping contributed a significant amount of photocurrent. This is far more important for individual devices than for arrays.

Figure 3.1 shows a schematic representation of the steps for the fabrication of stretchable solar cell modules, which consist of transfer printing a 6 × 6 array of 10 μm thick microcells onto a glass slide coated with a sacrificial layer of PMMA (~200 nm) and a 12 μm thick photocurable NOA (NOA61, Norland Product Inc.) layer as shown in Figure 3.1 (a). Metal contacts were formed via sputtering Cr/Au (5nm/500nm) followed by etch back in the corresponding etchants. A single row contains 36 microcells connected in parallel. The modules are then encapsulated by a second layer of NOA (12 μm) (i.e. neutral mechanical plane) which protects the microcells during mechanical deformation by reducing the degree of strain of the most brittle materials in the system (i.e., Si and the metal). A mesh design composed of islands (i.e., microcell area) interconnected by thin rectangular or s-shaped ribbons (bridges) is then etched by oxygen RIE followed by releasing

the solar modules from the glass substrate by dissolving the PMMA in a solution of acetone with ultrasonication. A PDMS stamp is used to retrieve the released module, and a thin layer of SiO_2 (300 nm) and Cr (3 nm) is selectively deposited via electron beam evaporation through a shadow mask, which exposes the backside of the island area while protecting the interconnected ribbons from the incoming flux. Transfer printing the fabricated module onto a biaxially pre-strained PDMS substrate upon release leads to the formation of pop-up structures that can accommodate mechanical deformations from all directions. Improved adhesion to the PDMS slab is enhanced by selective deposition of SiO_2 on the underside of the solar module. We recently demonstrated this approach for applications in stretchable electronic circuit design. However, in this study the layouts, materials and the thicknesses (i.e., 22 μm) are different, leading to different mechanical properties and considerations for materials choice. Modules fabricated in this way can be stretched and compressed up to 30 % without mechanical failure.

Figure 3.2 (a) depicts scanning electron and optical micrographs of the completed micro solar cell fabrics. As depicted in Figure 3.2 (b) upon releasing the strain of the PDMS substrate, the islands (Si active area) remain rigidly bonded to the PDMS substrate while the interconnect ribbons move up and down and in the out-plane direction forming arc-shaped ribbon structures.

3.3 Results and Discussion

These arc-shaped ribbons stretch and compress because they are not bonded to the PDMS substrate, and move in a way that accommodates applied mechanical deformations. Only weak van der Waals forces are present between the bridge and the strained PDMS slab. Due to the flexible and stretchable nature of these fabrics, they can be conformally wrapped around curvilinear surfaces without significant degradation to their mechanical and or electrical properties,

as will be described later. Figure 3.2 (c) depicts the completed stretchable module consisting of 36 microcells wrapped around a glass tube with a radius of curvature of 2 mm. Solar fabrics with arc-shaped ribbons can accommodate strain levels as high as 15 % without failure. Strain levels > 15% lead to mechanical failure at the points where the ribbons meet the islands for stretchable fabrics with arc-shaped ribbons. More advanced designs that contain narrow interconnect and serpentine geometries were fabricated to increase the deformation level tolerance, and to achieve the targeted stretching degree (i.e. 30%). Figure 3.3 (a) shows SEM and optical images of stretchable fabrics composed of s-shaped interconnect ribbons.

A representative J-V curve for a single Si microcell on a planar rigid substrate is depicted in Figure 3.4 (a). Single devices exhibit efficiencies of 7-8%, V_{oc} of 0.51V and a fill factor of 0.68. Increasing the cell thickness, adding light-trapping schemes or antireflection coatings can enhance these metrics to levels comparable to those displayed by conventional solar cells. Inset is an optical micrograph of an array of Si microcells, with a length of 600 μm, width of 45 μm and thickness of 10 μm transfer printed onto NOA/PMMA/glass slide substrate. Metallization to these microcells was accomplished by sputtering Cr/Au interconnects designed to metallically interconnect the string of cells in parallel. Simple modifications to this layout can also string the cells in series for the fabrication of modules with high voltage outputs. Figure 3.4 (b) depicts a single-pixel array of 6 microcells in parallel interconnection. The result shows an efficiency of 7.5% and V_{oc} of 0.50V. In either case of single microcell or interconnected 6 microcells, the performance does not show noticeable degradation.

To predict the levels of deformation and spatial layouts which are optimal for these stretchable fabrics, an analytical model was developed and was used to perform finite element modeling studies of the experimental systems. The metal interconnects are modeled as a composite

beam whose displacements have a sinusoidal form, with the amplitude determined by energy minimization. The island area is modeled as a composite plate and the PDMS substrate is modeled as a semi-infinite solid. The total energy of the system is defined as the membrane and bending energy of the metal interconnect and island area and the strain energy in the substrate. The analytical equation is:

$$\varepsilon_{bridge} = \frac{2\pi^2 w_{\max}}{\left(L^0_{bridge}\right)^2}\left(h + h_m - h_1 - y_0\right) + \frac{\pi^2 w_{\max}^2}{4\left(L^0_{bridge}\right)^2} - \frac{L^0_{bridge} - L_{bridge}}{L^0_{bridge}}$$

where L^0_{bridge} is the length of the ribbon interconnect prior to stretching, L_{bridge} is the length after stretching, and h, h_m, h_1 correspond to thickness of the individual layers of the system. Figure 3.5 (a) and (b) are schematic illustrations of the analytical model used to determine the amount of stress experienced in the solar fabrics for the interconnect area and the island area respectively. Figure 3.5 (c) shows the FEM simulation results for the strain across the interconnects with a prestrain of 22%. The maximum strain experienced by this area of the system at the max amplitude point is equal to 2.6×10^{-3} and the max strain experienced in the island area under mechanical deformation is 1.5×10^{-4} as shown in Figure 3.5 (d). This analytical model allows one to predict the appropriate choices of materials and layout design in order to ensure that the more brittle elements of our system experience the least amount of strain during operation. The quantitative aspects of this model will be compared to experimental results and will be described next.

Figure 3.6 (a) shows optical micrographs depicting the stretching directions and modes for 30% of strain using serpentine solar fabrics. Figure 3.6 (b) shows the J-V response of a non-optimized solar fabric during operation as illustrated in Figure 3.6 (a). These PV systems fabricated with a prestrain of 22%, which is suitable for most of the envisioned applications. When the fabric

is stretched in the x-direction the bridges (interconnects) flatten, while the polymer interconnects in the y-direction rise slightly from the plane depending on the degree of applied strain. As depicted in this figure, the layout of the system accommodates most of the strain experienced by the fabrication steps and that applied during use. A slight decrease in current can be attributed to possible light scattering from the interconnects that are in a flat state under stretching in the x-direction or cracks in the metal interconnects that are a result of the non-optimized layouts as determined by the modeling results; however, stretching in the y-direction shows no changes in performance. The system was functional without failure after 1000 cycles of stretching. Although important results are demonstrated in Figure 3.6, these levels of strain are not well suited for more mechanically demanding applications of stretchable PV. Changing the design of the bridge and fabrication of solar fabrics in optimized layouts per the theoretical results will lead to improved stretchability and open new application possibilities.

3.4 Conclusion

Collectively, the results and the types of module reported here may create new possibilities for monocrystalline Si photovoltaics. The design rules and layouts allow for high performance and elastic responses to high levels of strain. This type of stretchable solar cell could be applied for wearable solar cells or integrating Si photovoltaics onto bio-MEMS devices. Designing interconnects that offer higher levels of deformation or examining other semiconducting materials represent fruitful areas of future research.

3.5 Figures

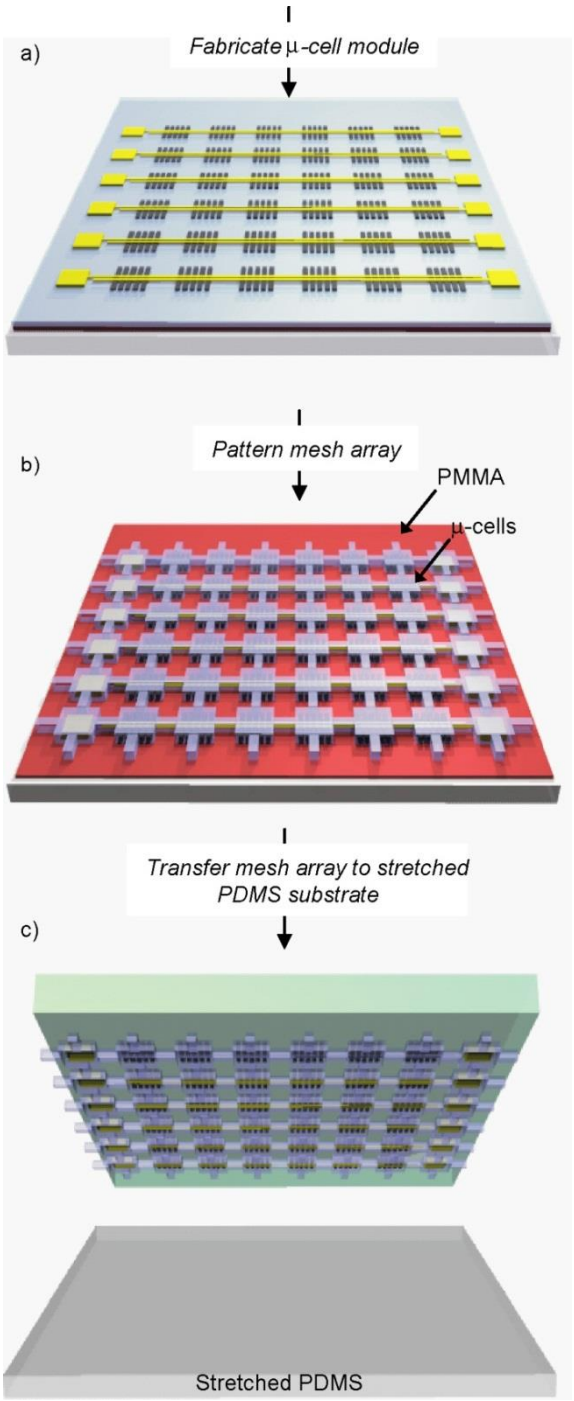

Figure 3.1 Schematic illustration of the processing steps for the fabrication of a stretchable module. (a) Metallization for interconnects. (b) Mesh array fabrication. (c) Transfer print mesh array onto a biaxially strained PDMS substrate.

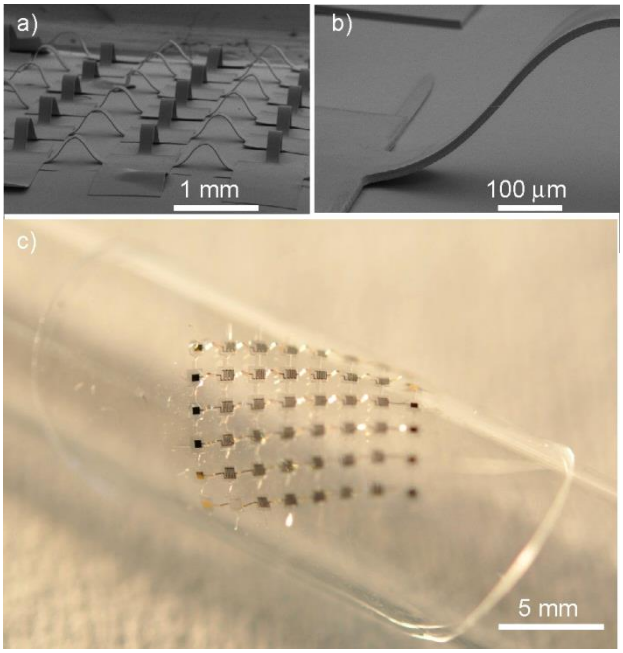

Figure 3.2 (a), (b) Scanning electron micrographs of a stretchable photovoltaic module that uses arrays of microcells interconnected by arc-shaped ribbons, bonded to a rubber substrate. (c) Optical micrograph of a completed stretchable module on a glass tube with a 2 mm bend radius.

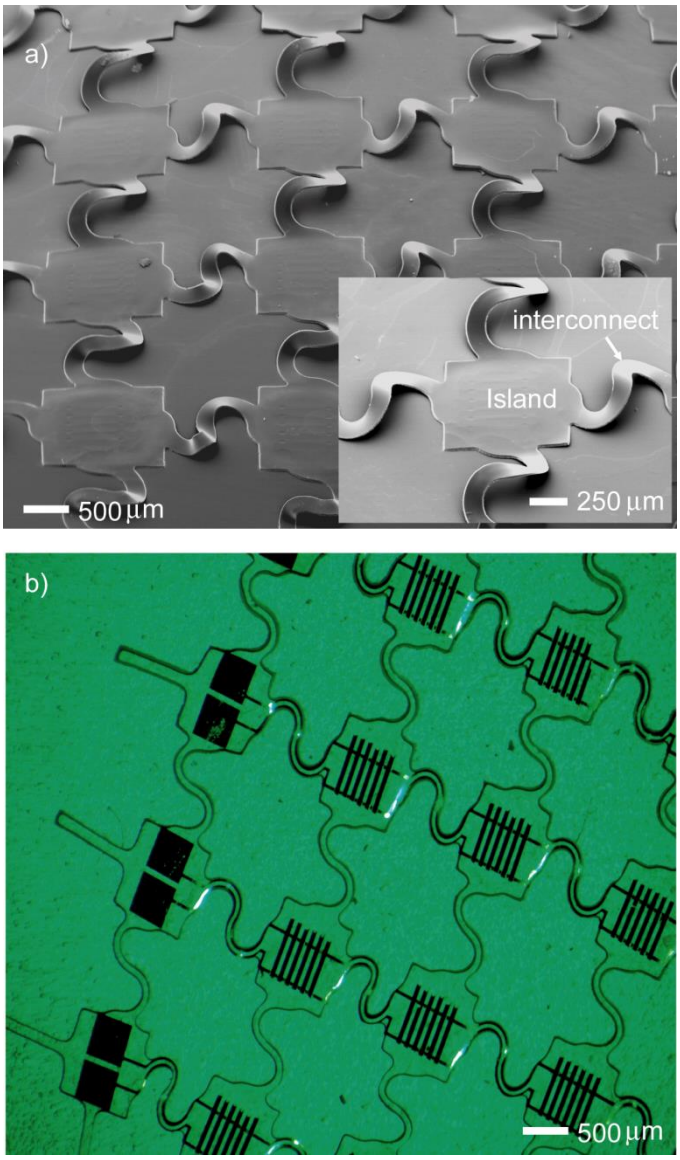

Figure 3.3 (a) Scanning electron micrograph of a stretchable photovoltaic module that uses arrays of microcells interconnected by serpentine ribbons, bonded to a rubber substrate. Inset shows a close-up image of an individual array. (b) Optical micrograph of a completed stretchable module on a glass tube with a 2 mm bend radius.

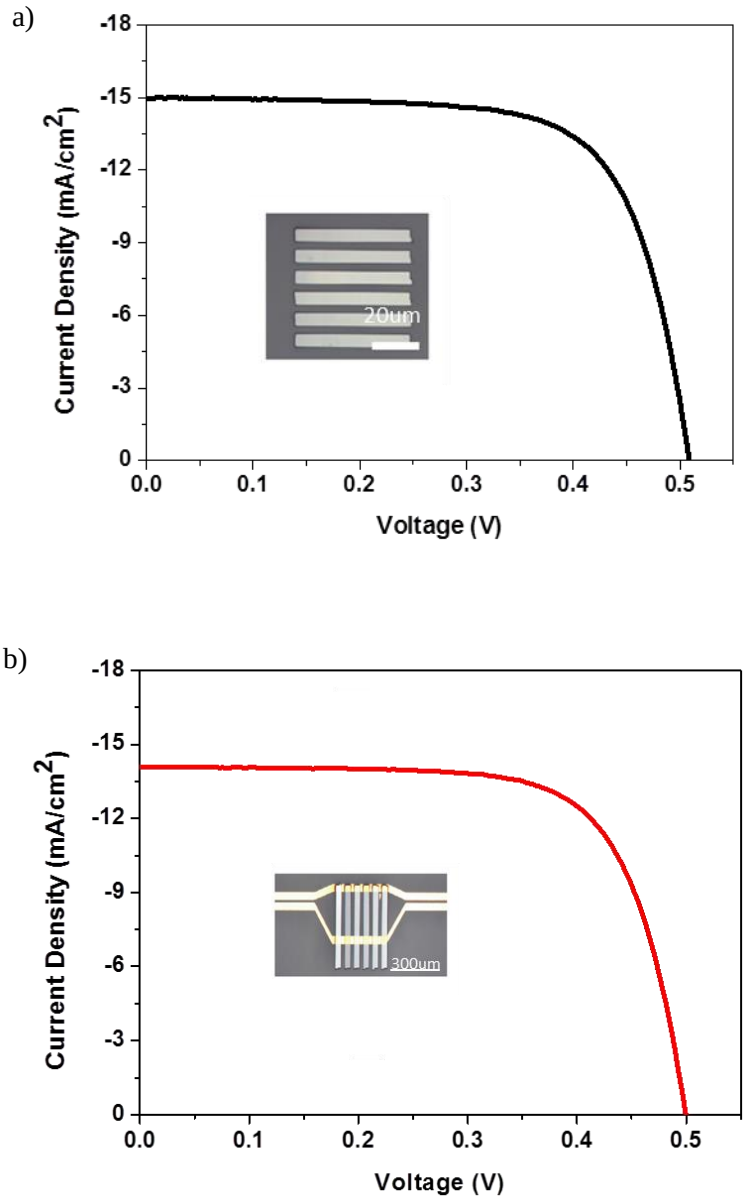

Figure 3.4 Current density-voltage curves for (a) an individual microcell and (b) an interconnected micocell array. Insets show optical images of the devices.

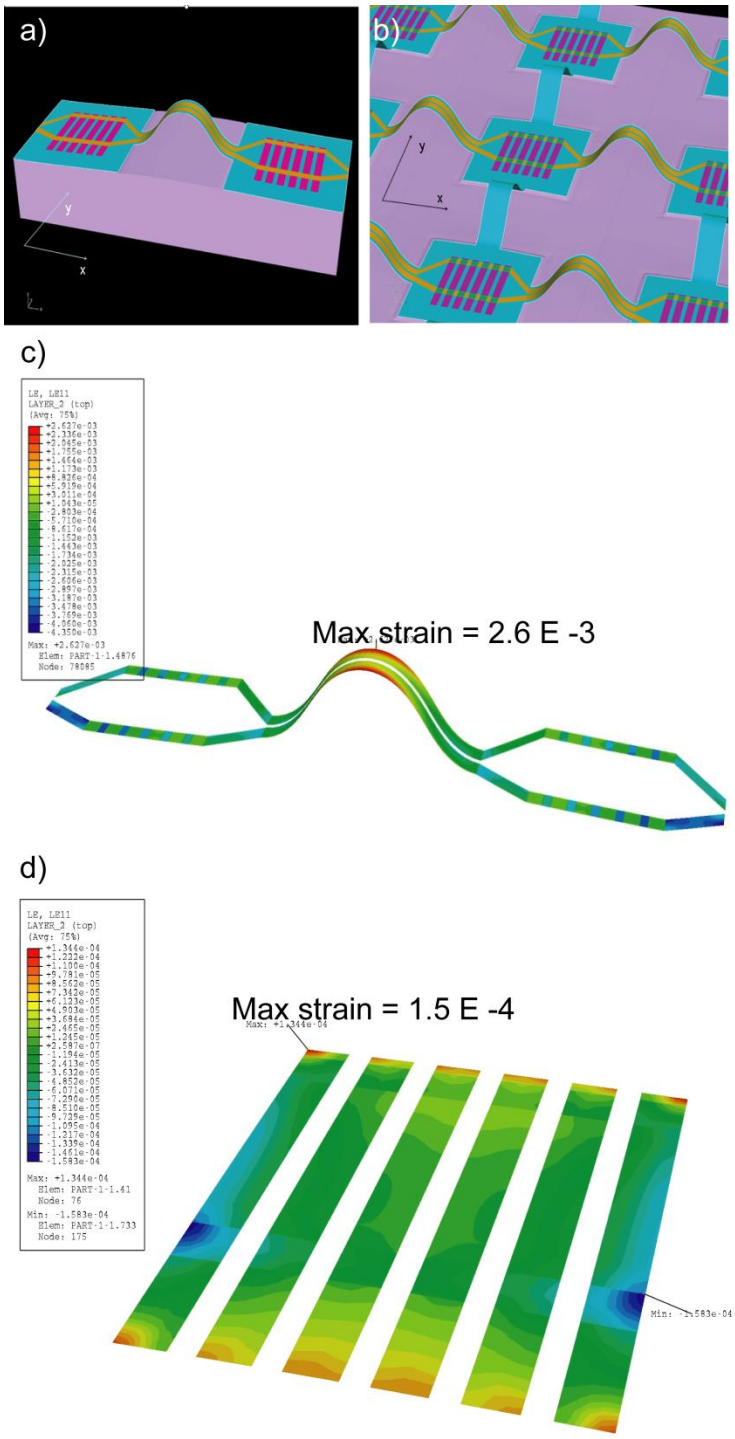

Figure 3.5 Schematic illustrations of the analytical model used to calculate the level of strain present in the interconnect area (a) and the island area (b). (c) Finite element solution for the strain in the interconnect area and (d) in the island area.

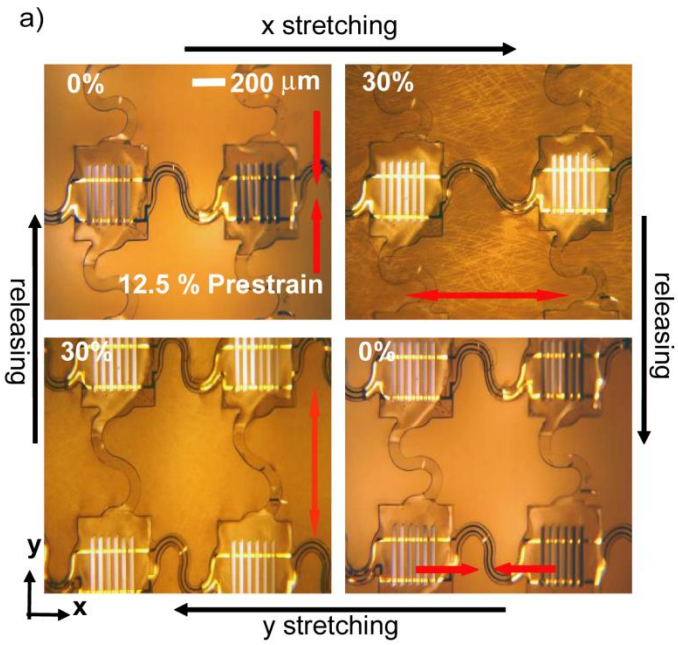

Figure 3.6 (a) Optical images of a stretchable fabric (serpentine shaped) illustrating the mechanical deformation modes. (b) Current density and voltage curves of solar fabrics stretched 30% in x (black), y (red) directions, and 0% (blue) stretching mode.

3.6 References

[1] D. M. Bagnall, M.Boreland, Energy Policy **36**, 4390-4396 (2008).

[2] M. A. Green *et al*., Solar Energy **77**, 857-863 (2004).

[3] M. Pagliaro, R. Ciriminna and G. Palmisano, ChemSusChem **1**, 880–891 (2008).

[4] A.W. Blakers and T. Armour, Solar Energy Materials & Solar Cells **93**, 1440–1443 (2009).

[5] F. C. Chen, J. L. Wu, C. L. Lee, W. C. Huang, H. M. P. Chen, and W. C. Chen, IEEE Electron Device Letters **30**, 727-729 (2009).

[6] D. H. Kim *et al*., Science **320**, 507-511 (2008).

[7] D. H. Kim *et al*., Applied Physics Letters **93**, 044102 (2008).

[8] D. H. Kim and J. A. Rogers, Advanced Materials **20**, 4887-4892 (2008).

[9] D. H. Kim *et al*., Proceedings of the National Academy of Sciences **105**, 18675-18680 (2008).

Chapter 4. COMPACT SI MINIMODULES WITH HIGH-VOLTAGE OUTPUT

4.1. Introduction

Si continues to be one of the most compelling materials for solar energy conversion; it remains the dominant choice for commercial photovoltaic applications. Research in this area focuses mainly on enhancing the conversion efficiency of non-crystalline Si, reducing the materials usage per unit power output and relaxing the requirements on purity. Thin films of amorphous or microcrystalline Si and thin sheets of single-crystalline Si are the most widely explored routes to efficient materials utilization. Recently, we reported an alternative strategy that involves production of ultrathin and small Si solar cells (i.e., microcells) from bulk, commodity wafers by use of lateral anisotropic etching techniques, followed by assembly of these microcells into interconnected arrays by use of soft, transfer printing methods. Here we describe modules that exploit large collections of such microcells printed to allow series electrical interconnection for compact modules (0.95 cm × 0.63 cm) that are capable of producing high-voltage outputs. When formed on thin sheets of plastic in optimized neutral mechanical plane designs, these modules can bend to radius of curvature as small as ~ 2 mm without any measureable changes in the mechanical or electrical properties. These devices provide a relatively simple route to a low-cost, high-voltage flexible photovoltaic device, suitable for portable and wearable electronic applications.

A type of compact (~cm^2) high-voltage photovoltaic module that utilizes large collections of ultrathin (~15 μm), small (~45 μm wide, ~1 mm long) Si solar cells was fabricated and characterized. Integration on thin sheets of plastic yields small, flexible modules with per-cell efficiencies of ~8%, voltage outputs >200 V and maximum power outputs >1.5 mW.

In the past several years the photovoltaic (PV) market has experienced rapid growth, with Si (in various crystalline forms) constituting ~90% of the market [1]. Enhancing the conversion efficiency of non-crystalline Si [2], reducing the usage of Si per unit power output [3] and relaxing purity [4] requirements on Si feedstock represent some priorities for research. Routes for reducing Si usage and facilitating large area processing, both with the potential to lower costs, include use of ultrathin layers of either amorphous or microcrystalline Si [5]. The main disadvantage of these approaches is the diminished performance of the associated solar cells compared to similar devices formed with monocrystalline Si. One alternative strategy to large area, materials-efficient cells relies on anisotropic etching procedures to create thin 'slivers' of Si from bulk wafers, followed by mechanical manipulation to form modules [6]. Recently, we reported a complementary approach that first creates ultrathin bars, membranes or ribbons of Si from the near surface of a wafer. This uses procedures originally developed for thin Si electronic devices [7, 8], and assembles the elements, each configured as a separate, functional solar cell (i.e., a microcell, or μ-cell), in ordered arrays on a target substrate by use of a soft printing process [3]. These techniques allow for the fabrication of compact modules out of hundreds or thousands of such microcells, with good efficiencies and the capacity to exploit Si in unconventional module designs. These offer, for example, mechanically flexible and even stretchable formats, semitransparent layouts, and ultralow profile micro-concentrator designs.

An important additional feature of the microcell module construction introduced here is the relative ease with which the outputs can be configured for high voltage. Such layouts can be important for driving devices that require high (e.g., microelectromechanical systems and certain classes of electronic paper technologies) or even moderate voltage (logic circuits), and they can also be exploited to reduce series resistance losses. Recent reports describe small scale modules

with high voltage outputs based on thin films of polymer [9] and crystalline Si [10] as active materials. The former case employs a structured design that offers the possibility for cost-effective, mechanically flexible modules, but with efficiency and long-term reliability limited by the polymers. The latter example involves the use of a rigid, Si-on-insulator wafer whose cost is unlikely to be compatible with most applications. Neither system offers the combination of small-scale design, robust high-performance operation and mechanical properties required of some of the most demanding (i.e., mechanically) or otherwise interesting applications.

4.2 Experimental

The fabrication for the microcells reported here uses processes whose details are described elsewhere [3]. Briefly, the process begins with a p-type (111) Czochralski Si wafer (3 inch diameter, 1-10 Ω cm, 450 μm thickness, Virginia Semiconductor) coated with a layer of SiO_2 (600 nm) formed by plasma-enhanced chemical vapor deposition (PlasmaTherm SLR). The SiO_2 was lithographically patterned with stripe openings. Inductively coupled plasma reactive-ion etching (STS ICP-RIE) [8] formed trench structures in the Si, with typical depths of 15–20 μm and widths of 45 μm. Selective doping of emitter and bottom contact areas used solid-state sources of boron (BN-1250, Saint Gobain) and phosphorus (PH-1000N, Saint Gobain) at 1000 °C under N_2 atmosphere for 30 min (boron) and 10 min (phosphorus). Protecting the top surfaces and sidewalls with a bilayer SiO_2/Si_3N_4 mask followed by immersion in a KOH bath resulted in undercut etching of the microcells, leaving them tethered to the underlying wafer only at their end points and ready for printing and integrating into modules.

Light and dark current (*I)* – voltage (*V)* measurements of microcells were carried out at room temperature using a dc source meter (model 2400, Keithley) and a 1000 W full-spectrum

solar simulator. For individual microcells the reported figures of merit are based on the spatial dimensions of the microcells, without accounting for coupling of light through the edges. Module level efficiencies are reported using both the aperture area (i.e., includes blank spaces between the cells; 0.95 cm × 0.63 cm) and the active area (i.e., only the Si area exposed to incoming flux; 0.50 cm × 0.57 cm). In all cases, we used a diffusive backside reflector during measurements. Certainly, there is a contribution from diffuse illumination and from the inter-cell areas, but this inherent feature of the reported devices is a further benefit as it provides more power per unit area of the device. Electrical characterization of performance during bending involved mounting completes modules onto the outer surfaces of glass tubes with a radius of curvature of 4 mm. Light and dark *I–V* measurements at various bending geometries and bending radii were performed under ambient conditions. Fatigue tests were also performed, where one cycle corresponds to bending a module to a given radius and then relaxing it to the flat state.

4.3 Results and Discussion

Figure 4.1 (a) shows a scanning electron microscope (SEM) image of partially undercut microcells, tethered to the host wafer via anchor points at their ends; the widths, lengths and thicknesses were ~45 μm, ~1.5 mm and ~15 μm, respectively. The microcell layouts were fabricated such that p^+ and n^+ doped regions alternate from cell to cell, as shown in the colorized SEM image in Figure 4.1 (b). The green, red and grey areas represent phosphorus doped regions (1.30 mm long), boron doped regions (0.15 mm long), and undoped regions (0.05mm), respectively. This design provides access for top-side contacts, thereby facilitating the wiring of individual cells for metal interconnection in series, in a monolithic fashion.

Figure 4.2 (a) provides a schematic illustration of transfer printing microcells (via an elastomeric stamp; PDMS) for integration into modules. The microcells are tethered onto the host wafer via anchor points [11] as illustrated in Figure 4.2 (b). Placing the PDMS stamp on the surface of the microcells, followed by quickly lifting the stamp [12], removes the microcells from the host wafer (Figure 4.2 (c)). Insets in Figure 4.2 (b) and 4.2 (c) show close-ups of the anchor regions before and after retrieval of the stamp, respectively. The PDMS stamp is used to print the cells onto a layer (~ 30 μm) of photocurable polyurethane (NOA 61; Norland Optical Adhesive) spin-coated onto a glass slide (carrier substrate). Metallization via sputter coating of Cr/Au (5 / 600 nm) followed by photolithography and etching of the exposed metal defined interconnect wiring. For flexible systems, a second layer of NOA (30 μm thick) cast on top of the printed arrays placed the fragile elements (i.e., metal and Si) close to the neutral mechanical plane of modules completed by removal from the carrier substrate. Figure 4.2 (d) illustrates a module consisting of 768 microcells connected in series. The metallization factor for this layout is ~ 16 %, defined as the fraction of device area covered in an individual microcell.

Figure 4.3 (a) depicts a high-resolution SEM image of a section of the high-voltage minimodule which depicts the device layout. Figure 4.3 (b) shows the *IV* characteristics of a typical, individual microcell. The solar conversion efficiency ranged 6-8% with open circuit voltages (V_{oc}) between 0.44-0.48 V, current densities (J_{sc}) of 23-26 mA/cm^2, maximum power (P_{max}) output of 3-4 μW and fill factors of 0.67-0.68. Efficiencies in the current devices are limited by low J_{sc} and V_{oc} values possibly due to carrier recombination at the metal contacts. Figure 4.3 (c) shows the *IV* characteristics for different numbers of rows of microcells (128 microcells per row) connected in series. An individual row fabricated in this way shows maximum voltage and power outputs of ~ 51 V and 0.37 mW, respectively. As shown in Figure 4.3 (c), increasing the number of rows

leads to systematic and expected changes in the characteristics, with voltage outputs of 51 V, 104 V, 155 V and 209 V for 1, 2, 3, 4 rows, respectively. Si solar cells with conventional dimensions would require much larger areas to generate the voltages produced here. The inset in Figure 4.3 (c) shows the maximum power (1.55 mW) from a 0.95 cm × 0.63 cm module composed of 512 microcells. The aperture area and active area efficiency for this minimodule is 2.8% and 5.2%, respectively. Figure 4.3 (d) presents the scaling properties of the number of microcells interconnected in series and the corresponding voltage and maximum power outputs. The results scale in an almost linear fashion, as expected. Such arrays of microcells can also be wired in parallel for high-current applications, thereby allowing for a wide range of voltage and current requirements depending on the target application.

A unique aspect of the printing approach to integration is the ability to assemble microcells on sheets of plastic in a scalable, deterministic and high-throughput manner, for the fabrication of flexible and rollable PV modules, in optimized neutral mechanical layouts. Figure 4.4 (a) shows an optical image of a high-voltage flexible PV module conformally wrapped around a glass tube with a radius of curvature of ~ 7 mm. For a unit cell as shown in the inset of Figure 4.4 (b), analytical modeling gives the strain at position z as $\varepsilon = (z - z_0)/R$ for bending perpendicular (y-direction) to the interconnect direction, where R is the bending radius, $z_0 = a - t/2 - (1/2)(a+b)(a-t-b)/\left[a+b+t(E_{Si}/E_{NOA}-1)W_{Si}/W\right]$ is the position of neutral mechanical plane, E_{Si} and E_{NOA} are the Young's moduli of Si and NOA, and a, b, t, W_{Si} and W are the geometry parameters as shown in the inset of Figure 4.4 (b) [3]. The maximum strain in the Si is

$$\varepsilon_{\max}^{Si} = \frac{t}{2R}\max\left[\left|1+\frac{a-t-b}{t+\frac{t^2}{a+b}\left(\frac{E_{Si}}{E_{NOA}}-1\right)\frac{W_{Si}}{W}}\right|,\left|1-\frac{a-t-b}{t+\frac{t^2}{a+b}\left(\frac{E_{Si}}{E_{NOA}}-1\right)\frac{W_{Si}}{W}}\right|\right]$$

Since the metal is very thin, its strain approximately equals to the strain at the top surface of Si and is obtained as

$$\varepsilon_{\max}^{metal} = \frac{t}{2R}\left[1+\frac{a-t-b}{t+\frac{t^2}{a+b}\left(\frac{E_{Si}}{E_{NOA}}-1\right)\frac{W_{Si}}{W}}\right]$$

Based on experimental structures and geometry layouts, maximum strains in the microcells and metal interconnects are less than 0.4% for bending radius of 2 mm perpendicular (y-direction) to the interconnect direction [3]. Figure 4.4 (b) presents finite element modeling of the distribution of strain for outward bending to a radius of curvature of 4 mm along (x-direction) the interconnect direction, while Figure 4.4 (c) shows the *IV* characteristics of such modules in a flat state (un-bent), bent along (x-direction) and perpendicular (y-direction) to the interconnect direction and under a twisting deformation (45°). The results in Figure 4.4 (c) and mechanical fatigue test of up to 1000 cycles show little or no change in the *IV* characteristics, consistent with the analytical modeling results.

4.4 Conclusion

In conclusion, this work demonstrates a compact Si solar module capable of producing high voltage outputs in mechanically flexible designs. Demonstration experiments show voltage and power outputs >200V and >1.5 mW, respectively, and bendability to radii of curvature down to ~2 mm without significant changes in the solar cell figures of merit. These results illustrate some advantages of modules that rely on microcells and printing-based assembly techniques. The more general design consideration in this thesis might be useful for Si solar cells and other classes of photovoltaic systems.

4.5 Figures

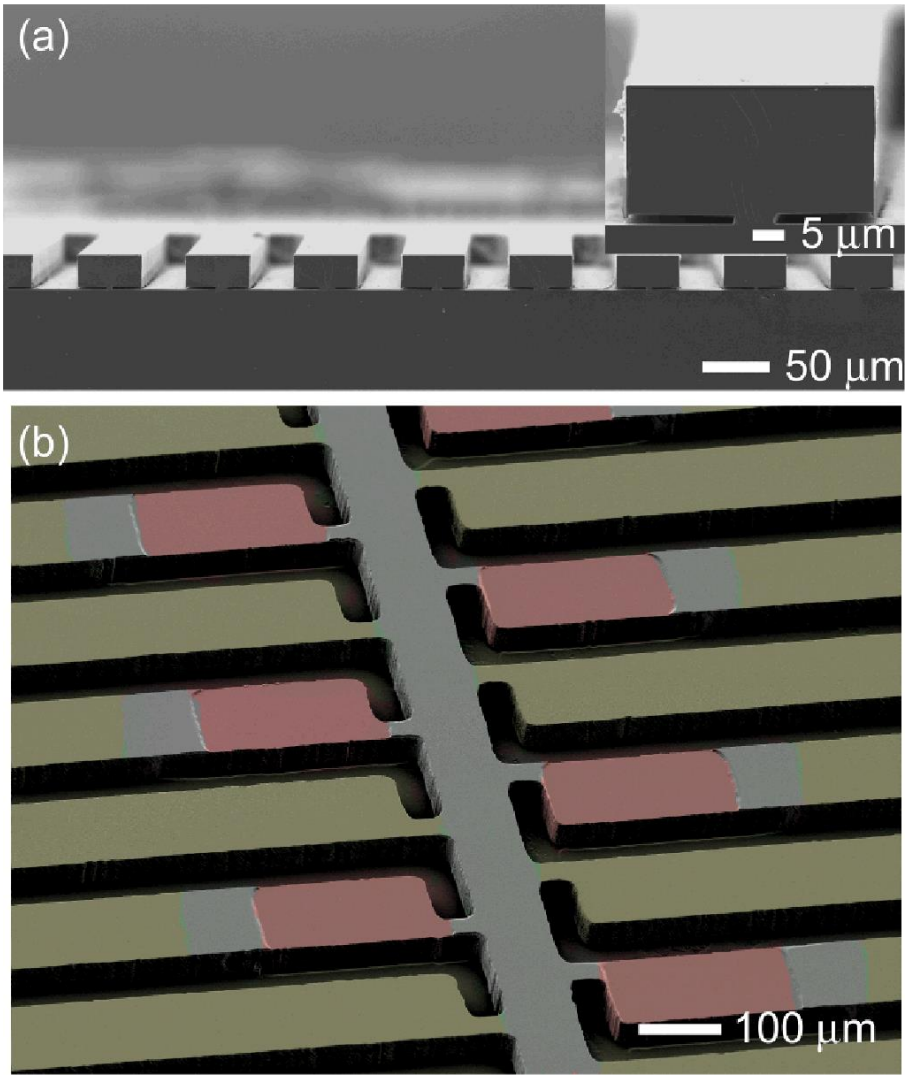

Figure 4.1 (a) SEM cross-sectional view of partially undercut microcells. (b) Colorized SEM image of an array of microcells on a source wafer, ready for printing, illustrating the selective doping areas and microcell layout. Green regions correspond to phosphorous doped area (n^+), red regions are boron doped area (p^+) and gray areas are un-doped Si.

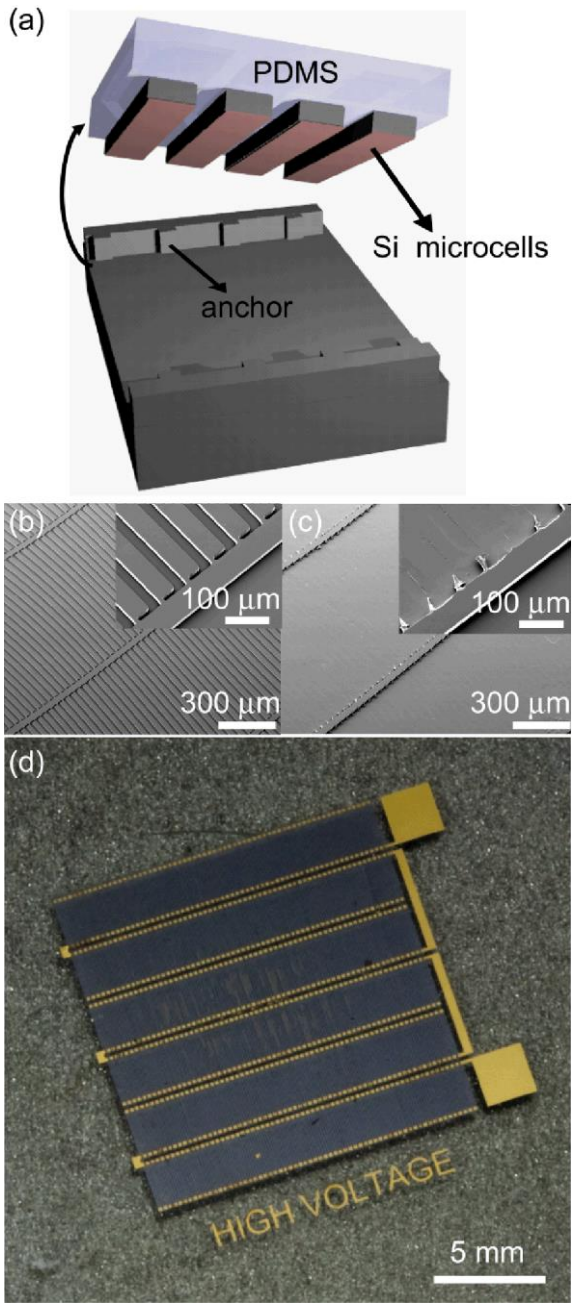

Figure 4.2 (a) Schematic illustration of the transfer printing process used to fabricate high-voltage PV minimodules. (b) SEM image of fully undercut microcells tethered onto a Si wafer ready for printing and (c) SEM image of the Si wafer after retrieval of the microcells. Insets in (b) and (c) show close up views of the anchor geometries before and after pickup. (d) Optical image of a completed minimodule consisting of printed microcell arrays metal interconnected in series by Cr/Au metal grid lines.

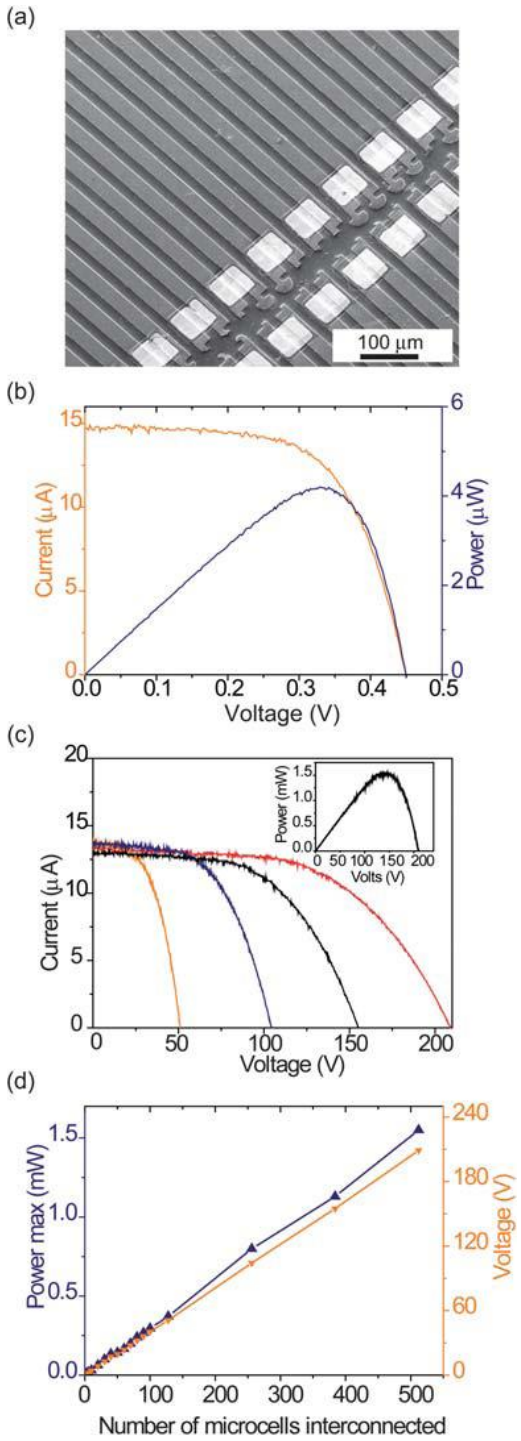

Figure 4.3 (a) SEM image of a section of a high-voltage minimodule depicting the device layout. The lighter regions (rectangular features) in the image of (a) correspond to the Au metal contacts. (b) Current-voltage characteristics of an individual high-voltage Si microcell. (c) Current-voltage characteristics of rows of Si microcells metallically interconnected in series from left to right: 1 row (blue), 2 rows (green), 3 rows (red) and 4 rows (black). Inset depicts the maximum power output of 512 microcells. (d) Scaling properties for voltage and power outputs of different microcells interconnected in series.

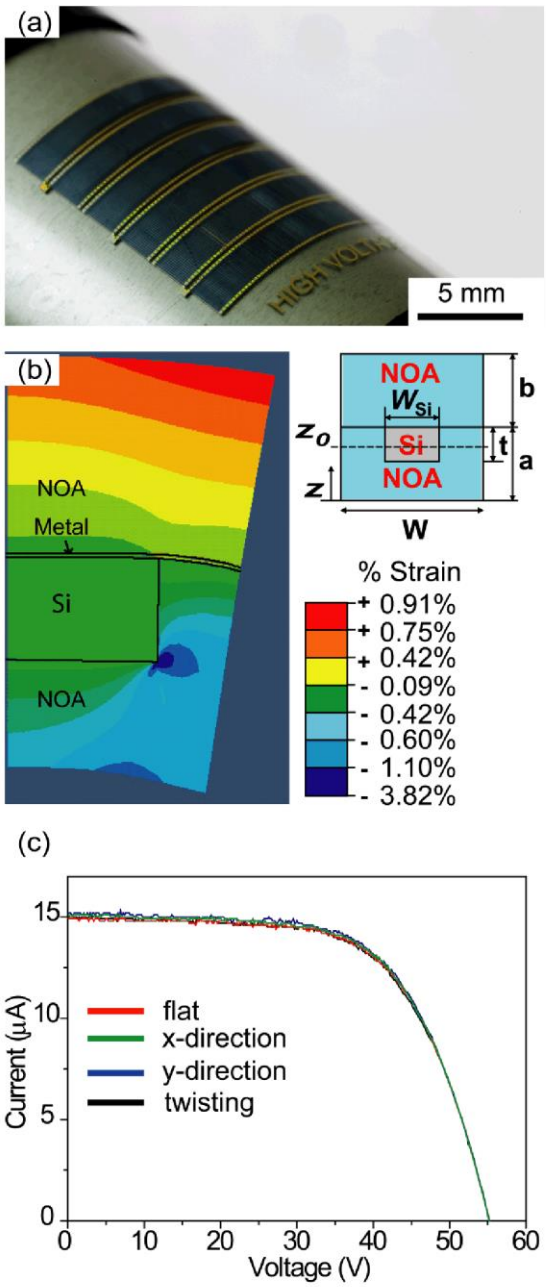

Figure 4.4 (a) Optical micrograph of a flexible high-voltage module conformally wrapped around a glass tube. (b) Color contour plot of calculated bending strains (ε_{xx}) through a cross-section of a high-voltage minimodule, bent outward along the cell width direction at a bending radius of 4 mm. Inset depicts the unit cell of the flexible modules, which is used to deduce the analytical modeling results. (c) Current-voltage characteristics of a high-voltage minimodule in un-bent flat state, bent along the cell width and the metal interconnect pad width, and under a twisting deformation (45 °).

4.6 References

[1] D. M. Bagnall, M.Boreland, Energy Policy **36**, 4390-4396 (2008).

[2] M. A. Green et al., Solar Energy **77**, 857-863 (2004).

[3] F. J. Haug, T. Soderstrom, M. Python, V. Terrazzoni-Daudrix, X. Niquille, and C. Ballif, Solar Energy Materials and Solar Cells **93**, 884-887 (2009).

[4] M. Pagliaro, R. Ciriminna and G. Palmisano, ChemSusChem **1**, 880–891 (2008).

[5] A. W. Blakers and T. Armour, Solar Energy Materials & Solar Cells **93**, 1440–1443 (2009).

[6] F. C. Chen, J. L. Wu, C. L. Lee, W. C. Huang, H. M. P. Chen, and W. C. Chen, IEEE Electron Device Letters **30**, 727-729 (2009).

[7] D. H. Kim *et al*., Science **320**, 507-511 (2008).

[8] D. H. Kim *et al*., Applied Physics Letters **93**, 044102 (2008).

[9] D. H. Kim and J. A. Rogers, Advanced Materials **20**, 4887-4892 (2008).

[10] D. H. Kim *et al*., Proceedings of the National Academy of Sciences **105**, 18675-18680 (2008).

[11] M. A. Meitl, X. Feng, J. Y. Dong, E. Menard, P. M. Ferreira, Y. G. Huang and J. A. Rogers, Applied Physics Letter **90**, 083110 (2007).

[12] M.A. Meitl, Z. T. Zhu, V. Kumar, K. J. Lee, X. Feng, Y. Y. Huang, I. Adesida, R. G. Nuzzo, and J. A. Rogers, Nature Materials **5**, 33 (2006).

Chapter 5. ULTRATHIN CELLS WITH LIGHT-TRAPPING STRUCTURES

5.1 Introduction

Ultra-thin monocrystalline Si solar cells are attractive due to their potential to achieve high efficiency operation and efficient materials utilization, in forms that are mechanically flexible and lightweight. We present the design and fabrication of cells of this type, in which bulk wafers serve as sources of material for ~3 μm thick bars of Si that include patterns of surface relief, antireflection coatings and back reflectors collectively configured to maximize absorption via trapping of light. Even with unoptimized patterns of doping and designs for electrical contacts, these devices yield power conversion efficiencies of ~8.5 %, corresponding to a ~190 % enhancement over those of otherwise identical cells without light trapping schemes. Integrating such cells into large-scale arrays on sheets of plastic yields lightweight, mechanically flexible modules, with properties that could facilitate transport and installation and/or enable use in portable applications. Si (Si) remains the material of choice for photovoltaic (PV) applications due to a favorable set of electrical and optical properties, excellent lifetime/reliability, low costs in manufacturing and high natural abundance [1-2]. Performance in commercially available cells already approaches the theoretical limit [3-5]. As a result, research on Si photovoltaics often now focuses on cost-effective means for manufacture, schemes for efficient materials utilization, and unusual methods for integration of Si into modules [6-11]. Routes to ultrathin Si in designs optimized for light management, i.e. light trapping and antireflection, are valuable in this context. Such types of ultra-thin cells are additionally attractive because they offer other attributes such as mechanical flexibility and rugged construction, when mounted on plastic substrates [12,13]. Notable advances in recent years include methods for kerf-less production of thin wafers from Si boules by controlled fracture [14-17], and

for fabrication of ultrathin bars and sheets of Si from wafers by anisotropic etching [8-11, 18, 19]. The most advanced demonstrations of the second strategy involve thin (~6 μm), microscale cells (μ-cells) that incorporate light-trapping structures (LTSs) and anti-reflection coatings (ARCs) [20]. The present work introduces refined fabrication techniques that enable further reductions of thickness by more than a factor of two, and light-trapping (LT) schemes that exploit engineered cavity resonances between a top surface LTS and a bottom backside reflector (BSR). By comparison to previous results, these devices offer not only more than a doubling of the efficiency in materials utilization, but also an order of magnitude reduction in stiffness [21]. The latter enables use in ultra-compliant, flexible modules and a reduction in the minimum bend radius by a factor of two.

5.2 Experimental

The fabrication starts with a P-type Czochralski Si <111> wafer (1-10 Ω-cm, 450 μm thickness, Virginia Semiconductor). The first step involves lithographically patterning arrays (180 × 14, over an area of 1 cm^2) of microbars (0.59 mm length × 0.25 μm width) aligned perpendicular to the Si <110> direction. Inductively coupled plasma reactive ion etching (ICP-RIE) in the regions between the bars (strips with 80 μm widths) yields trenches with depths of ~3.3 μm. For each bar, solid state doping of boron (Boron, BN-1250, Saint Gobain) along lengths of L_{p+} = 60 μm and phosphorus (phosphorus, PH-1000N, Saint Gobain) along lengths of L_{n+} = 0.5 mm, at 1000 ℃ (25 min) and 950 ℃ (10 min), respectively, through patterned hard masks of SiO_2 (900 nm), produces rectifying P-N junctions. Conformal deposition of bilayers of SiO_2 (100 nm)/SiN_x (500 nm) by plasma-enhanced chemical vapour deposition (PECVD, PlasmaTherm SLR) followed by annealing at 400 ℃ for 30 min establishes etch barriers on the top surfaces of the bars, as well as

the sidewalls and bottoms of the etched trenches. Directional deposition of Cr (100 Å)/Au (1000 Å) by electron beam evaporation (Tumescal, FC 1800) at an angle of ± 30° coats the sidewalls and top surfaces, to allow selective removal of the exposed SiO_2/SiN_x in the trenches by reactive-ion etching (CHF_3 (40 sccm)/O_2 (2 sccm); 50 mtorr, 150 W, 15 min). Immersing the processed wafer into a solution of potassium hydroxide (PSE-200, Transene) etches the Si preferentially along the <110> direction, starting at the exposed bottoms of the trenches, thereby producing arrays of freely suspended microbars tethered to the underlying wafer at their ends. Boron doping (1000 ℃ for 5 min) using the residual layers of SiO_2/SiN_x as a mask yields a back surface field, thereby completing the fabrication of collections of functional solar μ-cells. This overall process has yields of ~99 %.

5.3 Results and Discussion

A scanning electron microscope (SEM; Hitachi s4800) cross sectional image of a wafer after partial undercut etching of an array of μ-cells appears in Figure 5.1, with a magnified view of an individual μ-cell on the right. Figure 5.2 (a) presents an optical image of an array of μ-cells (left) and a schematic illustration (right). Each μ-cell is 25 μm wide, 0.59 mm long, and ~3 μm thick. The pink, grey, and blue areas in this illustration correspond to boron doped (L_{p+} = 60 μm), un-doped (L_p = 30 μm), and phosphorus doped (L_{p+} = 0.5 mm) regions respectively. After transfer printing onto a substrate of interest, soft imprint lithography and etching define LTSs on the top surfaces of the μ-cells. Figure 5.2 (b) provides top-view SEM images of LTSs consisting of a hexagonal lattice of cylindrical posts of Si, with periodicity, diameter and height of 500 nm, 370 nm and 120 nm, respectively. A bilayer of SiN_x (35 nm) and SiO_2 (50 nm) deposited by PECVD serves as an ARC. Furthermore, layer of silver (~200 nm) deposited on the backside of the glass substrate provided a BSR. (Previous work involving μ-cells with 6 μm thicknesses did not

incorporate the cavity layout that is enabled by this BSR.) Figure 5.2 (c) illustrates schematically the layers that constitute a completed μ-cell. The NOA in this figure is a thin, transparent layer of a photo-curable polyurethane that bonds the cells to the glass substrate (1 mm thick).

Three-dimensional finite difference time domain (FDTD) techniques and optical absorption measurements quantitatively reveal the roles of the LTS, the ARC and the BSR. The FDTD simulations assume a 3 μm thick film of Si with infinite lateral extent. The top hexagonal pattern diffracts/scatters light to increase the optical interaction length and, by consequence, the absorption. The BSR further increases this length and also establishes cavity resonances. Some of the higher order diffracted/scattered light remains trapped inside the Si via total internal reflection at the top surface. In both FDTD and experiment, the absorption (A) corresponds to A = 1-T-R where T and R are the transmission and reflection, respectively. Figure 5.3 (a)-(b) compares the relative absorption (with respect to the solar AM1.5D spectrum) for 3 μm thick μ-cells with and without the light trapping scheme (i.e. bare vs LT), evaluated using FDTD and experimental measurements with an AM 1.5D solar spectrum. The measured absorption is limited to 550 nm -1100 nm wavelength range by the source-detector combination in our microscope-coupled FTIR system (Bruker Vertex 70-Huperion 1000). The simulated and measured absorption values, integrated over the spectrum, are 27.6 % (Figure 5.3 (a)) and 28 % (Figure 5.3 (b)), respectively, for the bare μ-cell; with the LT μ-cell, these values increase to 69 % and 77 % respectively. The graph in Figure 5.3 (c) shows in an absolute scale that much of the absorption enhancement due to light trapping appears near the band edge, as expected, where bare Si is weakly absorbing. The thin geometry of the μ-cells leads to Fabry-Perot cavity resonances [22] in both bare and LT cases. The LT configuration, however, greatly enhances these effects. Here, the combined presence of the top diffractive pattern associated with the LTS and the bottom BSR induces not only resonances

associated with 0^{th} order diffraction but with the 1^{st} diffracted order as well. Moreover, these and other higher diffraction orders remain trapped due to total internal reflection. The FDTD simulation assumed perfect arrays of nano-posts as the diffractive top surfaces of the microcells. These structures diffract the incident solar spectrum as multiple diffraction orders inside the Si. In actual cells, the nano-posts possess non-ideal surface profiles due to imperfections associated with the lithography and dry etching processes. These imperfections scatter light in excess of that expected by diffraction alone, thereby leading to additional absorption. The slight discrepancies between experimental observations and FDTD predictions are likely due to such non-idealities of the etched surface relief geometries and thickness variation across the wafer and finite lateral geometries of the μ-cells.

To further understand the spectral aspects of light trapping, we examined the wavelength dependence of enhancements (compared to the bare case) in both absorption and efficiency. Figure 5.3 (d) presents experimental and FDTD results. Eight separate bandpass filters, each with 40 nm bandwidth (FWHM), centered at 550 nm, 650 nm, 750 nm, 850 nm, 900 nm, 950 nm, 1000 nm and 1050 nm, enable spectrally resolved efficiency measurements. The absorption data exhibit sharp narrow bands expected from cavity resonances. In FDTD predicted and measured absorption enhancement, sharp narrowband Fabry-Perot cavity resonances were observed. However, for wavelength dependent efficiency measurements, cells were illuminated with band-limited spectra (bandwidth ~ 100 nm) centered at wavelengths of 550 nm, 650 nm, 750 nm, 850 nm, 950 nm, 1050 nm. Due to the averaging over the filter bandwidth, sharp resonances in the efficiency enhancement spectrum were eliminated. The averaged responses and the overall trends exhibit good agreement.

Figure 5.4 (a) shows the measured current density (J) as a function of voltage (V) for various

μ-cell designs, using simulated AM 1.5D illumination of 1000 W/m^2 at room temperature. For accurate measurements, a lithographically defined pattern of metal (Cr/Au: ~10 nm/200 nm) served as an aperture to prevent exposure of the cells to unwanted, parasitic light. Separate studies isolate the effects of the LTS, ARC and BSR, and their combinations. The samples include: bare Si, with ARC, with BSR, with BSR+ARC, with LTS, with LTS+ARC, with LTS+BSR and, finally, with LTS+BSR+ARC (i.e. LT μ-cell). The data in Figure 5.3(a) yield key properties that can be considered individually. First, and most simply, is the short circuit current (J_{sc}). This quantity can be expressed as

$$J_{sc} = q g_{op}(L_p + L_{\mathrm{n}}) \tag{1}$$

where q is the charge of an electron/hole, g_{op} is the optical generation rate, and L_p and L_n are the minority carrier diffusion lengths. The minority carrier diffusion lengths are determined largely by the materials quality, the doping profiles and the surface properties. Among the devices corresponding to the data of Figure 5.4 (a), all such parameters are roughly the same. As a result, trends in J_{sc} should follow those in g_{op}, or, equivalently, the absorption. As shown in the table of Figure 5.4 (b), J_{sc} of bare Si and bare Si with LTS+BSR+ARC are 9.62 mA/cm^2 and 24.57 mA/cm^2, respectively. The enhancement of J_{sc} of bare Si compared to that of LT cell (LTS+BSR+ARC) is ~155 %, which is consistent with both experimentally measured and FDTD calculated enhancements in absorption, i.e. $((\frac{69\%}{27.6\%} \times 100 - 100)\ \% = 150\ \%)$ and $((\frac{77\%}{28\%} \times 100 - 100)\ \% = 175\ \%)$, respectively, according to the data of Figure 5.3 (a),(b).

The open circuit voltage (V_{oc}) is another important parameter. Under assumptions similar to those

for Eqn. (1), this quantity can be written:

$$V_{oc} = \frac{nkT}{q} ln(\frac{L_p+L_n}{L_p p_n/\tau_p+L_n n_p/\tau_n} g_{op} + 1) \quad (2)$$

where n is the ideality factor, k is the Boltzmann constant, T is the temperature, p_n and n_p are the minority carrier concentrations, τ_p and τ_p are the minority carrier life time, and q, L_p, L_n, and g_{op} are the same parameters as stated in Eqn. (1). As for the case of J_{sc} the examined μ-cells differ mainly in g_{op}. The expectation, then, is that V_{oc} should vary according to $ln(cg_{op}+1)$ where c is a constant. The V_{oc} of μ-cells built with bare Si and with LTS+BSR+ARC are 0.45 V, and 0.494 V respectively, as in the table of Figure 5.4 (b). The increase corresponds to ~10 %, roughly consistent with the expected weak, logarithmic scaling. The fill factors (*FF*) for all cases are between 70.5 % and 71.5 %, with no systematic variations. *FF* is the ratio of maximum power (P_{max}) to the product of V_{oc} and J_{sc}. The results suggest, then, that P_{max} increases by an amount approximately equal to that of the product of V_{oc} and J_{sc}, consistent with dominant effects of changes in the optical generation rate (g_{op}) associated with different cell configurations as shown in Figure 5.4 (a). Finally, the corresponding measured energy conversion efficiencies are 2.90, 3.7, 4.14, 4.69, 6.13, 6.68, 7.67 and 8.47 % for various cases, as tabulated in Figure 5.4 (b). The LTS+BSR+ARC configuration yields the highest overall energy conversion efficiency, consistent with combined effects of enhancements in J_{sc} (~155 %) and V_{oc} (~9.78 %). The result is that the efficiency of this full LT μ-cell is ~190 % larger than that of the bare case. These results are well outside of statistical distributions of results from multiple μ-cells. As an example of the typical variations, Figure 5.4 (c) shows efficiencies (η), fill factor (*FF*), open circuit voltage (V_{oc}), and short circuit current (J_{sc}) measured in 20 bare μ-cells and 20 μ-cells with the LTS, ARC, and BSR.

The efficiencies are ~3.0 % +/- 0.1 % and 8.5 % +/-0.2 % for the bare μ-cell and the full LT μ-cell case, respectively. Average values of *FF* for both cases are ~71 %, with standard deviations of ~1 %. The V_{oc} values are 0.46 V +/- 0.01 V and 0.49 V +/- 0.01 V for the bare and full LT cases; the J_{sc} values are 9.8 mA/cm^2 +/- 0.01 mA/cm^2 and 24.8 mA/cm^2 +/- 0.04 mA/cm^2, respectively.

In addition to efficient materials utilization, ultrathin μ-cells enabled by LT designs and fabrication processes reported here offer other attractive attributes such as mechanical bendability when mounted on plastic substrates. The small thickness is advantageous in this context because (i) the flexural rigidity, which is proportional to the cube of the thickness, is small [23, 24], (ii) the peak strains associated with bending, which are proportional to the thickness, are small for a given bend radius [25], and (iii) the ability to heterogeneously integrate Si on plastic, for example, improves due to energy release rates for interface failure that reduce linearly with thickness [26,27]. Figure 5.5 (a) shows arrays of such thin cells printed on a thin polymeric substrate bent around a curved surface with a radius of curvature of ~2.5 mm. Figure 5.5 (b) represents the *J*-*V* characteristics of miniature modules that contain 20 μ-cells with the full LT schemes connected in parallel, in a flat state, bent along the x-direction and bent along the y-direction relative to the direction of the electrical interconnects. Changes in the illumination condition with bending lead to slight changes in the J_{sc}, but without any irreversible alteration in system performance. Bendability at this level, particularly when combined with good photovoltaic performance, efficient materials utilization and lightweight construction, could be important for many applications in portable power.

5.4 Conclusion

The methods reported here demonstrate the ability to construct monocrystalline Si solar cells that are exceptionally thin, and in bendable formats. The cavity-enhanced LT designs enable absorption of ~77 % of A.M. 1.5D illumination, even at thicknesses of ~3 microns. By point of comparison, recently reported arrays of Si microwires [28] with the same volumetric content of Si as a 2.8 μm thick planar sheets, achieve somewhat higher levels of absorption (~85 %) although at the expense of requirements for less well established routes to forming working cells with good performance characteristics. Collectively, the results suggest further opportunities for research on these and other unusual schemes [29, 30] for implementing Si in photovoltaic devices, and on related ideas in flexible inorganic photovoltaics [30-32].

5.5 Figures

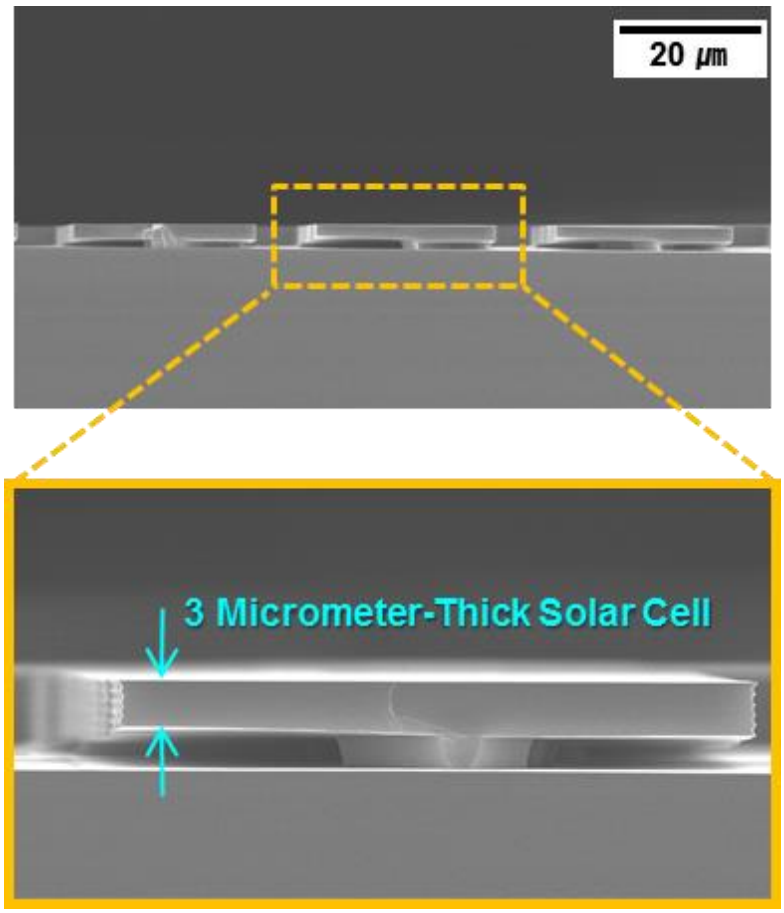

Figure 5.1 Side views of ultrathin microcells (~3 μm). Arrays of microcells after partial undercut (top). Magnified image of single microcell (bottom).

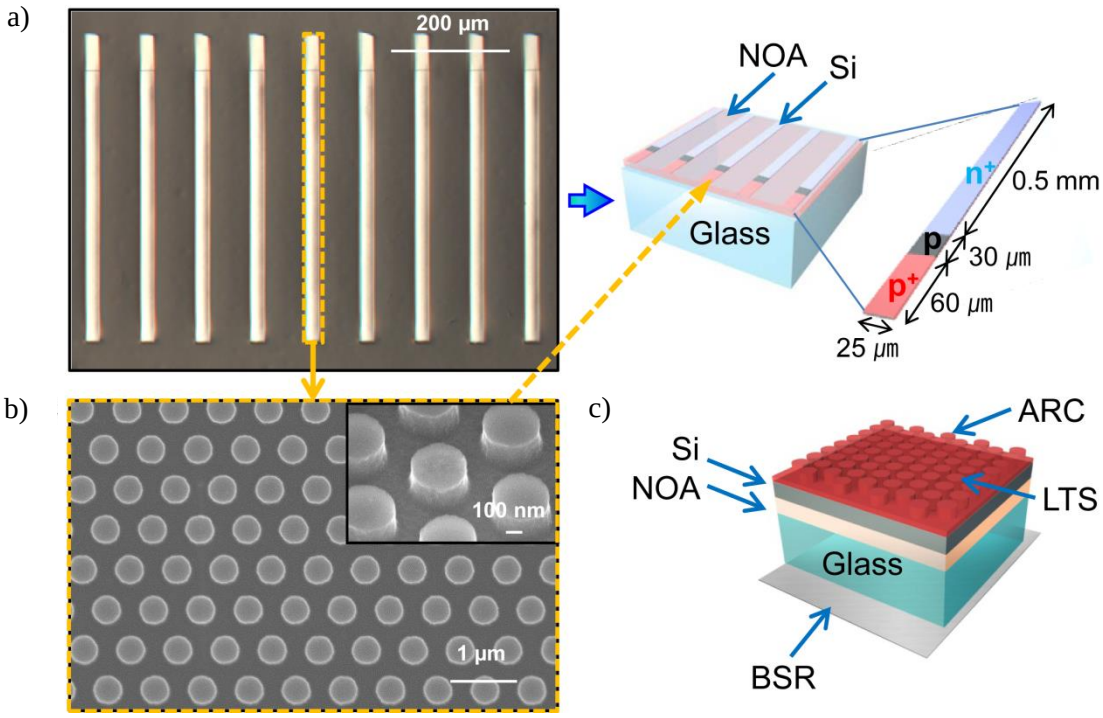

Figure 5.2 (a) Optical image and schematic diagram of arrays of μ-cells. The pink and blue areas correspond to regions of p-type and n-type doping. (b) SEM image of top surface light-trapping structures (LTSs). (c) Full light-trapping (LT) μ-cell structure, including ARC, LTS, and BSR.

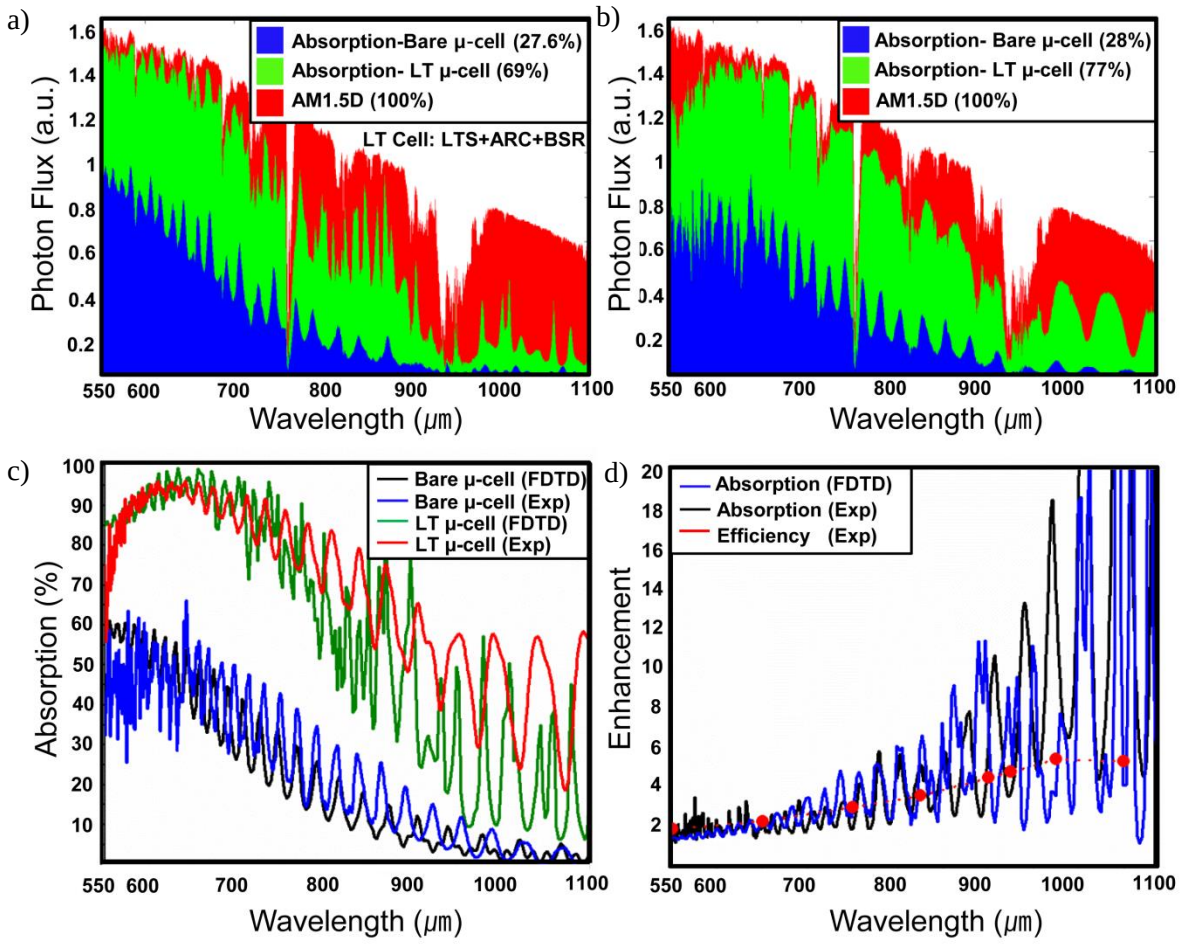

Figure 5.3 (a) Experimentally measured and (b) simulated absorbed photon flux for illumination by the AM 1.5D reference spectrum as a function of wavelength for bare Si, and bare Si with ARC+LTS+BSR. (c) Comparison of absolute absorption of a bare μ-cell and a LT μ-cell as a function of wavelength. (d) Spectrally resolved enhancement in measured and simulated absorption and measured energy conversion efficiency for a LT μ-cell and a bare μ-cell.

a)

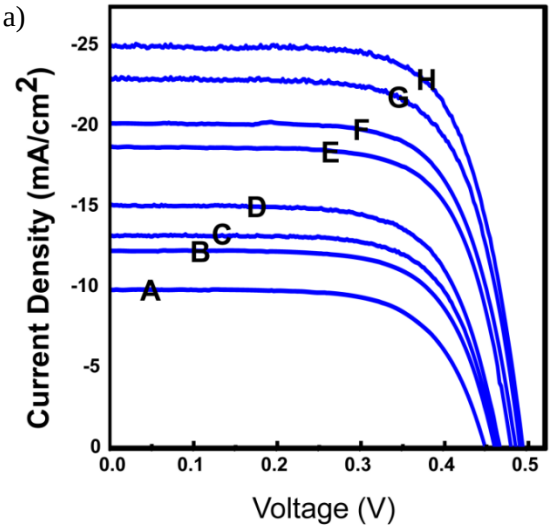

b)

	Case	J_{sc} (mA/Cm²)	V_{oc} (V)	FF (%)	η (%)
A	Bare Si	9.62	0.450	71.1	2.9
B	ARC	12.02	0.461	71.2	3.7
C	BSR	12.98	0.463	71.4	4.14
D	BSR+ ARC	14.79	0.468	70.6	4.69
E	LTS	18.39	0.481	71.2	6.13
F	LTS+ ARC	19.83	0.485	70.5	6.68
G	LTS+ BSR	22.52	0.492	71.7	7.67
H	LTS+ BSR+ ARC	24.57	0.494	71.5	8.47

c)

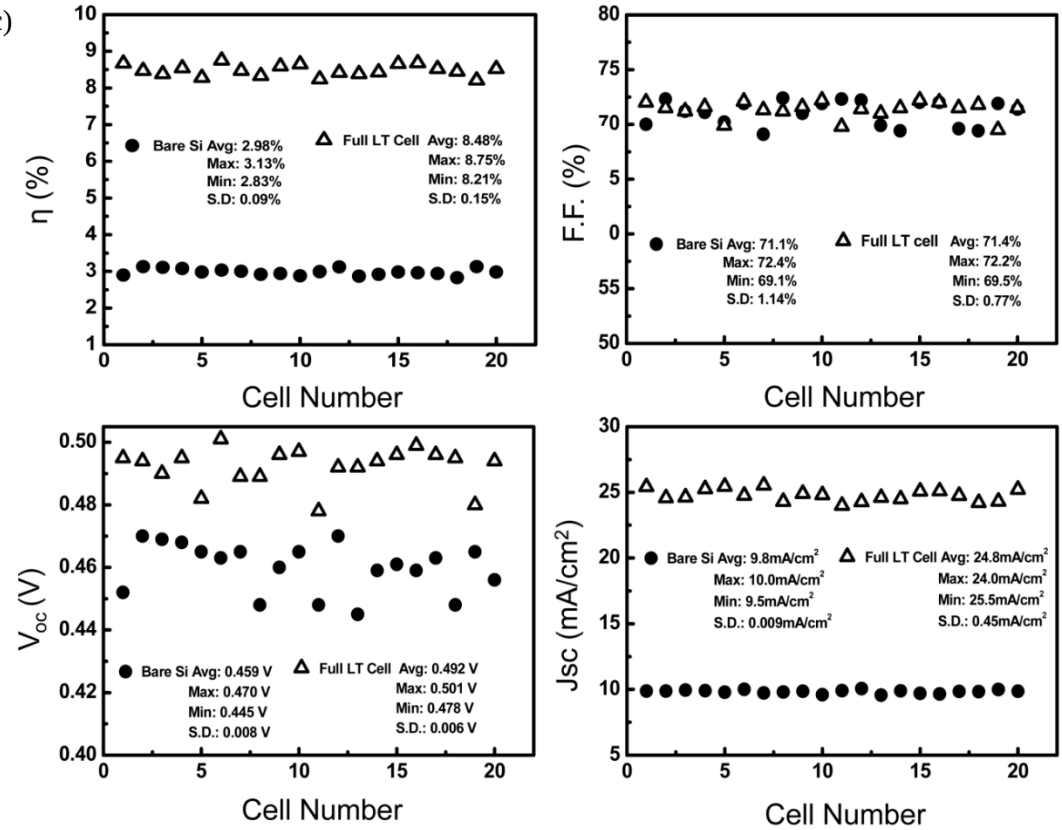

Figure 5.4 Experimentally measured (a) Current density (J)-Voltage (V) curves for μ-cells with bare Si, and with ARC, BSR, BSR+ARC, LTS, LTS+ARC, LTS+BSR, and LTS+BSR+ARC. (b) Chart of short circuit current (J_{sc}), open circuit voltage (V_{oc}), and efficiency (η) in μ-cells with bare Si, and with ARC, BSR, BSR+ARC, LTS+BSR, and LTS+BSR+ARC. Also shown is the efficiency enhancement with full LT compared to the case of bare Si. (c) Statistical variations in η, FF, V_{oc}, and J_{sc} extracted from measurements on 20 bare μ-cells and 20 full LT μ-cells.

a)

b)

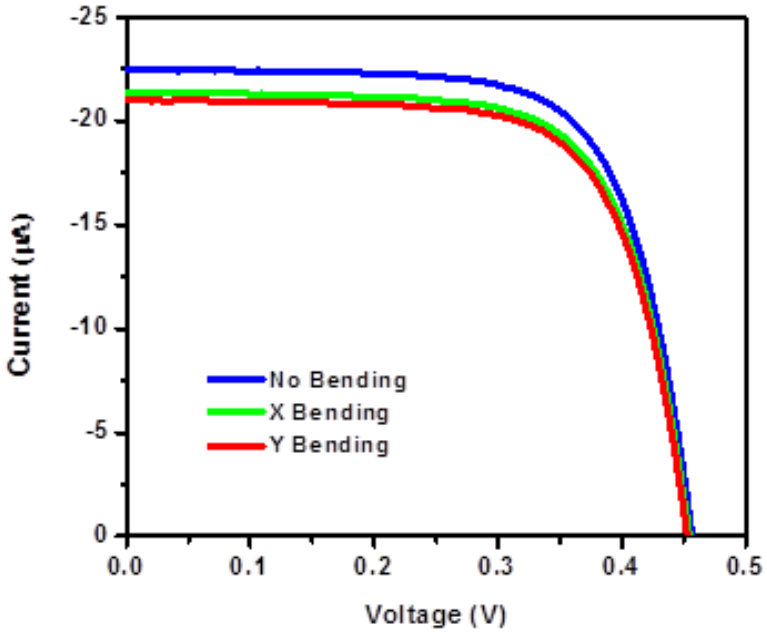

Figure 5.5 (a) Photograph of a solar mini-module consisting of 108×14 ultrathin μ-cells on a transparent substrate of polyethylene terephthalate (PET, 30 μm) wrapped onto a cylindrical support. (b) Current density (J)-Voltage (V) curves for the flat state and for bending along the x-axis and y-axis to a bend radius of 2.5 mm, for a device with 20 μ-cells with the full LT schemes connected in parallel.

5.6 References

[1] D. M. Bagnall and M. Boreland, Energy Policy **36**, 4390 (2008).

[2] M. A. Green, *Third Generation Photovoltaics: Advanced Solar Energy Conversion* (Springer, 2005).

[3] R. M. Swanson, *Photovoltaic Specialists Conference, 2005. Conference Record of the Thirty-first IEEE*. (IEEE, 2005)

[4] W. Shockley and H. J. Queisser, Japanese Applied Physics **32**, 510 (1961).

[5] C. H. Henry, Japanese Applied Physics **51**, 4494 (1980).

[6] A. Shah, P. Torres, R. Tscharner, N. Wyrsch, and H. Keppner, Science **285**, 692 (1999).

[7] L. V. Mercaldo, M. L. Addonizio, M. Della Noce, P. D. Veneri, A. Scognamiglio, and C. Privato, Applied Energy **86**, 1836 (2009).

[8] A. J. Baca *et al*., Energy Environmental Science **3**, 208 (2010).

[9] J. Yoon et al., Nature Materials **7**, 907 (2008).

[10] H. C. Ko, A. J. Baca, and J. A. Rogers, Nano Letter **6**, 2318 (2006).

[11] A. J. Baca et al., Advanced Functional Materials **17**, 3051 (2007).

[12] M. Pagliaro, R. Ciriminna and G. Palmisano, ChemSusChem **1**, 880–891 (2008).

[13] A.W. Blakers and T. Armour, Solar Energy Materials & Solar Cells **93**, 1440–1443 (2009).

[14] S. W. Bedell, D. Shahrjerdi, B. Hekmatshoartabari, K. Fogel, P. Lauro, N. Sosa, and D. Sadana, *IEEE J. Photovoltaic*, (37th IEEE 2011), pp. 228.

[15] F. Dross, A. Milhe, 1. Robbelein, I. Gordon, P. Bouchard, G. Beaucarne, and J. Poortmans, *Proceedings of the 2008 IEEE Photovoltaics Specialist Conference 2008*.

[16] F. Henley, S. Kang, Z. Liu, L. Tian, J. Wang, and Y.L. Chow, *in: 34th IEEE Photovoltaic Specialists Conference 2009*, pp. 1718.

[17] R. A. Rao *et al*., *Proceedings of the 2011 IEEE Photovoltaics Specialist Conference 2011*.

[18] K. J. Weber, and A. W. Blakers, (Aranda, Australia), Australian National University, ACT, Australia, 10432936 PCT/AU01/01546, Nov 2001, Appl. #11/193,**183**, 29 July 2005.

[19] P. J. Verlinden *et al*., Solar Energy Materials Sol.Cells **90**, 3422, (2006).

[20] D. Shir, J. Yoon, D. Chanda, J. H. Ryu, and J. A. Rogers, Nano Letters **10**, 3041 (2010).

[21] S. I. Park, J. H. Ahn, X. Feng, S. Wang, Y. Huang, and J. A. Rogers , Advanced Functional Materials **18**, 2673 (2008).

[22] O. S. Heavens, *Optical properties of thin solid films*, 2nd ed. (Dover Books on Physics, 1991).

[23] L. D. Landau, E. M. Lifshitz, *Theory of Elasticity*, 3rd ed. (Butterworth-Heinemann, 1986), Vol. 7, pp. 42.

[24] K. R. Symon, *Mechanics*, 3rd ed, (Addison-Wesley, 1971).

[25] D. Y. Khang, H. Jiang, Y. Huang, and J. A. Rogers, Science **311**, 208 (2006).

[26] A. M. Kiefer *et al*., ACS Nano **5**, 1179 (2011).

[27] J.-H. Ahn *et al*., Science **314**, 1754 (2006).

[28] M. D. Kelzenberg *et al*., Nature Materials. **9**, 239 (2010).

[29] R. J. Knuesel and H. O. Jacobs, Proceedings of the National Academy of Sciences **107**, 993 (2010).

[30] C. M. Hsu, C. Battaglia, C. Pahud, Z. Ruan, F. J. Haug, S. Fan, C. Ballif, Y. Cui, Advanced Energy Materials **2**, 628 (2012).

[31] Z. Fan *et al*., Nature Materials **8**, 648 (2009).

[32] K. Nakayama, K. Tanabe, and H. A. Atwater, Applied Physics Letter **93**, 121904 (2008).

Chapter 6. PRINTED ASSEMBLIES OF ULTRATHIN SINGLE-CRYSTALLINE SI FOR STRAIN SENSOR APPLICATIONS

6.1 Introduction

This chapter describes the piezoresistive effect in metal and semiconductor, discusses the effect of temperature and doping concentration and introduces a newly developed strain gauge using ultra-thin single-crystalline Si on plastic substrate. In general, a metal strain gauge has high flexibility with low sensitivity, whereas the semiconductor strain gauge has high sensitivity with low flexibility. Devices using thin ribbons of single-crystalline Si on plastic show gauge factor of 45 with good flexibility and repeatability. Integrating with PN diodes on the same substrate yields a large area 8 x 8 array that can be scaled up to higher density of sensing sites or used in various applications such as structural health monitoring and bio-integrated electronics for detecting motions from the human-body.

Since the discovery of the piezoresistive effects in Si sixty years ago [1], Si strain gauge has been widely used in various applications such as structural health monitoring system, bio-inspired system, pressure sensors and many others. Si strain sensor measures deformation of contact surface or motion related measurands such as pressure, flow and velocity [2]. The principle of Si strain sensors is based on the piezoresistive effect which induces the change in band gap structure. The piezoresistive effect eventually changes the resistance while external strain is applied to the Si. Metals are the most widely used materials to fabricate the strain sensors due to their mechanical flexibility and low cost production. However, they suffer from the low gauge factor, reliability, and limitation of multiplexing capability.

Recently, Si wafer-based strain sensors have been widely used due to their high gauge factor and long-term reliability. However, rigid Si wafer-based sensors are not compatible with certain applications in structural health monitoring for aircraft and in interfaces to the human body where large-area integrated networks of sensor arrays on thin deformable substrates are required. This chapter will describe the mechanically flexible network of arrays of piezoresistive strain sensors based on ultra-thin single-crystalline Si membranes on a thin plastic substrate with multiplexing capability.

The physics behind the change of electrical resistance of semiconductors is different than that of metal. When the external strain is applied to a semiconducting materials, the piezoresistive effect governs other effects (i.e., geometrical effect). There are two types of Si based on the type of impurity species (i.e., n-type and p-type Si), diffused or implanted. For the n-type Si, three pairs of valleys in the k-space are involved with the strain changes when external force is applied to Si. Each surface of valleys consists of ellipsoids of revolution located on the cube axes. All valleys are degenerated and are equally populated in the neural state. On the other hand, when the external force is again applied to Si, the symmetry of the valley structures is distorted and the carriers, in this case, electrons, are no longer in equilibrium. They will be redistributed, thereby leading to change in mobility in the conduction band. In other words, conductivity or resistivity changes as mobility changes [3]. To understand piezoresistive effect in n-type Si, the change of band structure due to the strain is analyzed. The forbidden energy gap between the conduction and valence bands is due to the interaction between moving electrons and the periodic lattice. When anisotropic stress is applied, lattice spacing along the stress direction increases, whereas spacing along two other perpendicular directions decreases. As a result, it changes the interaction of the electrons with the lattice, yielding the change of the forbidden energy gap. For example, with the compression along

the [100] direction, the minimum energy level along the [100] direction becomes lower, whereas the minima along the [010] and [001] directions becomes higher. This induces, when tensile strain is applied, the effective mass decrease which gives rise to increase in resistance. However, in contrast to the n-type Si case, hole concentrations in valence band contribute to the piezoresistive effect in p-type Si. There are two relations between the energy E and the wave number k. Large and small flatness correspond to heavy and light hole bands, respectively. As the strain is applied, heavy and light hole bands split, and holes move toward the lower bands. The effect of this redistribution of hole is large for the [111] direction where the mobility difference between heavy and light hole bands is greatest. So, p-type Si has a positive strain gauge factor, meaning positive or tensile strain along the current direction causes an increase of the resistivity. This indicates that positive strain causes the band with lower mobility to be higher with respect to the high mobility band.

We will describe basic the principle of the piezoresistive effect in doped Si. The gauge factor depends strongly on the doping concentration in Si. Reported results in Figure 6.1 show that the gauge factor (GF) increases as doping concentration decreases [4]. Based on the equation, GF is the relative change of resistance by the applied strain. Electrons in highly doped Si mostly stay in the conduction band, whereas most electrons in lowly doped Si occupy in the valence band. As the stress is applied, the energy band shifts, and this change solely depends on the magnitude of the strain. Electrons in higher energy levels move toward the lower energy level so that they reach the equilibrium state. For a large quantity of electrons in highly doped Si, the number of replaced electrons is relatively small, thereby resulting in small resistance change. On the other hand, a small quantity of electrons in lowly doped Si makes drastic change of resistance because the number of replaced electrons is high, yielding high gauge factor. This effect can explain the p-type

Si in a similar manner. The relative magnitude of hole redistribution between heavy and light hole bands is high in lowly doped Si but low in highly doped Si. In conclusion, lowly doped Si has higher GF compared to that of highly doped Si for both n-type and p-type Si cases. The p-type Si has a positive strain gauge factor, meaning positive or tensile strain along the current direction causes an increase of the resistivity or a decrease of the conductivity. On the other hand, the n-type Si has a negative strain gauge factor, thereby leading to decrease of the resistivity while positive or tensile strain is applied along the uniaxial direction.

GF also depends on the temperature. Lowly doped Si, having high GF, shows high temperature dependency. The occupation of conduction bands by electrons in n-type Si relies on the doping concentration in highly doped Si. In the same manner, the occupation of valence bands by holes in p-type Si also depends on the doping concentration in highly doped Si. Thermally excited electrons in lowly doped Si contribute greatly to the electron or the hole density in conduction bands. This induces in a low gauge factor as the relative redistribution of electrons due to the strain is reduced. Figure 6.2 shows the high temperature dependency of the gauge factor in lowly doped Si [5]. In conclusion, the tradeoff between GF and temperature dependency exists from the doping concentration. Therefore, by adjusting doping level, we can achieve relatively high GF and low temperature dependency.

6.2 Experimental

The fabrication starts with a P-type Si-on-insulator (SOI: Soitec unibond with 320-nm top p-type Si layer with resistivity of 14-22 Ω-cm). For the Wheatstone bridge and diodes, solid state doping of boron (Boron, BN-1250, Saint Gobain) and phosphorus (phosphorus, PH-1000N, Saint Gobain) at 1000 ℃ (15 min) and 950 ℃ (6 min), respectively, through patterned hard masks of SiO_2 (900 nm), produces rectifying P-N junctions and resistors. Patterning etch holes via the

photoresist layer on the device and etching the SiO_2 layer selectively through etched holes by the reactive ionic etcher are performed for lift-off membrane from the wafer. Immersing the processed wafer into hydrofluoric acid (HF) etches the SiO_2 preferentially thereby producing a freely sagged membrane tethered to the underlying wafer. The membrane can then be transferred onto Kapton® film. By patterning arrays of bridges and diodes onto the membrane, the devices can be isolated by etching away from the patterned area. Deposition of SiO_2, lithography and wet etching of PECVD-deposited SiO_2 interlayer dielectric, e-beam evaporated Cr/Au electrodes, and a layer of polyamic acid encapsulation generates the final device structure. For these particular samples, we used the mirror images of Phase II metal mask sets. Then, through an opening on the encapsulation layer, depositions of the second interconnect layer (Cr/Au), and patterning of the metal lines complete the process. Figure 6.3 shows the final device structure of an 8×8 strain sensor array transferred onto Kapton® film, and magnified images describe the individual Wheatstone bridge and diodes in the unit cell as well as the isolated bridge, leg, and diodes for individual device performance measurements. Metal lines are deposited in order to create ohmic contacts. Two additional diodes and one bridge were isolated at the left corner (those are added to extra pins) which enables measuring temperature sensitivity and individual bridge characteristics with a data acquisition system. We apply strain in x or y direction while input voltage is applied to two nodes (A and D) of Wheatstone bridge as appeared in Figure 6.4, and output voltages are measured from the other two nodes (B and C) of diagonal points.

6.3 Results and Discussion

As illustrated in Figure 6.5 (a), uniaxial tensile strain is applied in the longitudinal direction to a polyimide substrate which has a printed single μs-Si resistor of size 20 × 200 μm^2. In this configuration, the change in resistance of the μs-Si resistor at various strain levels can be

measured to extract the gauge factor associated with a printed μs-Si resistor on polyimide substrate. Electrical characteristics of the strain sensors arrays were measured. To measure the diode IV characteristics, the voltage range from the -1.0 V to +1.0 V was applied, and the good IV curve was obtained as shown in Figure 6.5 (a). We have measured IV characteristics of many diodes and all the IV curves look similar, which indicates good doping conditions. Furthermore, resistance of the strain sensor bridge elements has been measured as shown in Figure 6.5 (b). In order to get a diode with good characteristics, high doping of p and n has been done; therefore, the resistance of the Wheatstone bridge is ranged from 500 Ω to 700 Ω. This value of the resistance is relatively low and can affect the sensitivity of the device. The resistance of the μs-Si resistor varies linearly with the applied tensile strain, and the extracted gauge factor of this heterogeneous system is ~43 as shown in Figure 6.6 (a) [6]. The change in the output voltage of the μs-Si Wheatstone bridge strain gauge is measured in the same manner. Figure 6.6 (b) is the result under ±3 V input bias [6]. To predict the output voltage of a Wheatstone bridge, the following simple equation is used:

$$\frac{V_{Out}}{V_{In}} = \frac{R_4}{R_3 + R_4} - \frac{R_2}{R_1 + R_2}$$

where R denotes the in situ resistance of each bridge (i.e. μs-Si resistor) and can be calculated by

$$R = R_0(1 + GF \cdot \varepsilon)$$

where ε is the applied strain and R_0 is the initial resistance. The calculated voltage output reasonably matches experimental data, as shown in Figure 6.6 (b) [6].

In order to investigate the reliability of the μs-Si Wheatstone bridge strain gauge, the change in output voltages is measured for varying bending radii and repetitive cycles. The results in Figure 6.7 show good stability in which output voltage is constant through the repetitive cycles up to 1000 at different bending radii [6]. Temperature is the main parameter to change the device performance. In this regard, the I-V curves of isolated single diode and resistance of the bridge were sequentially measured and their behavior observed with increasing temperature. Voltage was swept from -1.0 V to 1.0 V. Figure 6.8 (a) is an optical image of diodes with metal on top. Figure 6.8 (b) shows the representative I-V curves as increasing temperature from 28℃ to 100 ℃. As demonstrated, turn-on voltage of the diode shifts to the left with increasing temperature. Increases in temperature reduce the band-gap of Si, thereby reducing the contact voltage, which induces lowering diode turn-on voltage. As well as diode properties, the resistance of the bridge resistor was measured sequentially with increasing temperature. Figure 6.8 (c) shows an optical micrograph of the bridge probed from upper left corner to lower right corner. The resistance was measured with increasing temperature from room temperature (25 ℃) to 90 ℃. Figure 6.8 (d) shows the resistance versus temperature curve. The resistance at 90℃ was increased approximately 7.7 % compared to that at 25℃. The mobility of the carriers in Si is influenced by the presence of charged impurities. With relatively low increases in temperature, the mobility of carriers is mainly influenced by impurity scattering, which lowers the mobility. However, the temperature sensitivity in both the I-V curve and resistance is relatively small.

The array functionality test was performed. When the compressive strain was applied to the device, the blue color was turned on in every 64 pixels in Figure 6.9(a). While the tensile strain was applied, the red color was turned on in the screen in Figure 6.9 (b). The yield of working unit cells was 100 %, and the device is still functional for other tasks.

6.4 Conclusion

In this chapter, basic physical principles of Si strain gauge and flexible network array of piezoresistive sensors based on ultra-thin single-crystalline Si were introduced. Strain sensors with Si as an active component showed high sensitivity and low temperature sensitivity. Furthermore, the new device consists of multiplexing diodes and Wheatstone bridges that enable continuous monitoring of strain changes of objects by making conformal contact due to its thin and flexible profile. Collectively, the results suggest further opportunities for research on these and other unusual schemes for implementing Si in flexible strain gauges for various applications.

6.5 Figures

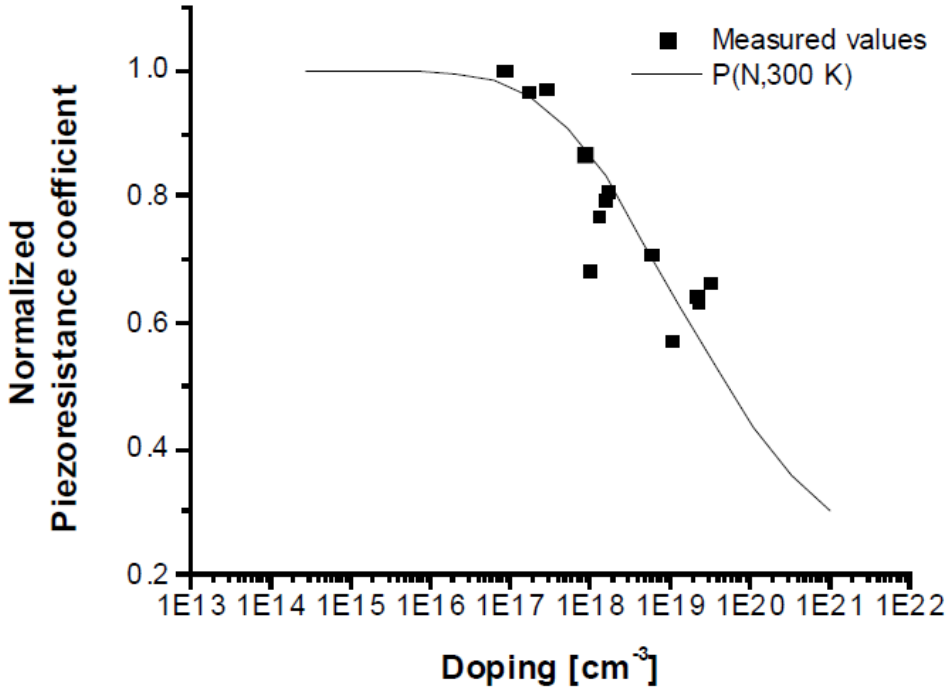

Figure 6.1 The change of normalized gauge factor of Si strain gauge at various doping concentrations. The gauge factor decreases with increasing doping concentration [4].

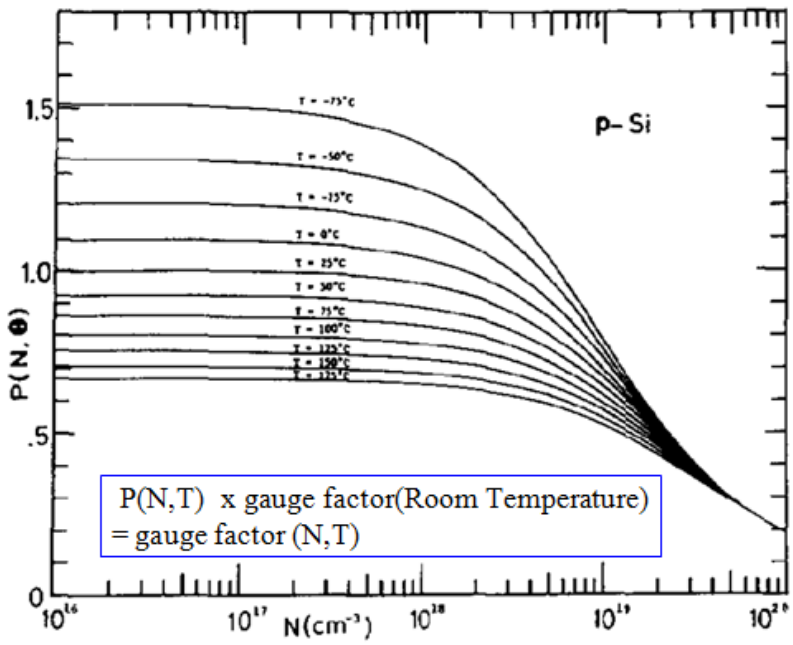

Figure 6.2 The gauge factor dependence on temperature. The factor P by which the gauge factor at room temperature should be multiplied to get the gauge factor at various temperatures is shown [5].

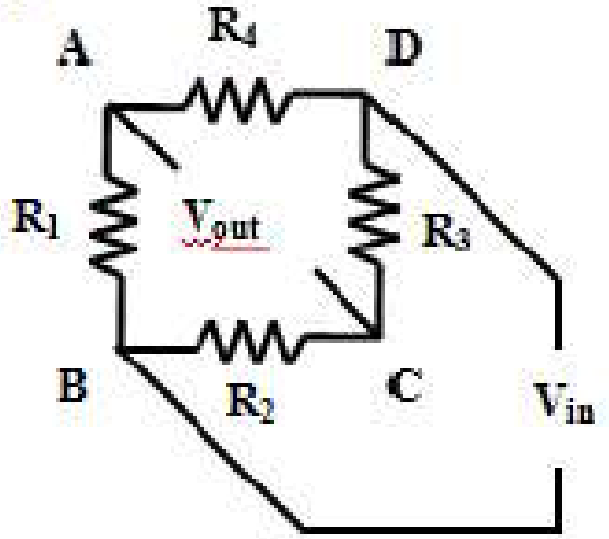

Figure 6.3 Circuitry schematic of Wheatstone bridge; with ±3 input bias at nodes B and D, the voltage difference between nodes A and C indicates the uniaxial applied strain [6].

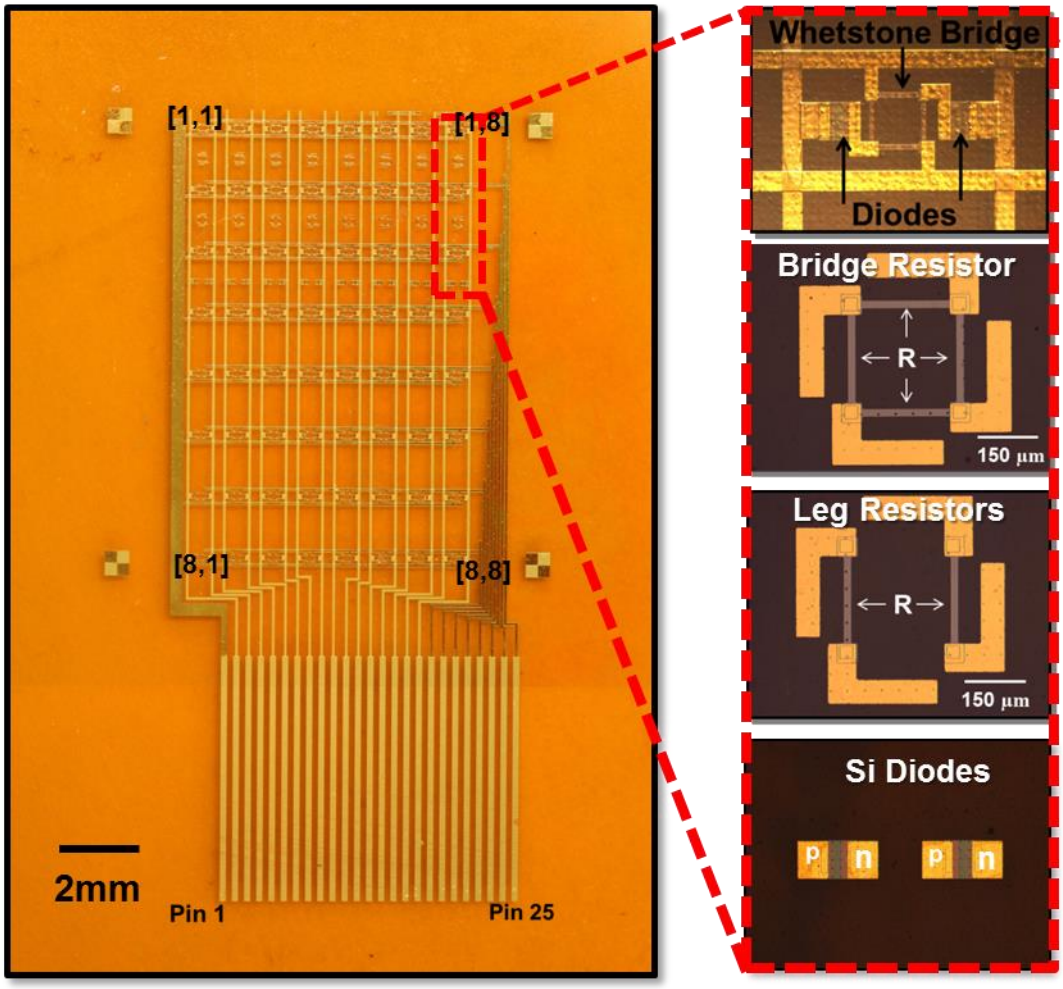

Figure 6.4 Optical image of the representative array of 8 × 8 strain gauges on a thin plastic substrate (Kapton®), and magnified images of isolated individual components.

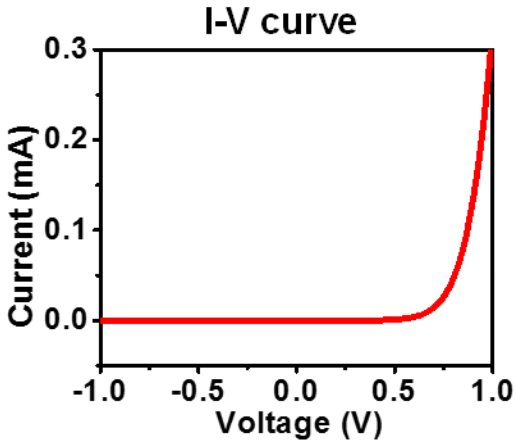

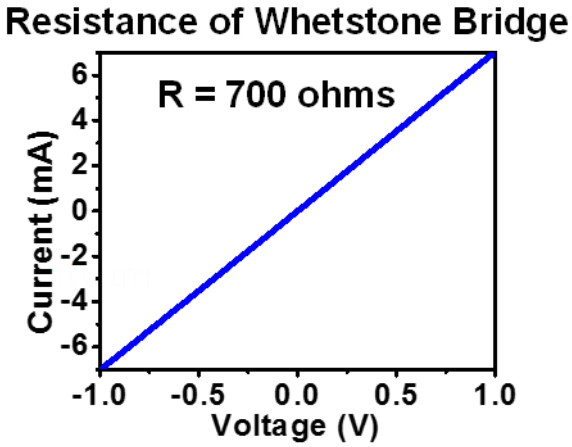

Figure 6.5 (a) Shows the voltage vs. current curves for diodes. (b) Nominal resistance of strain sensor bridge elements.

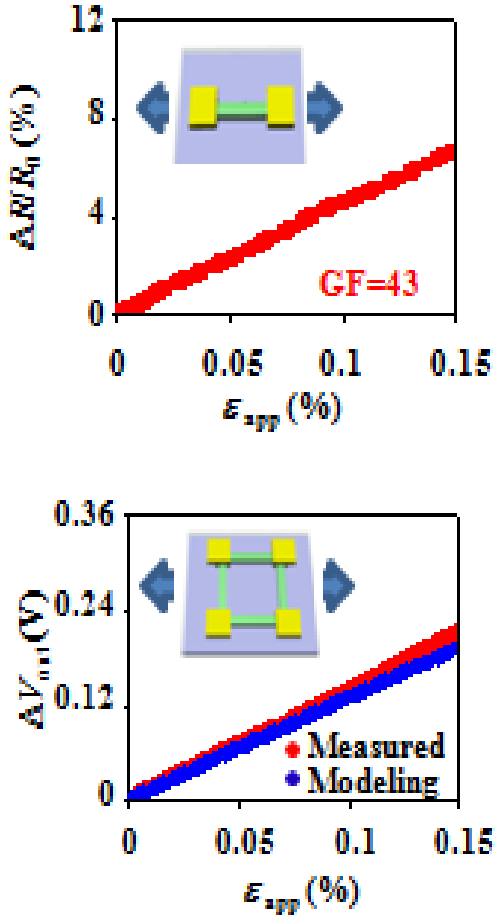

Figure 6.6 (a) Resistance change of μs-Si resistor as a function of applied longitudinal tensile strain; the slope gives the strain gauge factor of 43 [6]. (b) Voltage change of Wheatstone bridge as a function of uniaxial tensile strain [6].

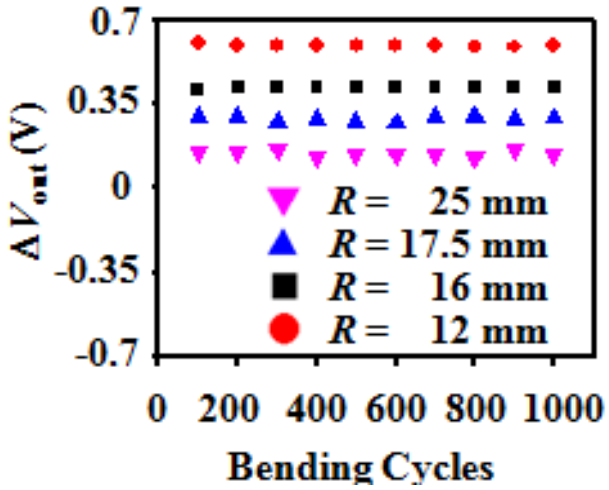

Figure 6.7 Voltage output from Wheatstone bridge during 1000 bending cycles at different radii [6].

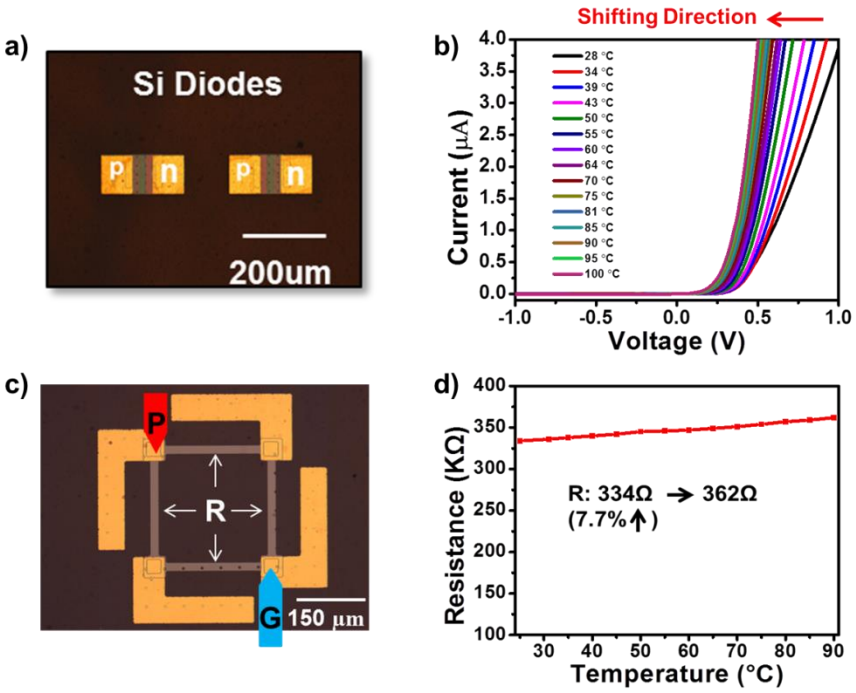

Figure 6.8 Optical image of (a) isolated diodes and (b) representative I-V curves plotted sequentially as increasing temperature. Optical image of (c) bridge resistor probed at UL(Power)-DR(Ground) and (d) representative resistance of the bridge resistor.

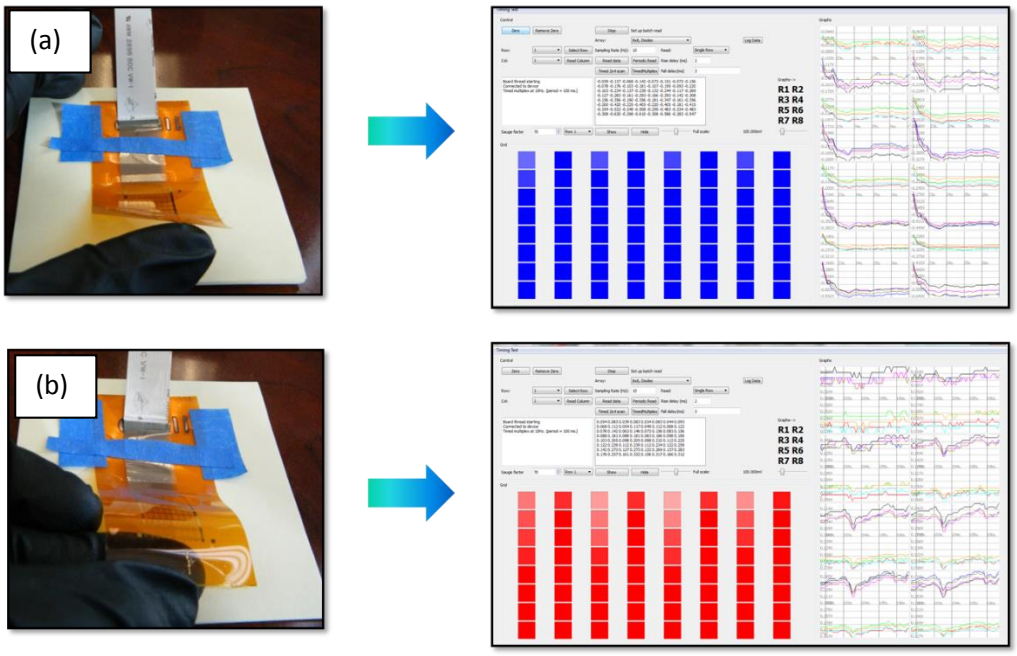

Figure 6.9 Data acquisition system results from when (a) compressive strain, and (b) tensile strain applied on the strain gauge device.

6.6 References

[1] C. S. Smith, Physical Review **94**, 42-49 (1954).

[2] S. Middelhoek and S. A. Audet, *Si Sensors* (London, UK: Academic Press, 1989).

[3] Y. Kanda, Sensors and Actuators A **28**, 83 (1992).

[4] E. Lund, *presented at MRS fall meeting* (Boston, MA, 2000).

[5] P. Norton, Solid-State Electron **21**, 969-974 (1978).

[6] S. M. Won *et al*., IEEE Transactions on Electron Devices **58**, 4074 (2011).

Chapter 7. BIORESORBABLE ULTRA-THIN SI ELECTRONIC INTERFACES TO THE BRAIN

7.1 Introduction

Bioresorbable electronic devices offer unprecedented opportunities in the deployment of advanced implantable monitoring systems that eliminate myriad risks and complications associated with surgical extraction. Applications include post-operative sensing and transient physiologic recording after percutaneous or minimally invasive placement of vascular, cardiac, orthopedic, neural or other devices. In this chapter, we apply a Si-based bioresorbable electronics technology, extending to arrays of active sensors with multiplexed addressing capabilities, for high performance electrophysiological recording from the cortical surface and the subgaleal space, *in vivo*. The key characteristic of these systems is that all of the constituent materials are physically transient, dissipated by a combination of hydrolysis, dissolution and metabolic action at the molecular level to yield products that are both soluble in biofluids and biocompatible. Demonstration experiments illustrate capabilities in the capture of normal physiologic and epileptiform activity *in vivo*, with fidelity comparable to that of standard devices in acute and chronic recordings up to 33 days. Biocompatibility studies show reduced microglial reactivity compared to conventional clinical electrocorticography (ECoG) electrodes. These results establish the feasibility of deploying bioresorbable devices for realistic clinical applications, specifically in the context of high resolution electrical recordings of brain activity. In addition to more general applicability in neural interfaces, this technology is broadly relevant across disorders where transient monitoring, and potentially modulation, of physiologic function, implant integrity and tissue recovery or regeneration are required.

Neurophysiologic monitoring is commonly used for diagnosing and treating neurological disorders such as epilepsy, Parkinson's disease, depression, chronic pain and disorders of the peripheral nervous system [1]. Such capabilities are critically important for mapping and monitoring of brain function during resective neurosurgery [2], such as for epilepsy and tumors, for assisting in neurodevice placement, such as for Parkinson's disease [3], epilepsy [4], and depression, and for guiding surgical procedures on complex, interconnected peripheral nerve structures such as the brachial, lumbar and sacral plexi. Related functionality is also increasingly leveraged during intravascular procedures, such as aneurysm coiling [5], stent placement [6], AVM embolization [7], and endoscopic operations. Post-procedure monitoring typically occurs in an intensive care unit (ICU), where a variety of devices record physiologic activity, typically with limited temporal and spatial sampling, directly at the regions of interest, simply because these are exposed and accessible during surgery. Many ICU monitors are invasive, such as epidural "bolts" and intraventricular catheters, some of which have the capability to record neurophysiology in addition to intracranial pressure. Although it would be desirable for neuromonitoring in the ICU to offer the same high fidelity, high-resolution performance as is available in the operating room, the morbidity and cost associated with additional surgeries to remove implanted recording devices preclude this possibility in general practice. In certain cases, such as in invasive intracranial electrocorticographic monitoring for epilepsy surgery, recording electrodes remain in place for one to four weeks to localize epileptic networks [8]. Here, removal occurs in a second procedure that adds cost and risk but is nevertheless justified by the ability to make patients seizure-free. An ideal scenario would involve placement of temporary, bioresorbable monitoring devices capable of providing continuous streams of data for guiding medical care. This chapter presents a class of technology that offers this mode of operation for neural recording, with

performance that matches or exceeds any existing alternative, in formats that are fully biocompatible, throughout their life cycle.

The platform builds on recently described technologies that exploit nanomembranes of device-grade, monocrystalline Si (Si NMs) as the semiconductor foundation of a high performance class of electronic systems with potential utility in this context. The ramifications range from the ability to monitor and influence patient health and recovery after surgery or injury, to the capacity to verify the success of a procedure or the integrity of a graft, repair or intervention in a specific application. In addition to their established bioresorbability, the nanoscale thicknesses of Si NMs, when deployed with thin substrates, interconnect metals and dielectrics, yield devices with levels of mechanical flexibility necessary for conformal contact and chronically stable interfaces with neural tissues. The following content describes means to exploit these concepts in materials, devices and system-level examples of bioresorbable Si electronic interfaces to the brain, with examples in passive and active matrix addressed recording *in vivo* and quantitative comparisons to standard electrode arrays. Evaluations include capture of electrocorticograms (ECoG) and subdermal encephalograms (EEG) in live, awake animal models, where Si NMs serve as active materials not only for the recording interface but for the backplane transistors needed for high-speed multiplexed addressing across arrays of channels. Comprehensive *in vitro* and *in vivo* studies establish that these systems provide accurate and reproducible measurements of neural signals and physiological activity for acute (~hours) and chronic (up to 33 days) use. Biocompatibility studies reveal no overt tissue reactions compared to clinically approved commercial ECoG electrodes (by Adtech Inc).

7.2 Experimental

Two types of devices, bioresorbable 4-ch passive electrodes and 64-ch actively multiplexed electrodes, for the neural recording *in vivo* application will be introduced in this chapter.

Fabrication of passive electrode arrays

Fabrication of the passive electrode arrays began with solid state phosphorus doping (PH-1000N Source, Saint Gobain, USA, 1000 ℃ for 10 minutes) of p-type device Si on a Si-on-insulator (SOI, top Si ~300 nm, SOITEC, France) wafer. Removing the buried oxide layer of the SOI by wet etching with concentrated HF released the device Si as a Si nanomembrane (Si NM), retrieved with a slab of the elastomer poly(dimethylsiloxane) (PDMS) and transfer-printed to a spin-cast bilayer of poly(methylmethacrylate) (PMMA, ~ 800 nm thick) and polyimide (PI, ~300 nm thick) on a Si wafer. Photolithography and reactive ion etching (RIE) defined a pattern of electrodes and interconnects in the Si NM. Plasma enhanced chemical vapor deposition (PECVD) formed a layer of SiO_2 (thickness 100 nm) as encapsulation. Patterned etching with buffered oxide etchant removed the SiO_2 from the electrode regions. Spin casting and patterning a top coating of PI (~300 nm thick) placed the Si NM electrodes and interconnects near the neutral mechanical plane. Patterning a mesh structure across the multilayer (i.e. PI, SiO_2, PI and PMMA) by RIE and buffered oxide etchant allowed removal of the base layer of PMMA by immersion in acetone. Retrieval onto a slab of PDMS removed the bottom exposed layer of PI by RIE. Transfer onto a film of PLGA (~30 μm thick), facilitated by heating to temperatures close to the glass transition of the PLGA (55~60 ℃, lactide/glycolide ratio of 75:25 composition), followed by elimination of the top layer of PI by RIE, completed the fabrication. Bonding an ACF cable to the terminal

regions of the Si NM interconnects yielded connection points for interfaces to external data acquisition (DAQ) systems. A detailed fabrication schematic flow is provided in Figure 7.1.

Fabrication of actively multiplexed electrode arrays.

The fabrication began with growth of 200 nm of thermal oxide on a p-type SOI wafer (top Si ~320 nm, SOITEC), photolithography and etching in buffered oxide etchant to create a mask for solid state phosphorus diffusion (1000 ℃ for 6 minutes) to define the source and drain contacts. Releasing, retrieving and transferring the doped Si NMs onto a temporary substrate, consisting of Si wafer with a bilayer coating of PI/PMMA, followed procedures similar to those described for passive electrode arrays. Photolithography and RIE etching patterned the Si NMs into geometries for an 8x8 array of unit cells, each consisting of two transistors connected in series for purpose of actively multiplexed readout. A thin layer of SiO_2 (PECVD at 220 ℃, thickness ~100 nm) served as the gate dielectric. Buffered oxide etching through a photolithographically patterned mask formed openings through the SiO_2 to expose the source and drain contact regions. Photolithography and lift-off in acetone defined a patterned layer of Mo (sputter deposited, thickness ~300 nm) to define the gate electrodes and metal interconnects. Deposition of a trilayer of SiO_2 (300 nm)/Si_3N_4 (400 nm)/SiO_2 (300nm) by PECVD formed the interlayer dielectric. Photolithography and buffered oxide etching created vertical interconnect access (via) holes for electrical connections between layers. An additional layer of Mo (thickness ~300 nm) patterned by photolithography and liftoff defined column select lines. Another trilayer of SiO_2 (300 nm)/Si_3N_4 (400 nm)/SiO_2 (300nm) served as encapsulation, with openings at the locations of the sensing electrodes and peripheral contact pads for interfacing to an external DAQ system. Spin-casting of a diluted PI created a layer for device passivation. Selective RIE and buffered oxide

etching through entire layer stacks (diluted PI/trilayers of inorganic materials/trilayers of inorganic materials/Diluted PI) formed mesh structures that enabled release of active layers from the temporary substrate by dissolving the PMMA layer in acetone. Transfer printing steps followed, according to procedures similar to those for the passive electrode fabrication.

7.3 Results and Discussion

Materials, designs and *in vitro* measurement of a bioresorbable passive neural electrodes

Figure 7.2 (a) provides an exploded schematic diagram (left) a magnified optical microscope image of the active sensing and the passivation regions (right) of a simplest embodiment of these concepts: a thin, flexible electrode array based on a phosphorus doped (impurity concentrations: ~ 10^{20} /cm^3) collection of Si NM (thickness ~290 nm) structures. Here, a layer of SiO_2 (thickness ~100 nm) insulates the connection traces to isolate them from bio-fluids and adjacent tissue. The terminal pads consist of exposed Si, as the direct neural interface. A flexible sheet of the bioresorbable polymer poly(lactic-co-glycolic acid, PLGA, thickness ~30 μm) serves as the substrate. This array (3 mm × 4 mm) allows chronic recordings from rat cortex at four measurement sites, each with dimensions of 250 μm × 250 μm. Figure 7.2 (b) shows micrographs of completed arrays. Placing an array onto a hydrogel substrate (Figure 7.3 (a)) and immersing the system in phosphate-buffered saline (PBS) at physiological pH (7.4) and at room temperature enables characterization of each of the electrodes by electrochemical impedance spectroscopy, measuring the low local field potential range (LFP: 1 Hz to 100 Hz, using a Gamry Reference 600 potentiostat and EIS 300 frequency analyzer). In the recording of brain signals, the electrodes perform the function of transduction from the ionic currents in the electrolyte to an electric current in the measurement system. The electric contact between an electrode and tissue makes electric

impedance. Lower impedance increases the current level, which gives rise to a higher signal-to-noise ratio (SNR) and lower signal distortion. The data in Figure 7.3 (b) correspond to the impedance (|Z|) of each channel in the array, along with the response of a gold (Au) electrode with the same dimensions. The phase responses show consistent behavior, i.e. capacitive (~90°) for Si at all frequencies. Values across the different channels are all similar at all frequencies. To better understand electrochemical characteristics of Si, EIS data were fit to an equivalent Randles circuit model (Figure 7.4 (a)), which can be expressed by a double layer capacitance (C_{PE}), in other words, a constant phase element, in parallel with a charge transfer resistance (R_{CT}), together in series with a resistance (R_S) of the phosphate-buffered saline or bio-fluids. An ionic layer on the solution side establishes two layers of charges, interfacial capacitance (double layer capacitance, C_{PE}), between the solid surface and solution, which mainly changes the impedance values. The statically charged region at the solid/electrolyte interface is composed of a space charge layer in the solid and double layer in the electrolyte. The fitting results are plotted in Figure 7.4 (b). The model provides a good fit for impedance results for both Au and Si electrodes. Typical values of C_{PE} of metals and Si are ~10-20 $\mu F/cm^2$ and ~1-3 $\mu F/cm^2$, respectively [9]. Two main parameters to determine the impedance are C_{PE} and R_{CT} since W and R_S are negligible. The fitted C_{PE} values (Si: ~2.5 $\mu F/cm^2$, Au: ~10 $\mu F/cm^2$) of Si and Au in Figure 7.4 (c) correspond well to those reported in the literature. Interfacial charge distribution in C_{PE} between semiconductor and electrolyte is lower compared to that between metal and electrolyte. Thus, in general, metal has higher C_{PE} values. Results of impedance measured on devices constructed using Si NMs with different dopant species and concentrations (phosphorus, between ~10^{17} and ~$10^{20}/cm^3$; and boron, at ~$10^{20}/cm^3$) show similar values at all frequencies (Figures 7.5 (a) and (b)). As a result, the doping concentration does not strongly affect neural recordings because the relevant data occur in the physiological frequency

range. However, we used highly doped Si in order to achieve slower dissolution of Si in biofluids for the chronic neural recording. The impedance results using Si NMs with different thickness imply continuous similar value at all frequencies as well (Figure 7.6 (a)). This result implies continuous reliable neural recording with the Si electrodes even if the electrodes dissolve over time. The impedance decreases, as expected, inversely with the areas of the electrodes (phosphorous, ~10^{20}/cm^3), as illustrated in the data of Figure 7.6 (b) for dimensions of 200×200 μm^2 (A1), 300×300 μm^2 (A2), 400×400 μm^2 (A3), 500×500 μm^2 (A4). Further increases in area can be achieved using surface roughening or nanoporosity in the Si NMs, with corresponding benefits in impedance (SNR).

The key attribute of these electrodes is their bioresorbability. The slow, controlled dissolution of Si NMs is advantageous in this context. (Coating the Si with metals [10-13], as a standard approach to low impedance contacts, is not applicable for present purposes due to the fast dissolution kinetics of most bioresorbable metals.) Si dissolves under physiological conditions by hydrolysis to yield silicic acid, at rates that depend strongly on ionic content of the surrounding solution, pH, temperature and other factors, including the doping level. Specifically, Si forms neutral ortho-silicic acid $Si(OH)_4$ through an initial oxidation step to SiO_2 or through a direct equilibrium $Si+4H_2O \leftrightarrow Si(OH)_4 +2H_2$ [14, 15]. Figure 7.7 illustrates the dissolution kinetics for highly boron and phosphorus doped (concentration of ~10^{20} /cm^3) Si NMs (~300 nm thick) in artificial cerebrospinal fluid (aCSF, pH 7.4) at physiological temperature (37 ℃), evaluated by measuring the thicknesses at different time points by profilometry (Dektak, USA). Observations indicate that dissolution occurs in an exceptionally controlled, predictable process, without cracks, flakes, particulates or reduction in surface smoothness that often occurs in dissolution of metals. The dissolution rate exhibits a constant, thickness-independent value of ~11 nm/day as shown in

Figure 7.7 (a). These characteristics make doped Si NMs an excellent choice for neural interfaces, by comparison to biodegradable metals or other alternative materials. The dissolution characteristics of the other materials in the system, which for the case of the simple device in Figure 7.1 (a) are SiO_2 and PLGA, are also important, although less critical than the Si NMs due to their passive role in the device operation. Measurements indicate that SiO_2 and PLGA (75:25) dissolve in biofluids at 37 ℃ at rates of ~8.2 nm/day (Figure 7.7 (b)) and complete dissolution time scales of 4-5 weeks [16], respectively. Accelerated dissolution tests appear in Figure 7.8 as a series of images of a complete device collected at various times after immersion in PBS pH 10 at 37 ℃. We anticipate that the current device design material choices allow complete dissolution of the device in 2 months in biofluids pH 7.4 based on the dissolution rates of the materials. Si and SiO_2 will be dissolved first within a month and 2 weeks, respectively, followed by PLGA. PLGA will be dissolved in 4-5 weeks. The material parameters (i.e., thicknesses, doping levels for the Si, and ratio of lactide to glycolide for the PLGA) can be adjusted to achieve desired dissolution times.

For conformal contact against the curved surface of the brain, mechanics are important. Three dimensional-finite element modeling (FEM) reveals distributions of principal strain for bending perpendicular to the interconnect direction, as in Figure 7.9 (a). Based on the layouts and the mechanical moduli, the maximum strains in the SiO_2, Si and PLGA are less than 0.03 % for a bending radius of 1 mm, corresponding to the linear elastic regime for each of these materials. An optical image of a device wrapped around a glass rod with a radius of curvature of ~2 mm appears in Figure 7.9 (b). Measurements before and after bending show negligible differences in impedance (Figure 7.10), consistent with expectation based both on FEM and analytical modeling results.

Neural Recordings with Passive Bioresorbable Electrodes

In vivo and *in vitro* neural recording experiments used the bioresorbable devices of Figure 7.1 in adult rat animal models and in hippocampal slices (Figure 7.11) respectively. We were able to record the brain signals for both pipettes and Si electrodes. *In vivo* experiments on anesthetized rats exploited a stereotaxic apparatus to hold the head in a fixed position. A craniotomy exposed a 4×8 mm region of cortex in the left hemisphere (Figure 7.12 (a)), to allow positioning of a device on an area of the cortical surface next to a standard stainless steel microelectrode (7,850 μm2) as a control for recording physiological oscillations induced by isofluorene anesthesia. Figure 7. 12 (b) shows representative sleep spindle activity captured by one of the channels in the bioresorbable array and the control electrode. The amplitude of the activity recorded by the control electrode is larger due to low impedance and penetration to the cortical tissue (~0.5 mm from surface). Figure 7. 13 (a), (b) show similar data for brain waves recorded during transition to deep anesthesia and K-complexes measured under anesthesia. Representative examples of inter-ictal and ictal-like spiking epileptiform activity induced by application of crystals of bicuculline methiodide recorded by the bioresorbable electrode and the control electrode appear in Figure 7.12 (c) and (d), respectively. The frequency of the inter-ictal spikes (Figure 7.12(c)) increases and the inter-spike duration decreases as the time progresses, terminating into ictal-like early epileptic discharges (Figure 7.12 (d)). Competing effects of the neurotoxin and anesthetic agent likely prevented observation of prolonged seizures. The bioresorbable arrays can also be utilized as subdermal implants for high fidelity, recording of EEG and evoked potentials. Devices implanted on periosteum as described in Figure 7.14 (a) and (b) yielded reliable recordings of theta waves (highlighted in power spectral analysis) and sleep spindles (Figure 7.14 (c)). Collectively, the

results demonstrate that bioresorbable recording platforms yield reliable physiological or pathological activity both intracortically and subdermally.

Chronic tests of ECoG recording indicate long-term stability in operation, where devices with increased thicknesses of SiO_2 (300 nm) and Si NMs (1000 nm) survive for more than one month. Such studies used a miniature interface board connected to the device via a flexible interconnect cable (Figure 7. 15) to a headstage designed for use with rats. Details appear in the Methods section 7.5. Figure 7.16 (b-f) summarizes representative cortical potentials recorded by three electrodes in the bioresorbable array and by a nearby screw electrode as a control, captured on Days 1, 8, 15, 30 and 33 measured from the time of the surgical implantation. Figure 7.15 and Figure 7.16 (a) describes the surgical setup. ECoG potentials show physiological signals and brain oscillations with various temporal and spatial differences. After day 33, signals from the bioresorbable device disappear, while those the control persist, consistent with dissolution of at least some critical component of the device. High-amplitude seizure-like rhythmic spike discharges appear occasionally, consistent with absence-like seizure activity observed in Long-Evans rats [17-19]. The clinical patient intracranial recordings are usually performed for 2-4 weeks to determine the seizure focus before epilepsy surgery. Longer recordings are not preferred due to potential risk of infection. Therefore, we designed bioresorbable ECoG arrays to record for one month in chronic rat experiments. Additional engineering improvements hold promise for further extending the operational lifetime.

Biocompatibility analysis

Understanding the reactive tissue response to implantable systems of the type introduced here is critical in assessing their potential for clinical applications [20]. Tissue inflammation, encapsulation of the electrodes in fibrous tissue (glial scar) and neuronal death in the vicinity of the electrode are the most important issues related to the stability and longevity of long-term neural recordings and their clinical translation [21-23]. Studies of tissue reactions to bioresorbable electrode arrays involved chronic implants in 14 animals with the bioresorbable arrays and with Pt electrodes, as controls, cut into similar geometries from clinical subdural grids (Ad-Tech Medical Inc), as shown in Figure 7.17. Figure 7.18 summarizes the results for immunohistochemistry analysis for the bioresorbable and the control electrodes, performed according to procedures outlined in the methods section. Double label immunohistochemistry for GFAP and Iba-1 reveal glial cell activation at 4 weeks post-implant (Figure 7.18). In both control and bioresorbable array groups, moderate subpial gliosis occurs at the implantation site, when compared to the control contralateral hemisphere. No significant astrogliosis is noted at distant sites within the ipsilateral hemisphere. Iba-1 immunohistochemistry demonstrates the presence of both resting ramified, as well as round activated microglia underneath the control electrode, which extends to the superficial layers I-III. In contrast, at the implantation site of the bioresorbable electrode, microglial cells show an almost exclusively ramified morphology. The contralateral side in both groups exhibits no microglial reaction. The sham-operated control demonstrates a similar moderate subpial gliosis, but with no change in microglial densities or morphology.

Materials, designs and *in vitro* measurement of bioresorbable, 8×8 channels, actively multiplexed neural electrodes

Active multiplexing schemes enable high-resolution, high channel count neural interfaces by minimizing the number of wires needed for external data acquisition. In this context, Si NMs provide an excellent choice not only for the electrodes but also for the backplane electronics, including the necessary switching and buffer transistors. A fully bioresorbable design appears in an exploded view schematic illustration in Figure 7.19 (a); a sequence of optical microscope images at various stages of the fabrication appears in Figure 7.19 (b) (left). This embodiment uses 64 n-channel metal-oxide-semiconductor field-effect transistors (MOSFETs), with Mo for the source, drain and gate electrodes, and SiO_2 (100 nm) for the gate dielectrics. Additional layers of Mo and a trilayer of SiO_2 (300 nm)/Si_3N_4 (400 nm)/SiO_2 (300 nm) form interconnects and interlayer dielectrics (ILD), respectively. A second layer of Mo (300 nm) serves as column selects and additional sensing electrode pads. Another trilayer provides a blanket encapsulating layer that has openings only at the locations of the Si interface electrodes. The chemistry, dissolution kinetics and biocompatibility of each of the constituent materials can be found elsewhere [24-28]. Fabrication occurs on a temporary substrate. Techniques in transfer printing enable integration onto substrates of PLGA. Details on all processing steps appear in section 7.5. Figure 7.19 (b) (right) presents photographs of a representative device, wrapped around cylindrical tube, with an inset that shows arrays of active electrodes. Figure 7.20 (a) and (b) summarize the electrical properties of a representative n-type MOSFET, where the mobility and on/off ratio are ~400 $cm^2 V^{-1}$ and ~10^8, respectively, as calculated from the slopes of the transfer curves and the ratio of maximum and minimum current outputs using standard field-effect transistor models. Figure 7.21 summarizes the key aspects of the designs of circuits that incorporate these transistors for

multiplexed addressing. The approach involves two transistors per unit cell [29] (Figure 7.21 (a)), in which a buffer transistor connects to the interface electrode to provide buffering of measured biopotentials, and a multiplexing transistor allows electrodes in a given column to share a single output wire. The surface electrodes appear in the top layer, where they come into physical contact with the brain; they connect to the underlying backplane circuit through vertical interconnect access holes (vias). An active shielding scheme described in Figure 7.21 (b) greatly reduces the parasitic capacitance between electrodes and increases the gain of each. Figure 7.21 (c) shows the dimensions of a unit sensor and an overall device. Figure 7.22 shows *in vitro* measurements on a representative unit cell. The operation involves successive application of 3 V (V_r) to the gate of the multiplexing transistor as a row select operation, 4 μA (constant current) and 3 V (V_c) to the source electrodes of the two transistors in the column select, and 0 V (V_e) to the ground lines. The output (V_e) from the objective represents the signal, where V_r, V_c, and V_e correspond to voltages from row select, column select and sensing electrodes, respectively, after biasing to 200 μV (peak to peak) with a frequency of 50 Hz and a sinusoidal waveform from reference electrodes immersed in PBS at pH 7.4 (Figure 7.23). The output response is consistent with the input, indicating proper operation. Figure 7.24 shows the switching property of a single unit sensor by application of +/-3 V (+3 V: on, -3 V: off) to Vr. During multiplexed sampling, driving the row select signal selects a single row of electrodes at a time. This scheme allows the unit cells in the corresponding row to drive the column output lines which connect to a high-speed analog-to-digital converter. Row select signals are rapidly cycled to sample all electrodes on the array. The entire device connects to an external data acquisition (DAQ) system through a connector with 26 contacts. Figure 7.25 shows a sequence of images during accelerated dissolution in PBS pH 12 at 37 ℃. PECVD Si_3N_4 and Mo dissolves in biofluids at pH 7.4 at 37 ℃ at a rate of ~5.1 nm/day as shown in Figure 7.7

(b) and ~16-25 nm/day [24]. This system involves 1.3 µm, 800 nm, 290 nm, 600 nm and 30 µm thick layers of PECVD SiO_2, Si_3N_4, Si, Mo and PLGA, respectively. PLGA, Si, and Mo in biofluids at 37 ℃ dissolve completely within in ~4-6 weeks. Both SiO_2 and Si_3N_4, dissolve in 6 months under the same conditions.

Figure 7.26 shows the gain mapping result and leakage current of the multiplexed array by submerging the device in PBS pH 7.4 prior to implanting the device. The average gain and yield are 97% and 100%, respectively. Leakage current level is ~ 10 nA. A 64-electrode array connected to DAQ preamplifer boards was placed on the cortical surface of the left hemisphere of an anesthetized rat placed in a stereotaxic apparatus. Figure 7.27 shows a 64-channel electrode array and control electrode placed onto the left and right hemispheres of rat brain, respectively. Figure 7.28 provides details on *in vivo* recordings with the bioresorbable multiplexed array. Picrotoxin was applied topically to induce epileptiform activity before the placement of the array. Epileptic activity induced by picrotoxin affects a large number of neuronal populations spreading across the rat cortex and is detected simultaneously by the individual electrodes in the multiplexed array. Seizure-like oscillations were observed, lasting 1–2 s and repeating every 10-15 s. A set of different epileptic spikes (clockwise spiral, lower right to upper left diagonal, upper left to lower right diagonal, and right to left sweep), representative of the recordings from 64 channels, is shown in Figure 7.28 (a). The sequences of eight movie frames corresponding to each spike activity clearly show the motions of the neural waves and spatio-temporally resolved patterns in Figure 7.28 (b). Band-pass filtering the spiral wave data yields corresponding delay plots for each spike activity that are consistent with spiral waves in Figure 7.28 (c). Each spiking activity provides a good singularity as indicated by the yellow arrow in each movie frame. RMS power spectra, corresponding to each spike activity, is provided in Figure 7.29.

In addition to epileptiform activity, spatial distributions of low amplitude evoked cortical activity can be captured using the same device and animal models. Somatosensory evoked potential (SSEP) experiments were conducted in anesthetized rats without drug application (Fig. 7.30 (a)-(d)) using the bioresorbable multiplexed array on the surface of the exposed barrel cortex. Evoked potentials were produced by stimulating a single whisker and recorded. Two different whiskers were stimulated to study the spatial distribution of evoked potentials across barrel cortex. The spatial distribution of the amplitude of the evoked potentials measured at the cortical surface by the array is consistent with the relative location of the activated whiskers on the barrel cortex as described with the color map (Fig. 7.30 (d)). These results collectively demonstrate an ability to record stimulus evoked and drug-induced neural activity with high SNR in the LFP band. The same materials and device architectures can be easily adapted to increased areas and channel counts with potential for use in other animal models and, in the future, for clinical monitoring applications.

7.4 Conclusion

The concepts in materials, fabrication and characterization methods introduced here create possibilities for application of bioresorbable implantable electrode technology for various clinical problems, ranging from post-operation monitoring of brain activity to electrical monitoring of skeletal muscles or organ function. For ECoG monitoring after brain surgery, resorbable arrays can transform clinical practice by eliminating the need for a second surgery for the implant removal. *In vivo* studies presented in this chapter show great promise for feasibility of long-term chronic recordings and biocompatibility of the bioresorbable electrode technology. Future designs might incorporate electrical stimulation and drug release capabilities in addition to higher density of

electrodes to improve the spatial resolution of monitoring neural activity. Development of new techniques to deploy bioresorbable electrodes to internal organs of the body through catheters, injectors or endoscopes can provide additional areas of opportunity for a wide range of clinical monitoring applications.

While the above discussion focuses primarily on devices focused on neurological disorders, dissolvable implantable devices easily port to applications outside of the brain and peripheral nervous system. Examples might include implantable sensors to measure and guide therapy after joint replacement, dissolvable pacing wires after cardiac surgery, and devices to measure and modulate flow in a number of different organs in the pulmonary, renal and digestive system, to name a few. Because these devices, including substrate, wires and contacts are resorbed after their job is done, and need not be removed, complications due to surgical removal or chronic foreign body reactions are eliminated.

Bioresorbable implantable systems can offer new, efficacious means for monitoring patient condition and delivering therapy throughout the cycle of care after or before the surgery. In addition to dissolving, the devices we report perform their function with minimal invasiveness (e.g. minimal mechanical injury) due to their thin, flexible profile. At the end of their lifespan they are resorbed by the body and only the connector attached to the skin surface needs to be removed. The small surface wound could be closed or sealed with steri-strips and left to granulate in, while all implanted components dissolve. Here, use of Si nano-membranes for the active components of devices is particularly promising for future integration with high performance CMOS chips. In addition, Si offers the advantages of biocompatibility, slow and predictable dissolution kinetics and absence of flaking or cracking during dissolution, in contrast to other metal alternatives.

7.5 Method

In vivo acute recordings

The *in vivo* data Fig. 7. 12 is representative of four different acute experiments, each of which lasted 5-6 hours. The procedures, which were approved by the Institutional Care and Use Committee of the University of Pennsylvania, involved an anaesthetized rat with its head fixed in a stereotaxic apparatus. Wild-type, adult Long-Evans male and female rats were used. The animal was anesthetized initially with ketamine/xylazine and then isoflurane throughout the craniotomy and neural recordings. A craniotomy exposed a 4x8 mm region of cortex in either left or right, or both hemispheres. All recordings were taken in reference to a distant stainless steel bone screw inserted through the skull during the surgery. A commercial stainless steel microwire electrode (100 µm stainless steel wire from California Fine Wire) placed at 0.5 mm depth from the cortical surface in close proximity to the bioresorbable electrodes served as a control during acute recordings. Neural data was acquired by a FHC multi-channel neural amplifier (FHC Inc, Bowdoin, ME, USA) and an acquisition system (16 bit Axon Instruments Digidata 1322A, Axon Instruments, Foster City, CA). Recordings were high-pass filtered at 0.1 Hz. Neural recording data were analyzed offline using Clampfit software (Axon Instruments) and custom Matlab software for neural signal analysis.

In vivo chronic recordings

An adult Long-Evans rat was anesthetized with isoflurane and placed in a stereotactic frame (David Kopf Instruments Tujunga, CA). Body temperature was maintained with a heating blanket and the eyes were covered with ointment to prevent drying. The skull was exposed and a large craniotomy (4 mm x 8 mm) was made between bregma and lambda and laterally to the

midline. The electrode was placed on the exposed dura and a slurry of gel foam and saline was layered on top of the electrode. A screw electrode was placed contralaterally to the experimental array, with another such electrode placed posterior to lambda as a ground and reference. Additional screws were secured in the skull for anchoring. The skull and electrodes were then covered with dental cement and the connecting plug was secured on top. The rat was given meloxicam for postoperative pain and allowed to recover on a heating pad. The rat was given meloxicam daily for 3 days after surgery to minimize pain. After 1 week the animal was placed in a cage for video/EEG recording. EEG signals were collected continuously from 3 channels on the array and from the screw. The signals were amplified and low pass filtered at 600 Hz (Multichannel Systems, Reutlingen, Germany) and sampled at 2000 Hz with a 16 bit digitizer (National Instruments, Austin, TX). Data was acquired using a custom written MATLAB routine.

Chronic evaluation of immunohistochemistry

Rats (n=14) were anesthetized and transcardiac perfusion was performed using phosphate buffered saline (PBS 10x, cat. # BM-220, Boston BioProducts, Ashland, MA), followed by 4% paraformaldehyde (PFA, cat. # BM-155, Boston BioProducts). Whole brains were then removed and post-fixed overnight at 4℃ in the same 4% PFA solution. Subsequently, fixed brains were cryoprotected in 30% sucrose (cat. # 57-50-1, Sigma-Aldrich, Saint Louis, MO) at 4℃ and coronal sections were cut at 20 μm using a Leica CM3050 S cryostat (Leica Biosystems Inc.). Serial sections, spanning the entire craniotomy site, were mounted on charged slides and stored at -20℃ until use. For immunostaining, slides were first immersed in an antigen retrieval solution (0.1M citrate buffer, pH 6.0, cat# ab64214, Abcam, Cambridge, MA) and placed in a water bath at 95℃ for 10 min. After cooling, sections were rinsed in distilled water, incubated in a blocking

solution containing 0.1% Triton X-100 (cat. # 9002-93-1, Sigma-Aldrich) and 5% normal goat serum (cat. # GS-0500, Equitech-Bio Inc., Kerrville, TX) for one hour at room temperature (RT) and then incubated overnight at 4 ℃ with the following primary antibodies: anti-glial fibrillary acidic protein (GFAP, 1:1000, cat. # SMI-22R, Covance, Princeton, NJ), and anti-ionized calcium binding adapter molecule 1 (Iba-1, 1:1000, cat. # 019-19741, Wako Chemicals USA, Inc., Richmond, VA). After 3x20-minute washes in PBS, sections were incubated with the corresponding fluorescent secondary antibodies (Alexa Fluor 488 goat anti-mouse IgG2b, 1:1000, cat. # A-21141, and Alexa Fluor 568 goat anti-rabbit IgG, 1:1000, cat. # A-11011, Invitrogen by Life Technologies, Grand Island, NY). After the final washes (3x20 min in PBS), the slides were cover-slipped with an anti-fade medium containing the nuclear stain DAPI (Fluoromount-G+DAPI, cat. # 0100-20, Southern Biotechnology, Birmingham, AL). Control sections were incubated with omission of one or both primary antibodies, adding only the secondary antibodies to exclude false-positive labeling. Slides were examined on an epifluorescence microscope (Zeiss Axioscope, Germany) and images were acquired with a 20x objective and a Spot RT3 digital camera, using the Spot Software 5.1 (Diagnostic Instruments, Sterling Heights, MI). Digital images were processed using Adobe Photoshop 12.0 (Adobe Systems, San Jose, CA).

7.6 Figures

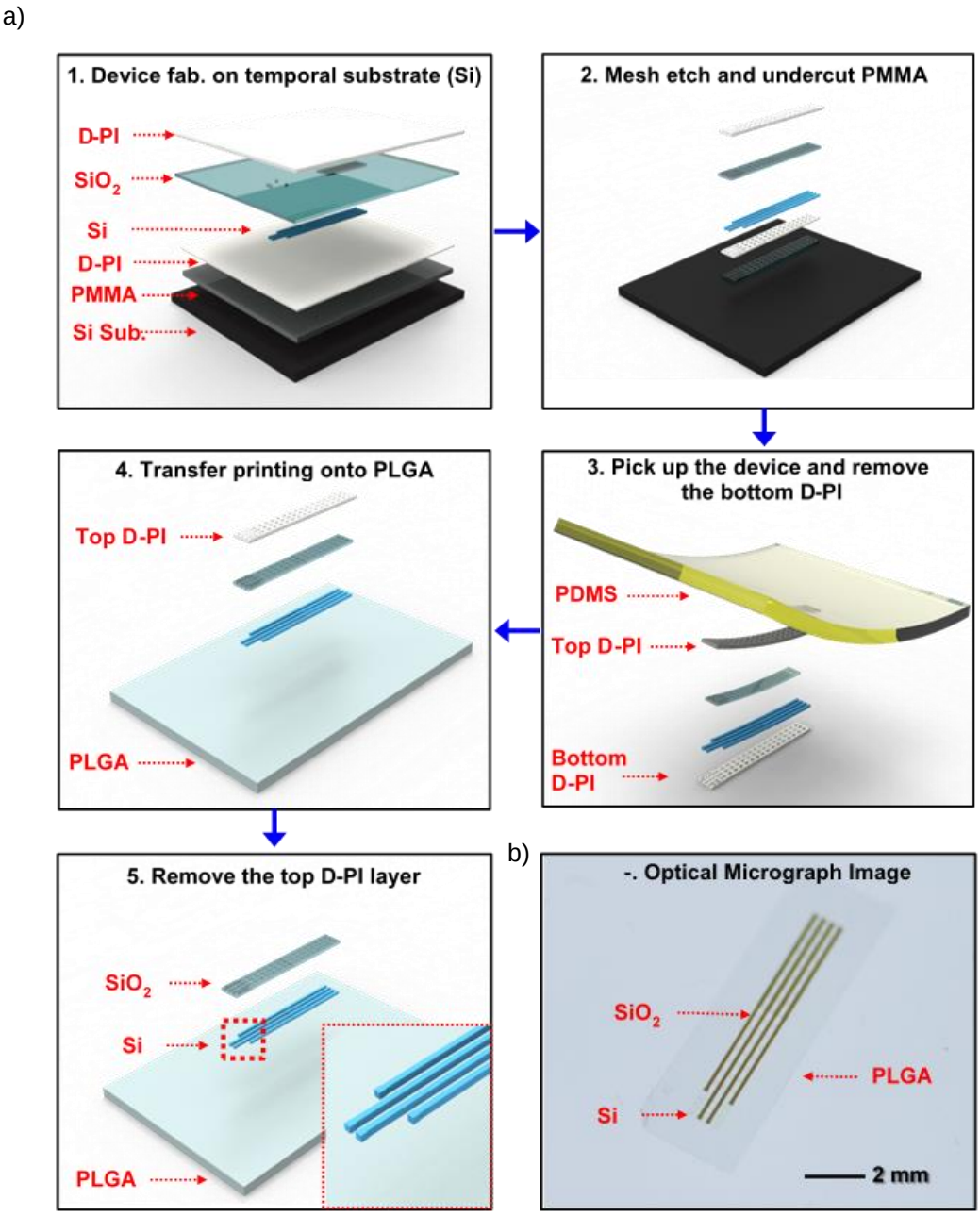

Figure 7.1 Materials and procedures for fabricating bioresorbable passive electrodes on biodegradable substrates (PLGA) and a device image. (a) Schematic illustrations of key processes for fabricating bioresorbable passive electrodes: (1) printing highly n-doped Si on temporary substrates, (2) defining mesh structure, followed etching materials using RIE and buffered oxide etchant (BOE), (3) retrieving the device onto a PDMS slab, (4) printing the device onto a bioresorbable substrate (PLGA), and (5) removing the top D-PI layer. (b) Optical image of a complete device.

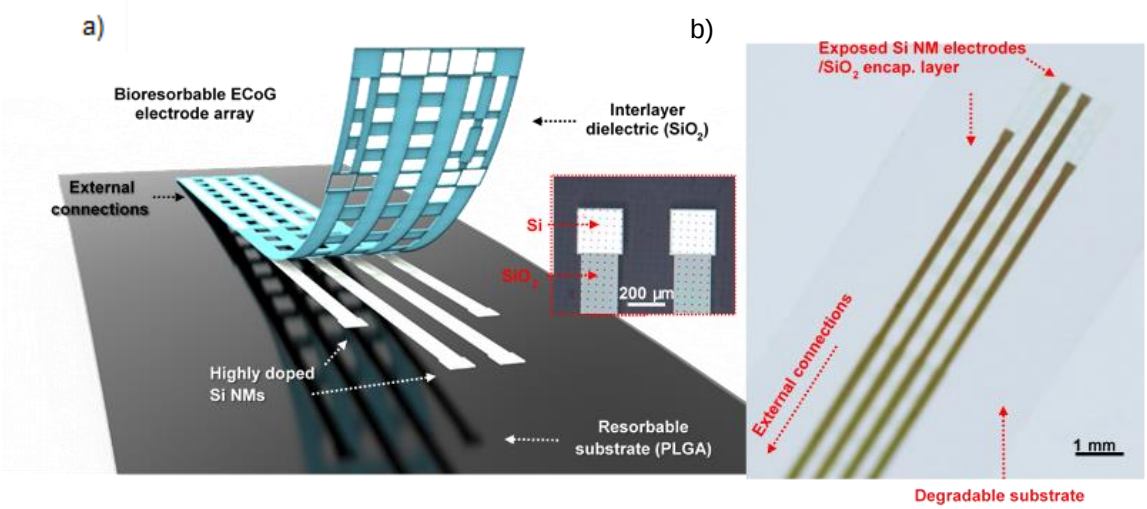

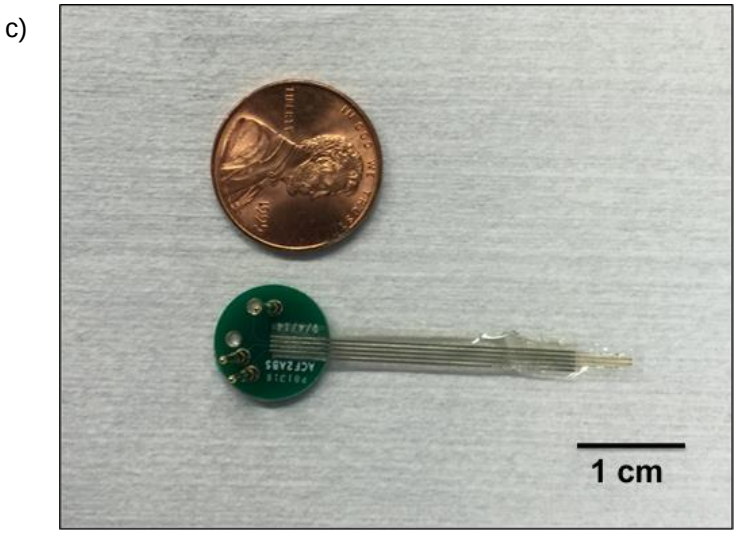

Figure 7.2 Thin, flexible neural electrode arrays with fully bioresorbable construction based on patterned Si nanomembranes as the conducting component. (a) Schematic exploded view illustration of the construction of a passive, bioresorbable neural electrode arrays for ECoG and sub-dermal EEG measurements. A photolithographically patterned, n-doped Si NM (~290 nm thick) defines the electrodes and interconnects. A film of SiO_2 (~100 nm thick) and a foil of PLGA (~30 μm thick) serve as bioresorbable encapsulating layer and substrate, respectively. The device connects to an external data acquisition (DAQ) system through an anisotropic conductive film interfaced to the Si NM interconnects at contact pads at the edge. (b) A magnified optical image of electrodes highlights the sensing (Si NM) and insulating (SiO_2) regions. (c) Size comparison of a bioresorbable passive electrode array to a penny.

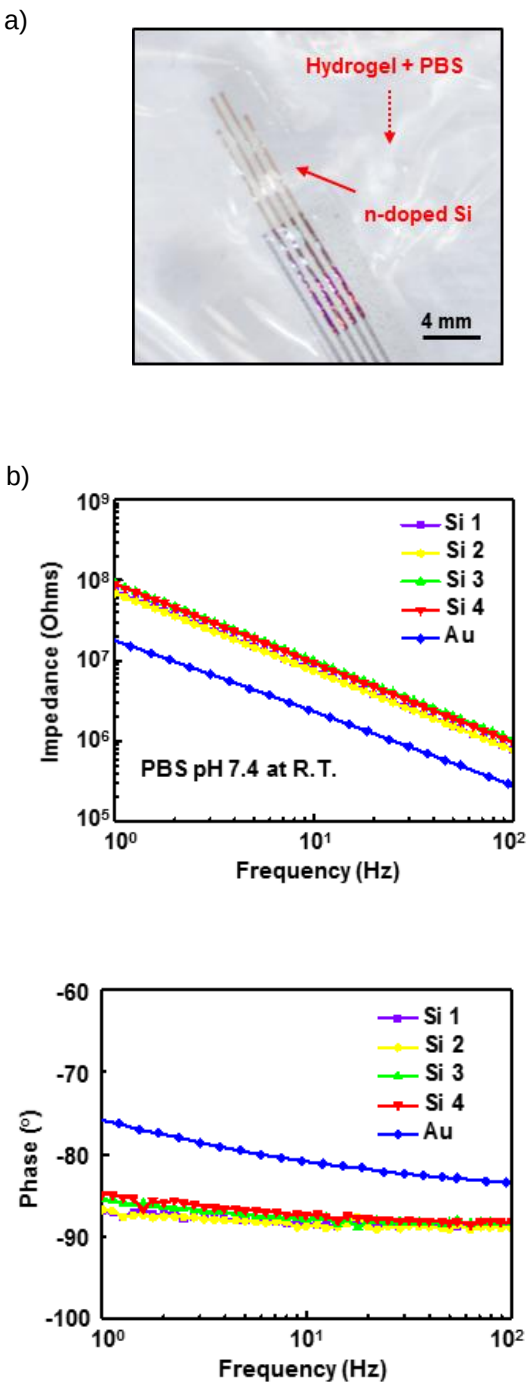

Figure 7.3 (a) Microscope image of a device on a hydrogel substrate immersed in an aqueous buffer solution (pH 7.4) at 37 ℃. (b) Impedance spectra measured at four different recording sites in an array configured for ECoG.

a)

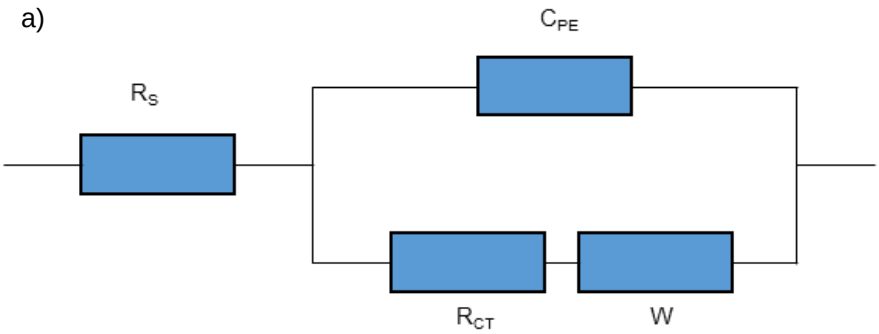

b)

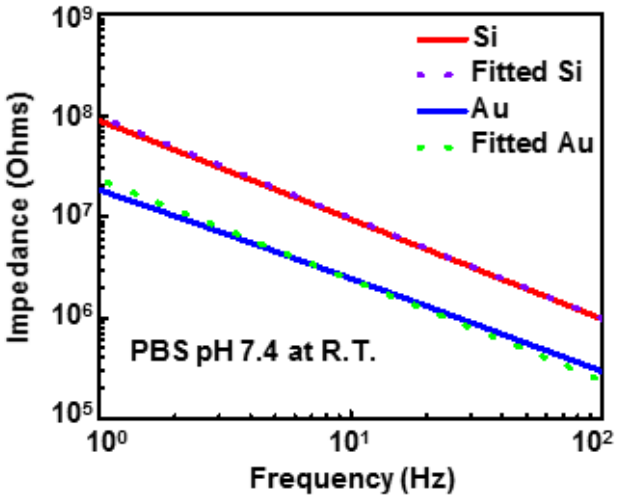

c)

	C_{PE}	R_{CT}
Si	2.5 μF/cm²	1.17 G-ohms
Au	10 μF/cm²	130 M-ohms

Figure 7.4 EIS characterization of Si and Au. (a) Schematic description of the equivalent circuit model used to fit EIS measurement results. CPE is the constant phase element representing the double-layer capacitance; RCT is the charge transfer resistance; and RS is the solution resistance. (b) Results of measurement (solid lines) and fitting (dashed lines) for the impedance. (c) Representative values of CPE and RCT for Au and Si.

a)

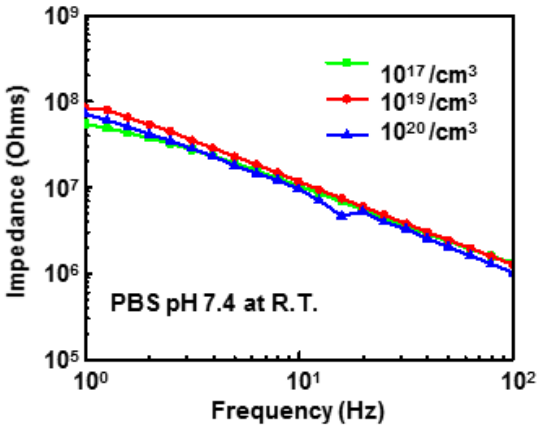

b)

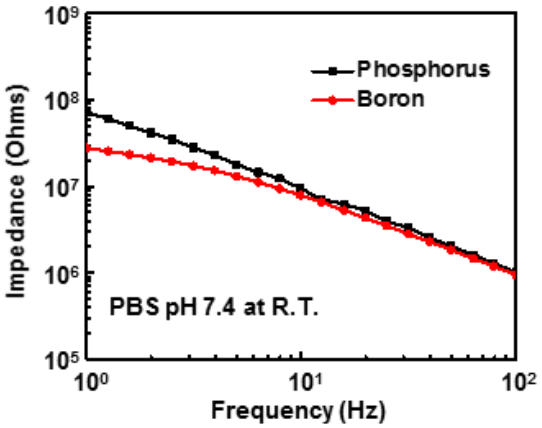

Figure 7.5 (a) Impedance spectra of phosphorus doped Si NM electrodes with different doping concentrations. (b) Impedance spectra of boron and phosphorus doped Si NM electrodes.

a)

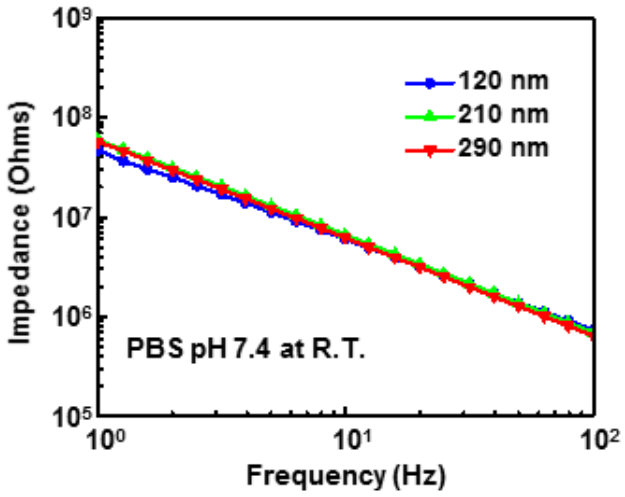

b)

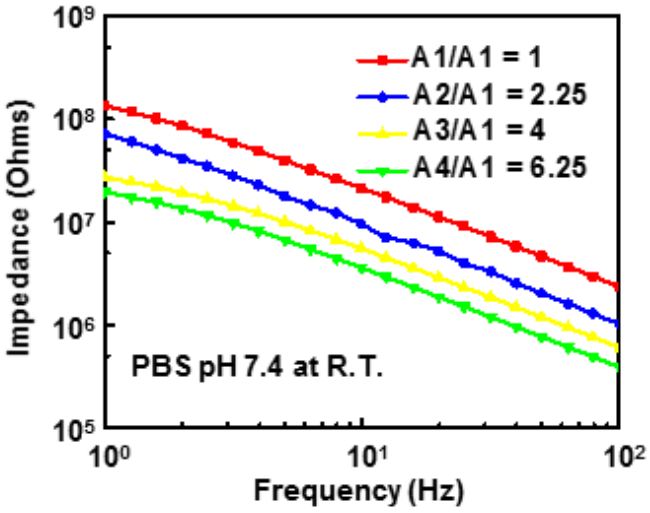

Figure 7.6 (a) Impedance spectra of different thicknesses of Si NM (120 nm, 210 nm, 290 nm). (b) Impedance spectra of phosphorus doped Si NM electrodes with different sites of areas.

a)

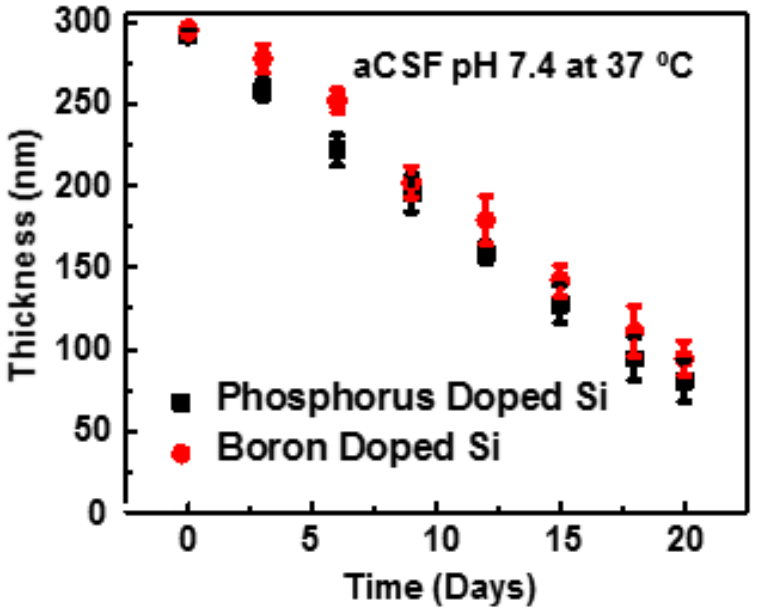

b)

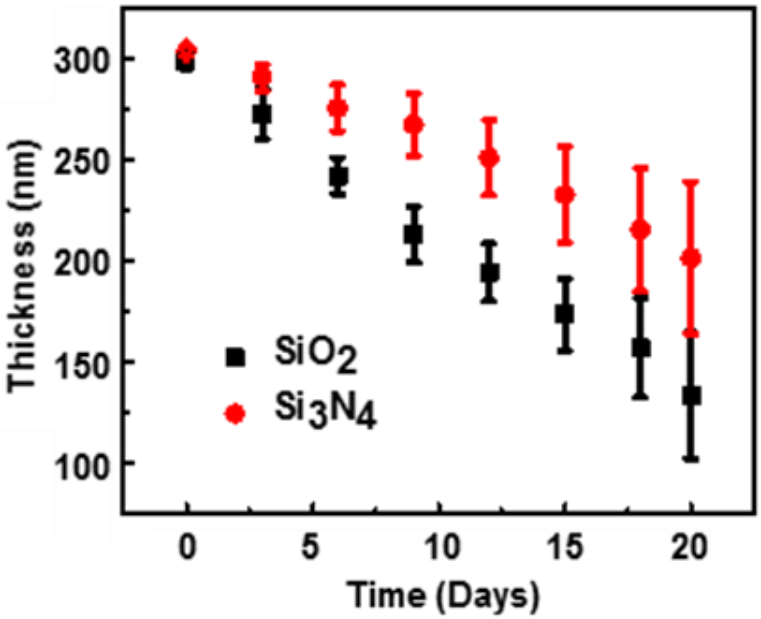

Figure 7.7 (a) Dissolution kinetics for phosphorus and boron-doped Si NMs (~290 µm thick, dopant concentration 1020) during immersion in artificial cerebrospinal fluid (aCSF) pH 7.4 at 37 ℃. (b) Hydrolysis kinetics of SiO_2 and Si_3N_4 used in the neural electrodes. Thickness as a function of time during dissolution in artificial cerebrospinal fluid (ACSF) at 37 ℃. The initial thicknesses were 300 nm for both SiO_2 and Si_3N_4.

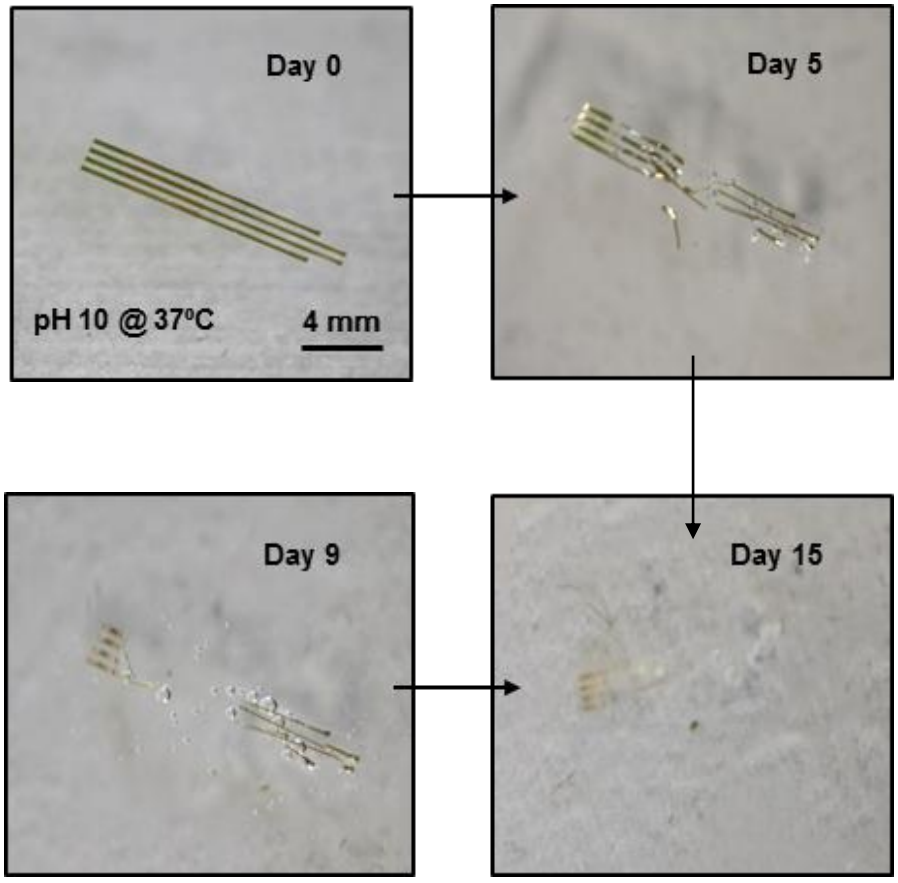

Figure 7.8 Images collected at several stages of accelerated dissolution induced by immersion in an aqueous buffer solution (pH 10) at 37 ℃.

a)

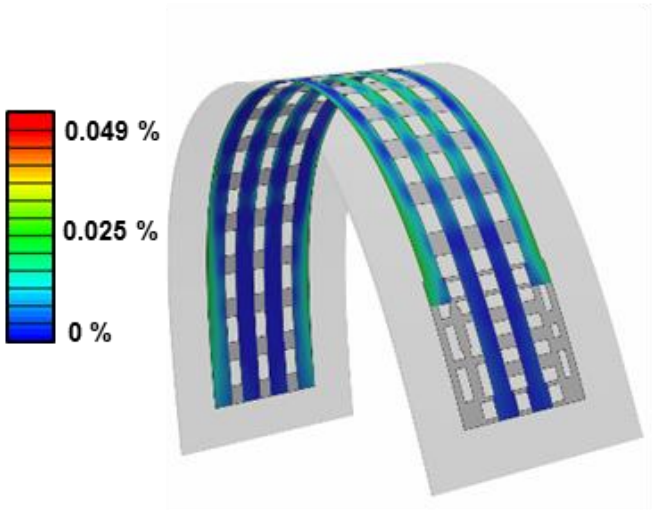

b)

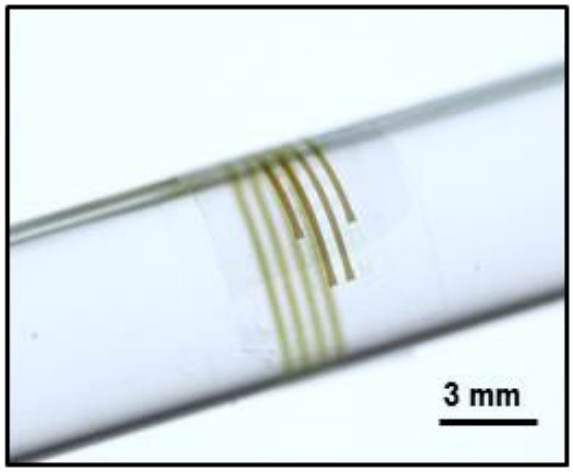

Figure 7.9 (a) Distribution of principal strains extracted from finite-element modeling (FEM) of a device bent to a radius of curvature of 1 mm and corresponding displacement profile and (b) image of an array wrapped around a cylindrical tube with a radius of 2 mm.

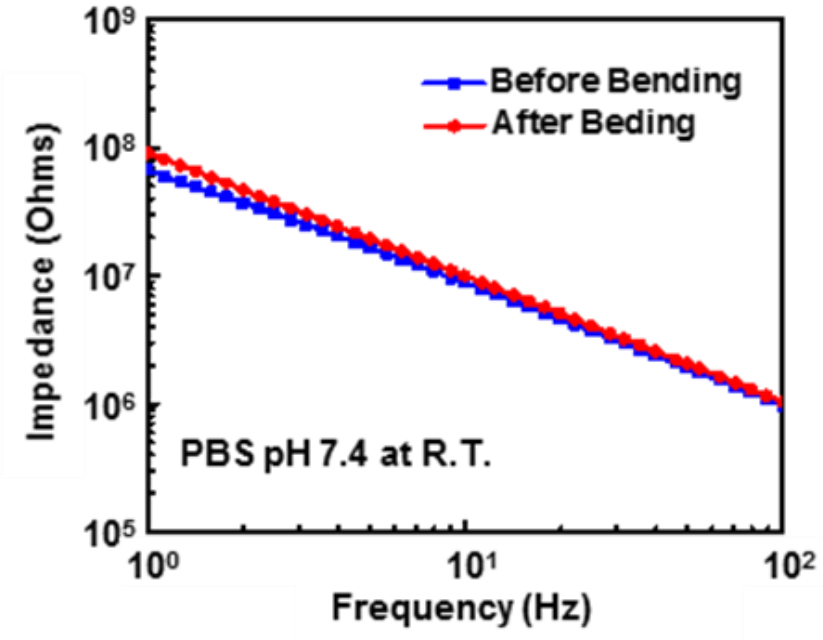

Figure 7.10 Impedance spectra before and after bending.

a)

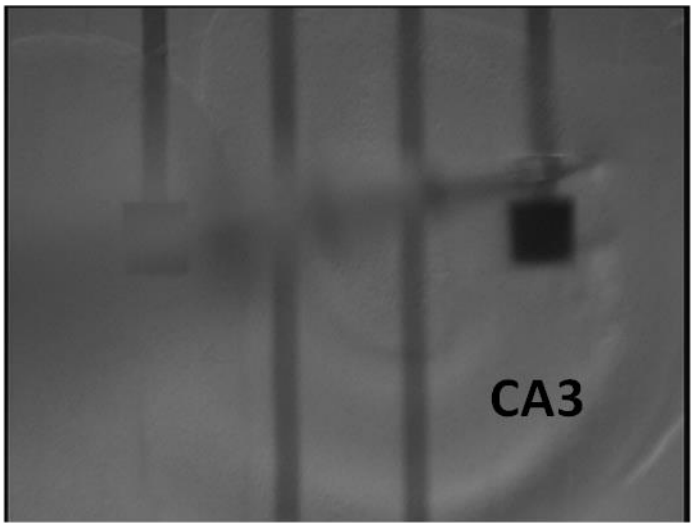

b)

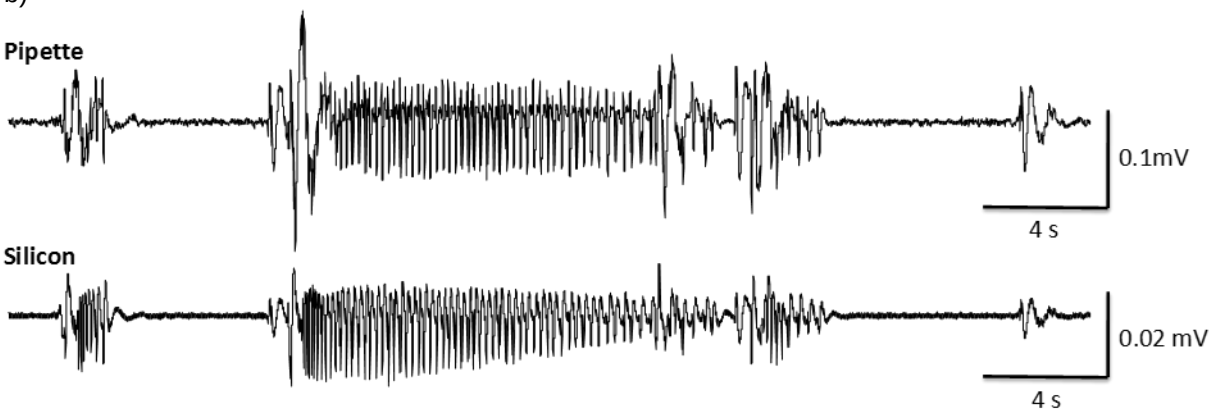

Figure 7.11 (a) Bioresorbable electrodes were placed onto a brain slice. (b) *In vitro* seizure recording, obtained using pipette electrodes (upper frame) and bioresorbable Si NM electrodes (lower frame).

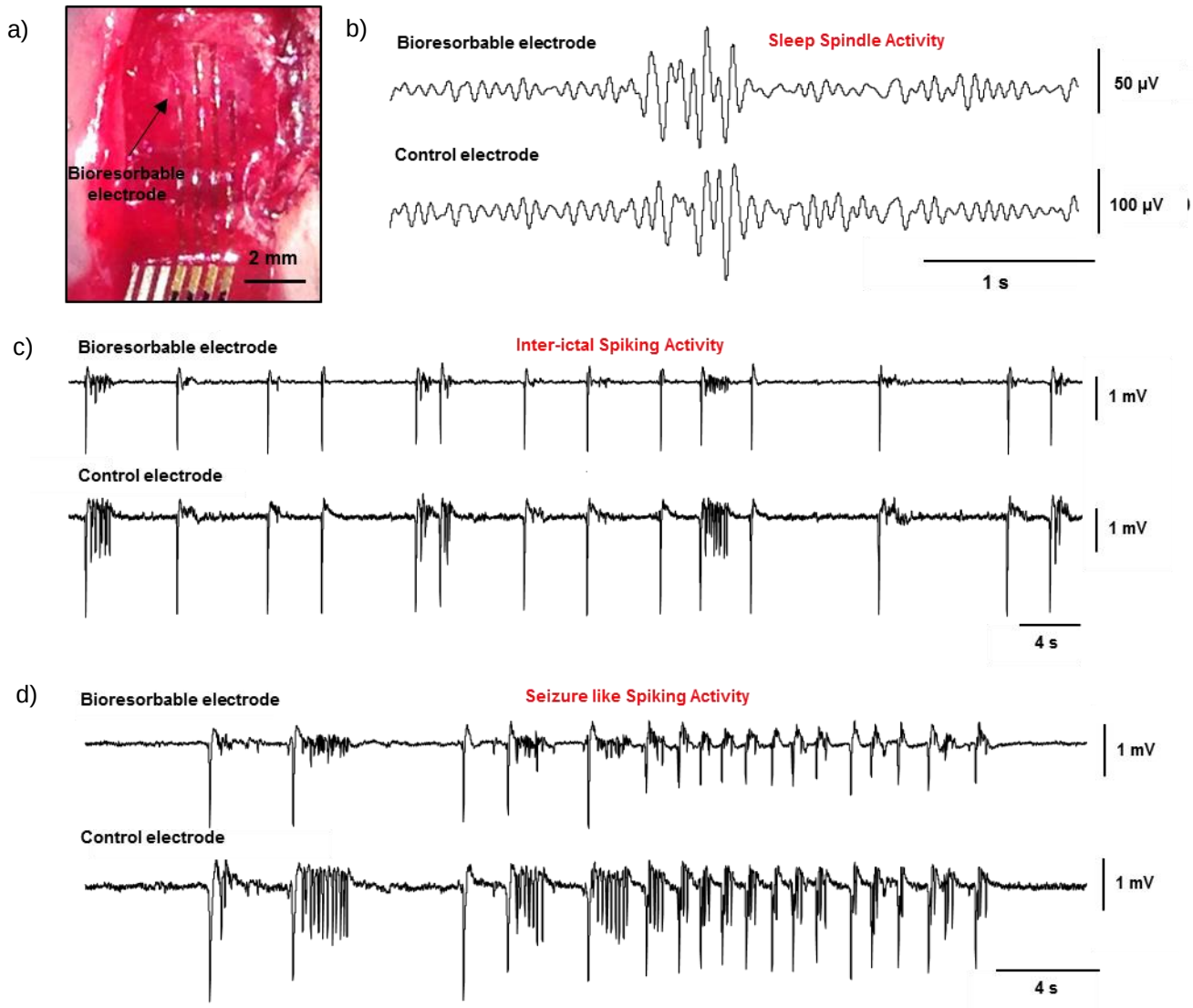

Figure 7.12 *In vivo* neural recordings in rats using a passive, bioresorbable electrode array. The data presented here are representative of three separate acute experiments, each with a duration of 5-6 hours. (a) Photograph of four-channel bioresorbable electrode array placed on the cortical surface of the left hemisphere of a rat. (b) Sleep spindles recorded by a bioresorbable electrode and a nearby commercial stainless steel microwire electrode, as a control, placed at 0.5 mm depth from the cortical surface. (c) Interictal spiking activity captured by the bioresorbable electrode and the control electrode after topical application of bicuculine methodide. Both electrodes interface with the same hemisphere. Data were processed through a 0.1 Hz-5 kHz bandpass filter. Recordings from the bioresorbable electrode and the control electrode show consistent interictal spikes. (d) Interictal spiking activity recorded by the bioresorbable electrode and the control electrode 30 minutes after topical application of bicuculine methodide. Both recordings exhibit high signal-to-noise ratio for detecting epileptiform activity.

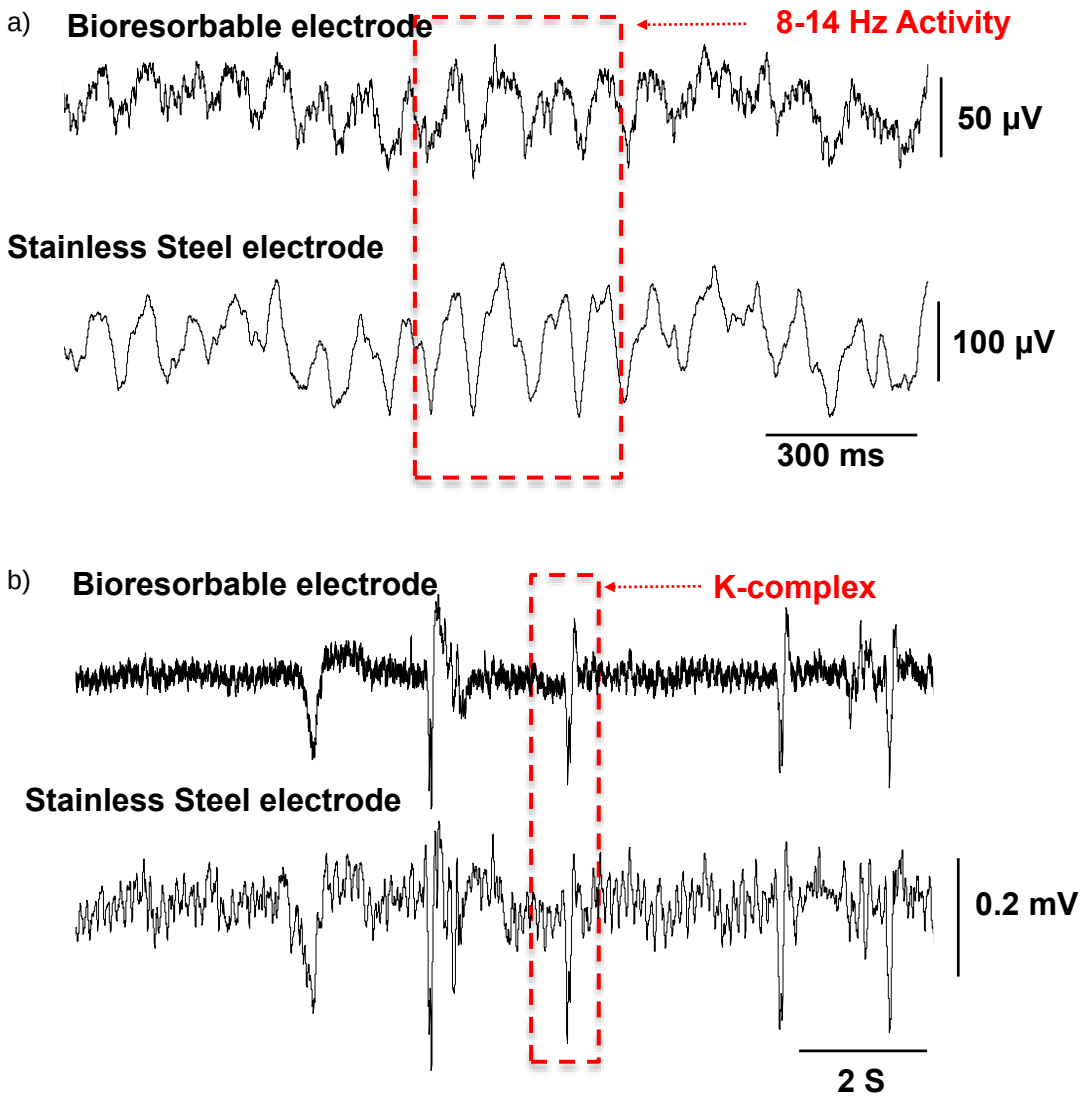

Figure 7.13 *In vivo* neural recordings in rats. (a) Slow wave activity. (b) K-complexes recorded using the bioresorbable electrode array and a control stainless steel microwire electrode.

a)

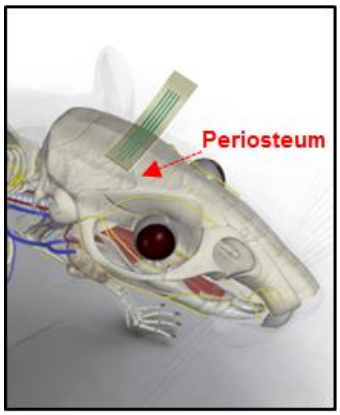

b)

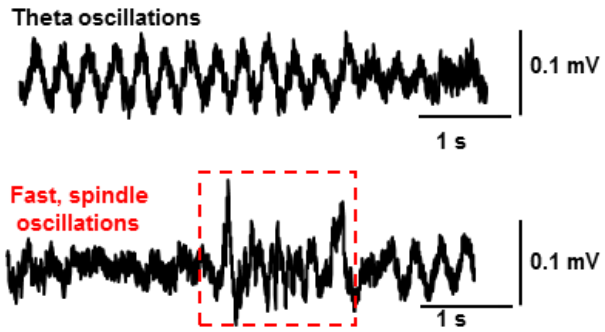

c)

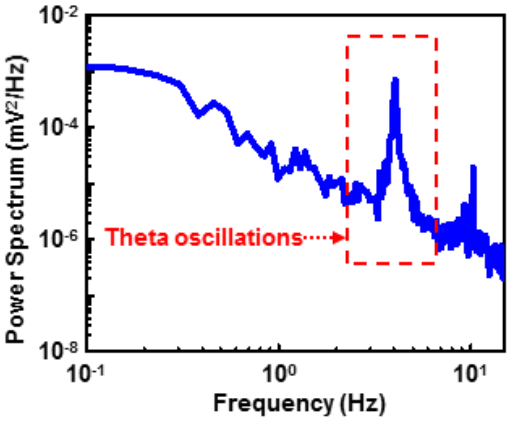

Figure 7.14 (a) Cartoon illustration of a bioresorbable array placed on the periosteum for subdermal EEG recordings. (b) Theta oscillations and fast spindle-like oscillations recorded subdermally using bioresorbable electrodes during isoflurane anesthesia. (c) Power density spectra of the theta oscillations recorded over a 5 min time window. The spectrum shows a clear peak at the expected frequency range.

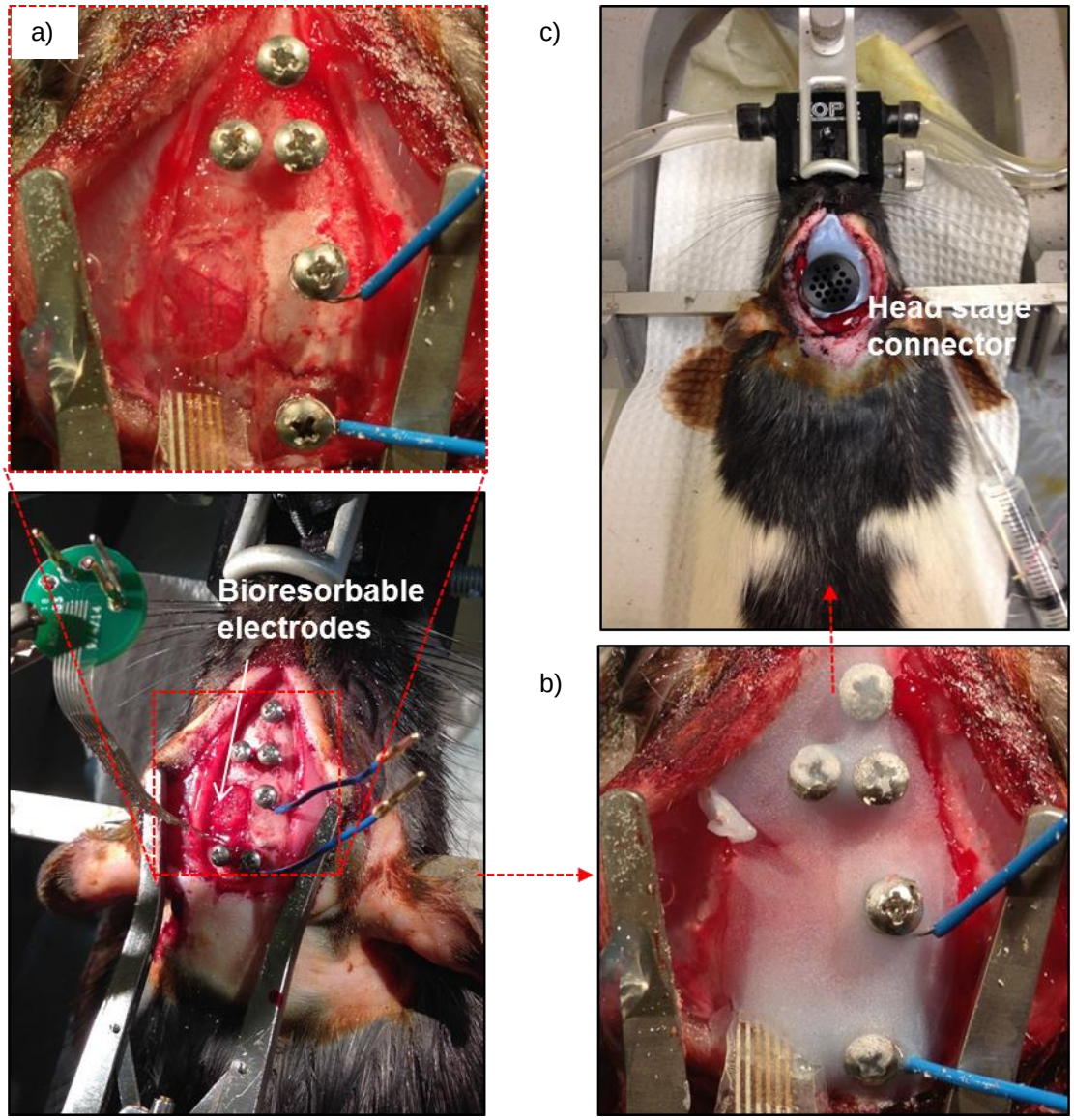

Figure 7.15 Photographs of surgery associated with chronic recording experiments. (a) Implanting the bioresorbable electrode arrays on a rat brain, (b) applying dental cement on the cortical surface and bioresorbable electrodes, and (c) connecting a head stage connector to the electrodes (right).

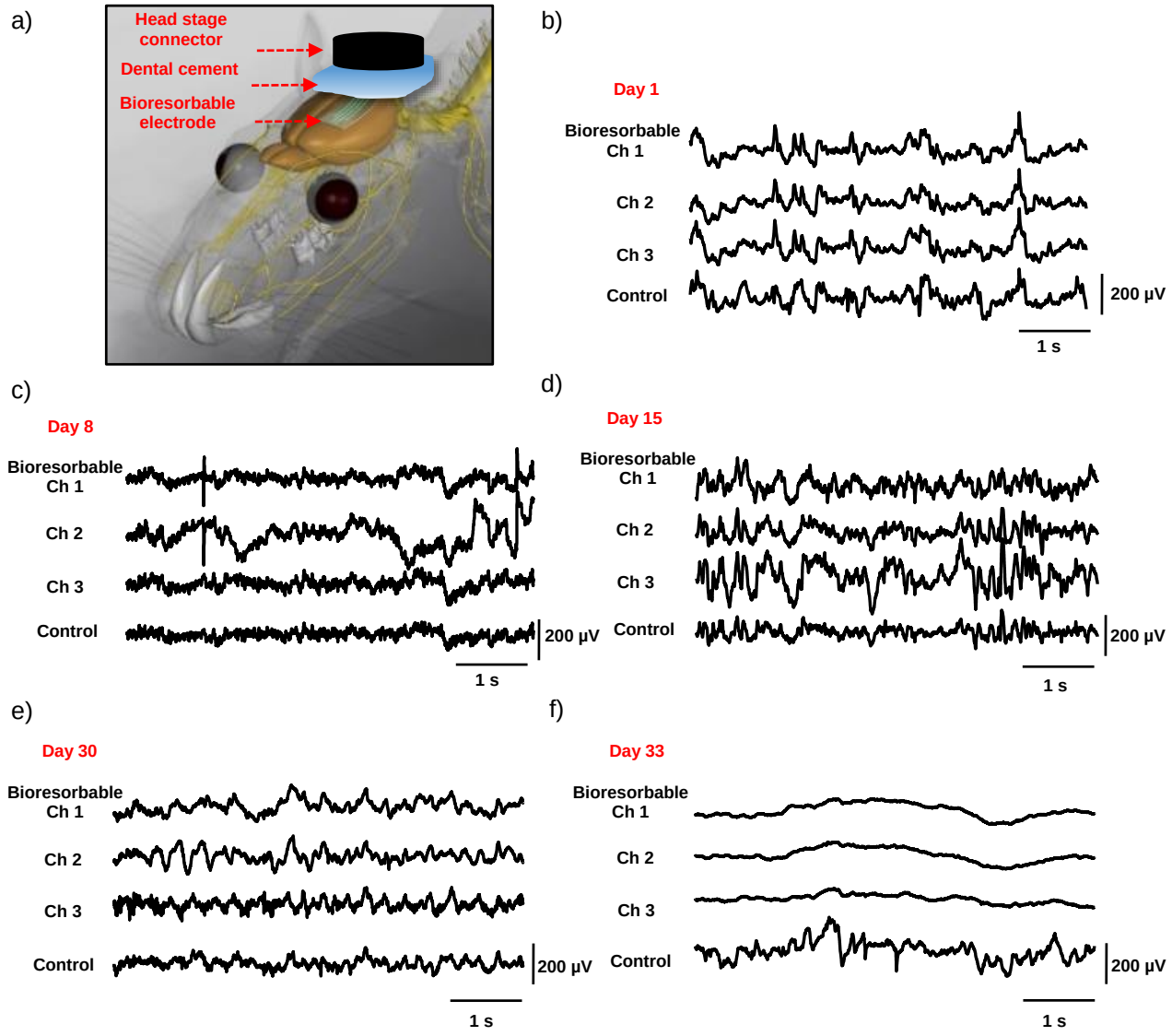

Figure 7.16 *In vivo* chronic recordings in rats using a passive, bioresorbable electrode array. The data presented here is representative of chronic recording experiments with a duration of 30 days. (a) Photograph of a four-channel bioresorbable electrode array implanted on the left hemisphere of the brain of a rat, for chronic recordings, with a gelfoam coating and a layer of dental cement. The array connects to a custom-built circular interface board through a flexible ACF cable. The inset shows the array and craniotomy after application of a first layer of dental cement. (b-f) Representative ECoG signals recorded by the bioresorbable array and the control electrode on days 1, 8, 15, 30 and 33. Recordings from three electrodes from the bioresorbable array exhibit large-scale oscillatory behavior consistent with small local and temporal variations. After functional dissolution (Day 33), signals from the bioresorbable array show no ECoG activity while the control electrode continues to show expected cortical potentials.

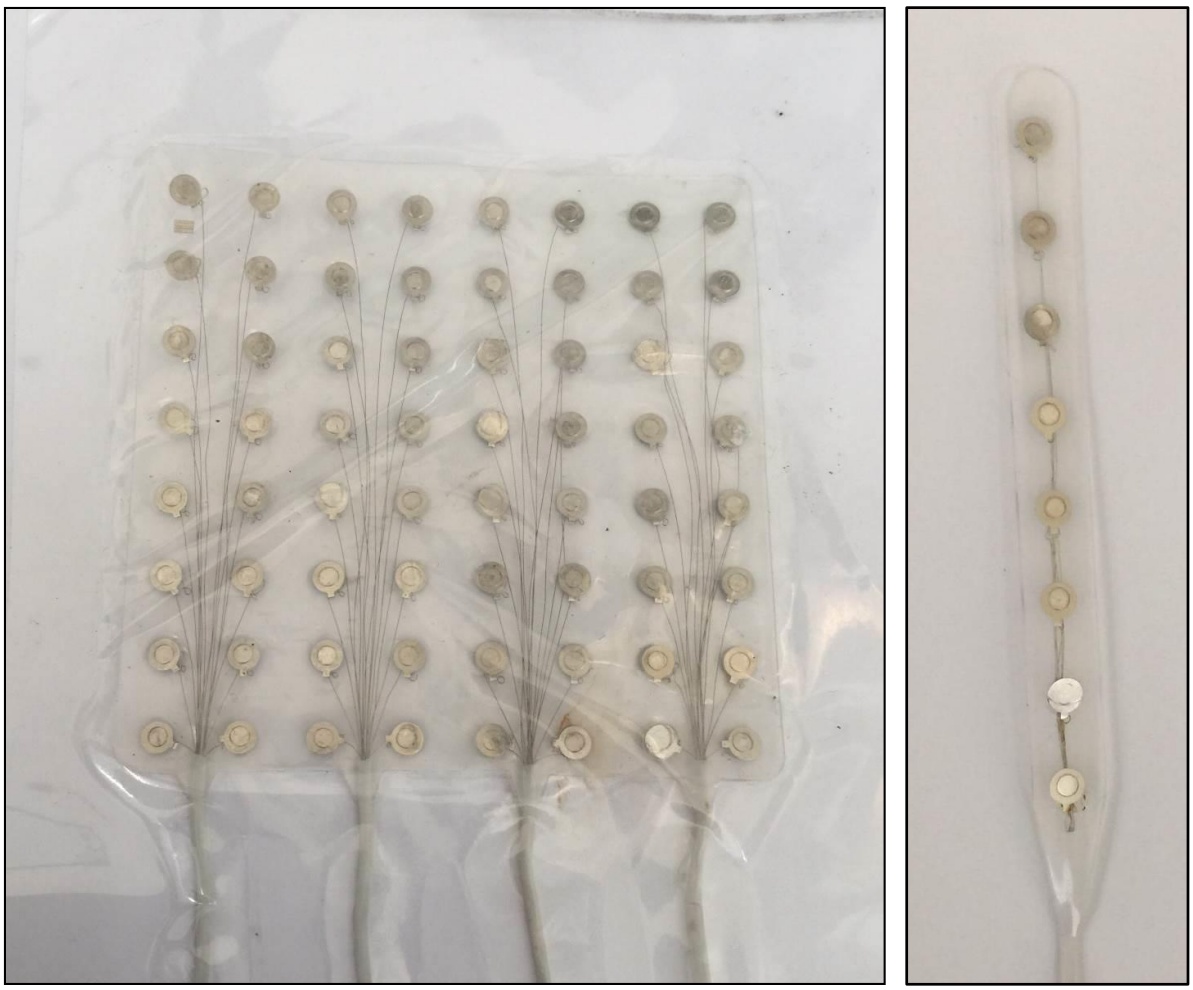

Figure 7.17 Photographs of Pt electrodes.

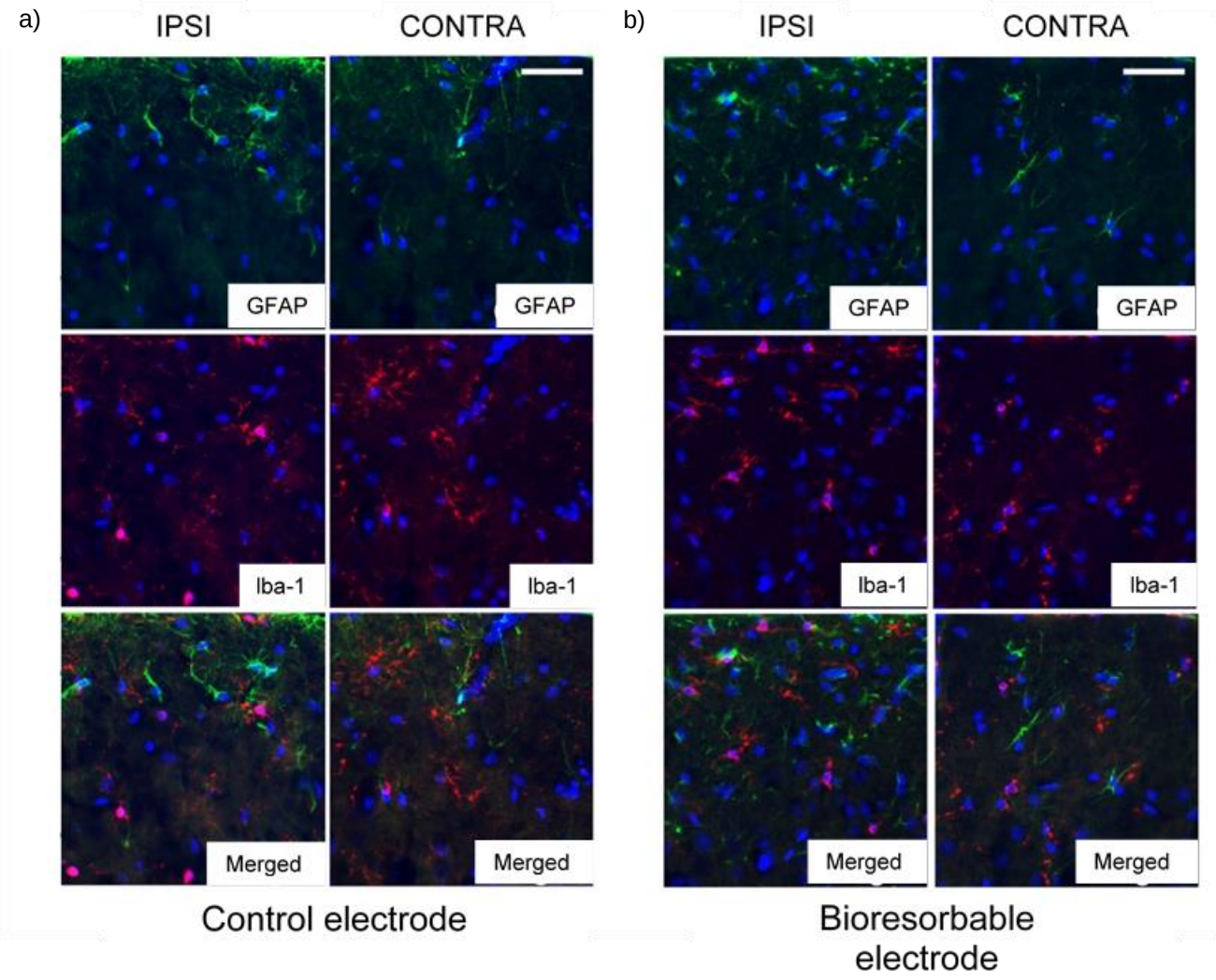

Figure 7.18 Immunohistology analysis. Double labeling for astrocytic marker GFAP (green) and microglia/macrophages marker Iba-1 (red) demonstrates moderate subpial gliosis at the implantation sites of both control (a, upper left panels) and bioresorbable (b, upper right panels) electrodes and a marked increase in the densities of activated round microglial cells, exclusively underneath the control electrodes (middle left panels). Cell nuclei are visualized with DAPI stain (blue). Scale bars represent 30 µm

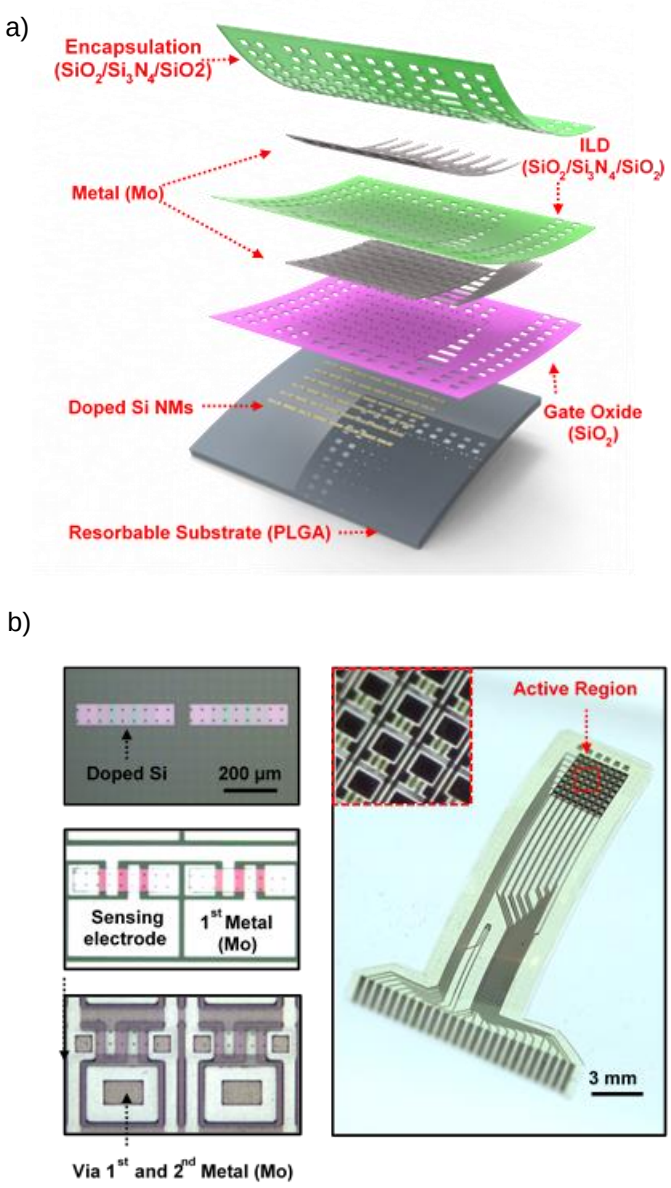

Figure 7.19 Bioresorbable actively multiplexed neural electrode array. (a) Schematic exploded view illustration of an actively multiplexed sensing system for high resolution ECoG, in a fully bioresorbable construction. This 8 × 8 embodiment includes 64 metal-oxide-semiconductor field-effect transistors (MOSFETs) where Si NMs serve as both the active semiconductor material and the neural interface electrodes. The metallization, the gate dielectric and the interlayer dielectric rely on thin films of Mo (~300 nm thick) and SiO_2 (~100 nm thick) and trilayers of SiO_2 (~300 nm thick) / Si_3N_4 (~400 nm thick) /SiO_2 (~300 nm thick), respectively. A second layer of Mo (~300 nm thick) defines column select lines. A similar trilayer serves as the encapsulation. A film of poly(lactide-co-glycolide) (PLGA, ~30 μm thick) forms the substrate. (b) Optical micrograph images of a pair of unit cells at various stages of fabrication (left) and a picture of a complete system (right).

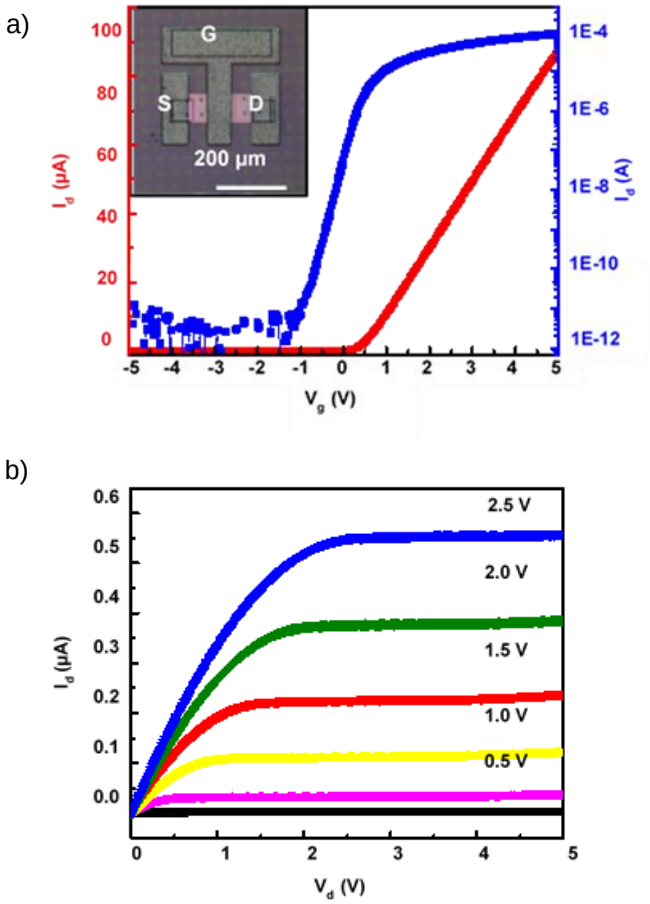

Figure 7.20 (a) Linear (red) and log scale (blue) transfer curves for a representative n-channel MOSFET, for V_g swept from −5 to +5 V. The channel length (Lch), and width (W) are 15 µm and 80 µm, respectively. The threshold voltage, mobility and on/off ratio are 1 V, 400 $cm^2/V \cdot s$ and ~10^8, respectively, with Mo for source, drain and gate electrodes, and SiO_2 for gate dielectrics. (b) Current-voltage characteristics, for V_g from 0 to 2.5 V with 0.5 V steps.

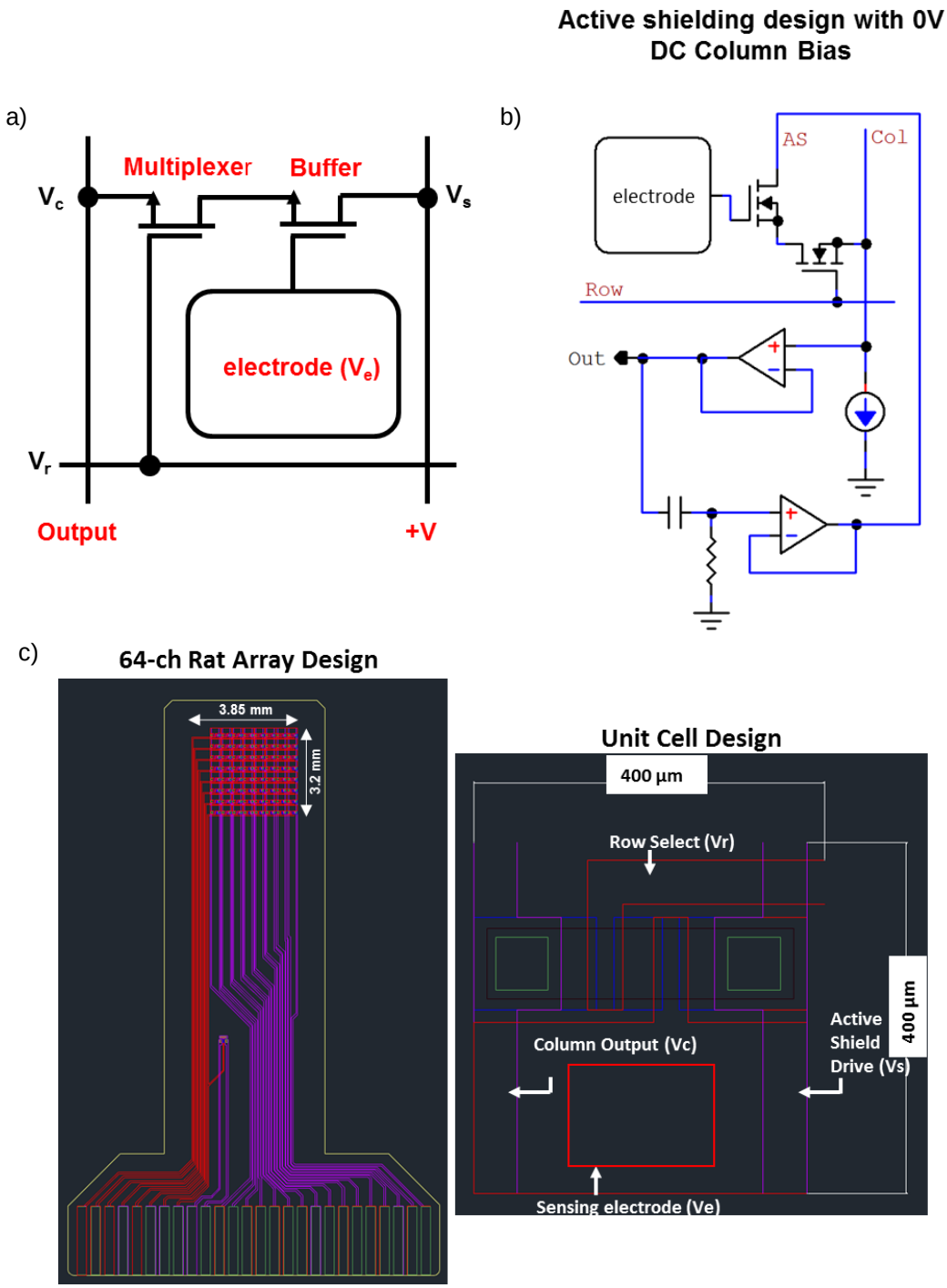

Figure 7.21 (a) Schematic circuit diagram of a single unit cell containing two matched n-MOS transistors in an actively multiplexed, bioresorbable electrode array. (b) Schematic circuit diagram of active shielding circuit for the actively multiplexed array. (c) 8×8 array of actively multiplexed channels in a bioresorbable electrode array and single unit sensor design with dimensions.

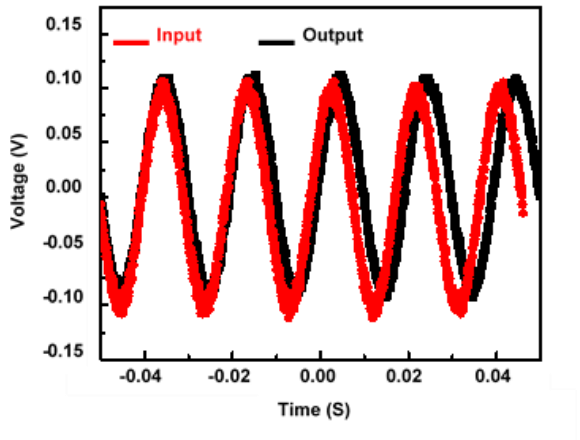

7.22 Output response of a unit cell with respect to an input sine wave (200 mV peak to peak) upon insertion in aqueous phosphate buffer solution (PBS, pH 7.4) at room temperature.

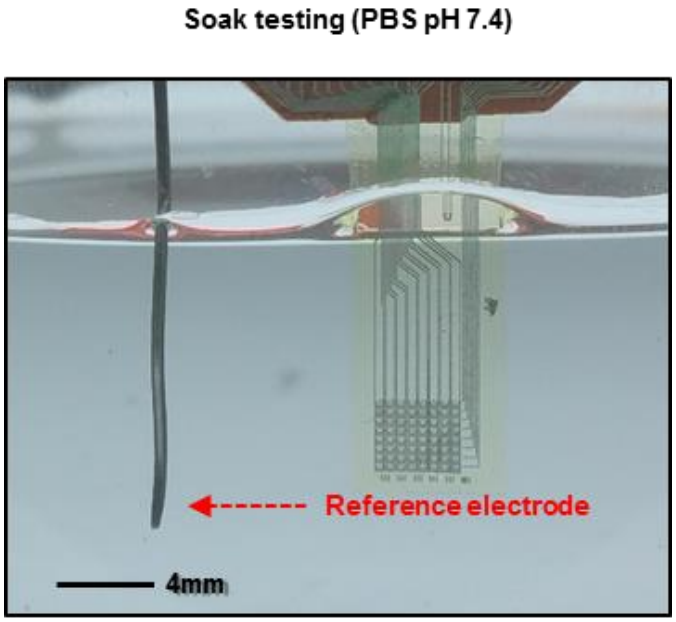

Figure 7.23 *In vitro* test setup for actively multiplexed array.

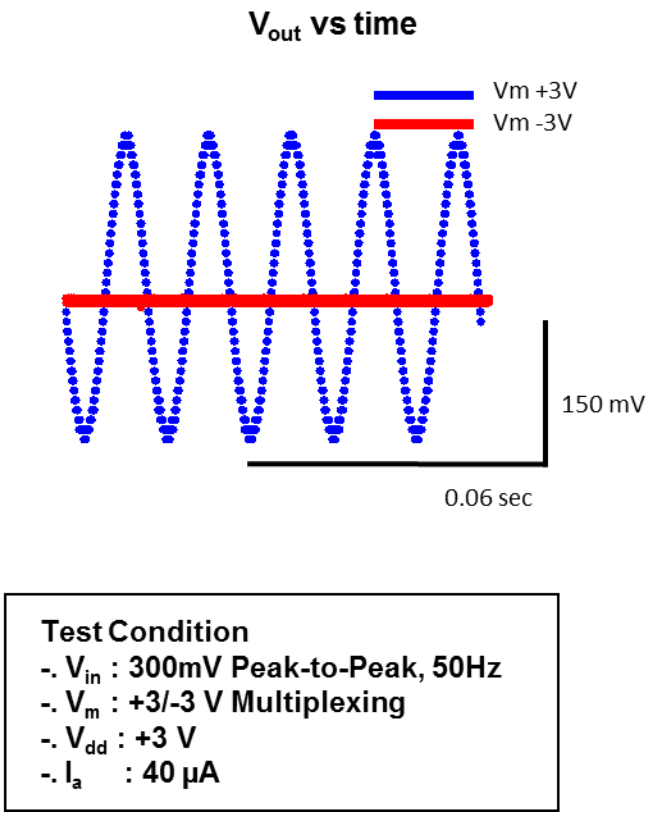

Figure 7.24 Switching property of a unit cell in an actively multiplexed, bioresorbable electrode array with respect to an input sine wave (200 mV peak to peak, 50 Hz) and biasing +/- 3V to V_r upon insertion in aqueous phosphate buffer solution (PBS, pH 7.4) at room temperature.

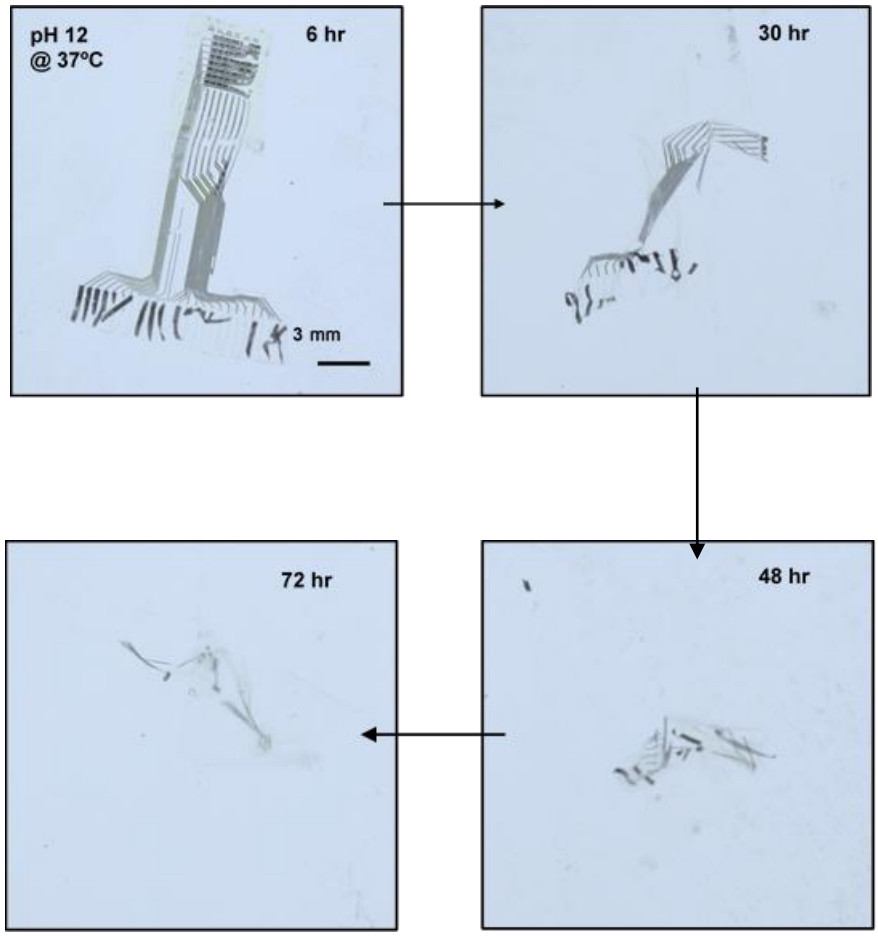

Figure 7.25 Images collected at several stages of accelerated dissolution of a system immersed into an aqueous buffer solution (pH 12) at 37 ℃.

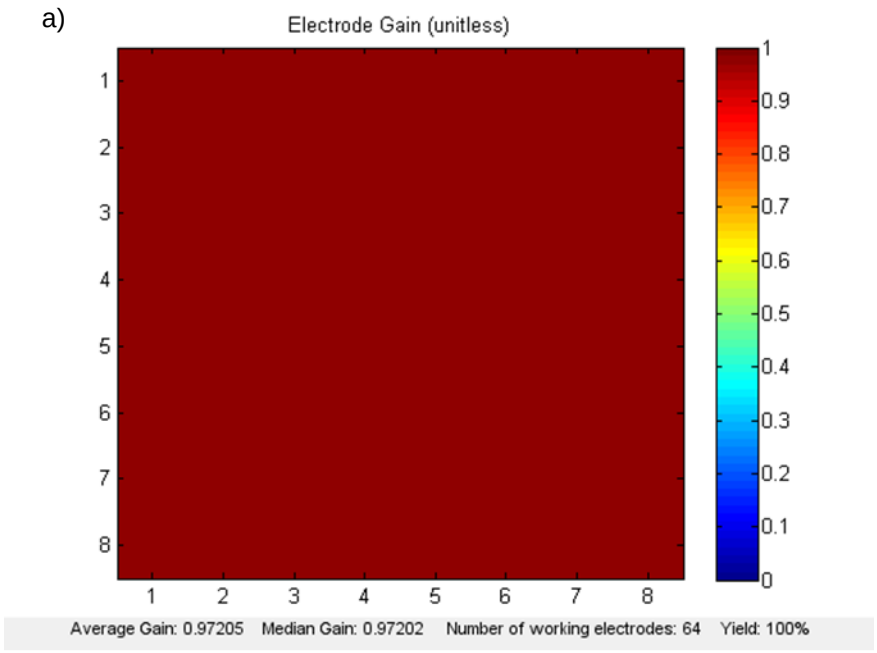

Figure 7.26 (a) Color map illustrating the spatial distribution of the electrode response, demonstrating the spatial uniformity of the gain of an actively multiplexed, bioresorbable electrode array. (b) Leakage current measurement.

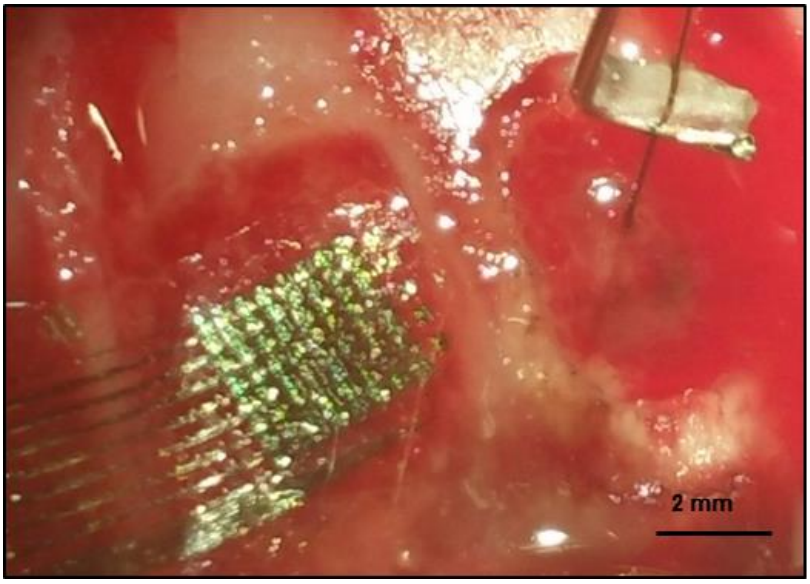

Figure 7.27 Photograph of active (left) and penetrating control (right) electrodes that were implanted onto left and right hemispheres of a rat brain, respectively.

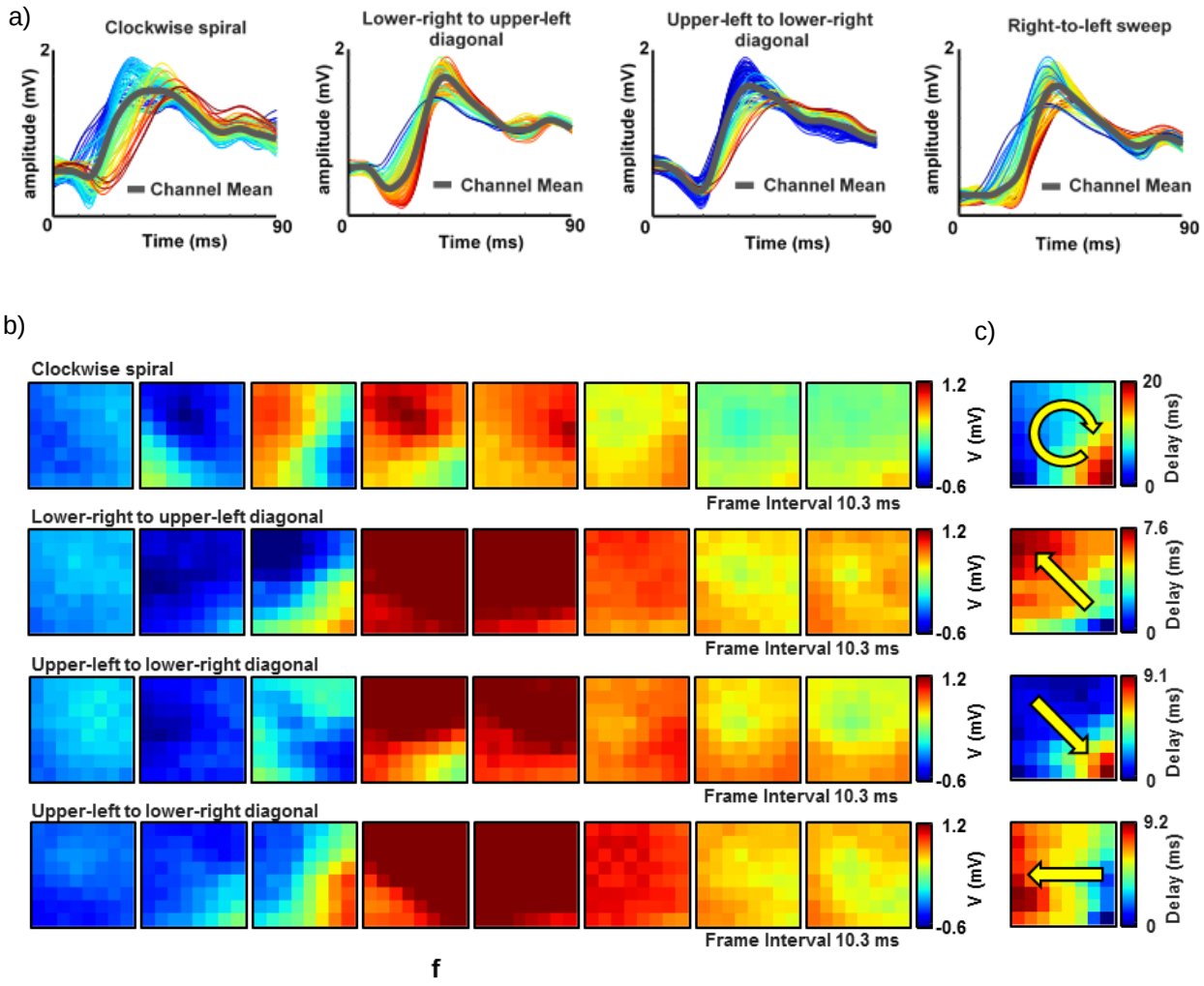

Figure 7.28 A 64-channel active device was implanted onto a rat brain and performed acute *in vivo* recording and whisker stimulation experiment. (a) Picrotoxin-induced spikes (clockwise spiral, lower-right to upper-left diagonal, upper-left to lower-right diagonal, and right-to-left sweep): 64 channel active array recording, and average channel response (grey) of all 64-channel electrodes. Channel waveforms are color-coded according to the relative latency of the spike maximum (blue is earliest, red is latest). (b) Movie frames corresponding to each spike pattern show varied spatio-temporal μECoG voltage patterns from all 64 electrodes during the labeled time. Blue indicates negative, and dark red indicates the highest peak-to peak voltage observed for that particular electrode site. The frame interval and color scale are provided for each set of eight movie frames. (c) Relative delay map for the band-pass filtered data of each spike activity from (b), indicating a clear phase singularity indicated by the arrow.

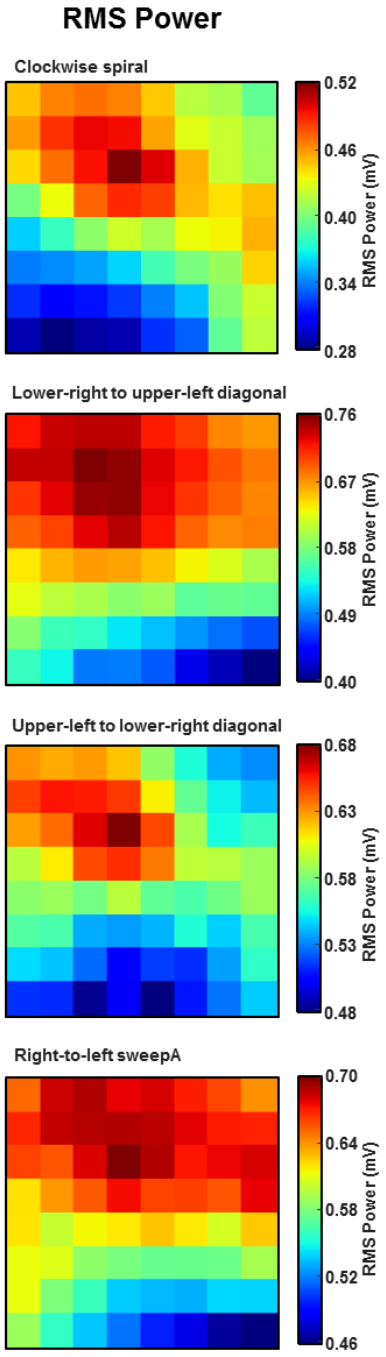

Figure 7.29 Representative RMS power image maps from four different spike clusters (clockwise spiral, lower-right to upper-left diagonal, upper-left to lower-right diagonal, right-to-left sweep) illustrate the high sensitivity of the electrode array and the spatially localized nature of spikes.

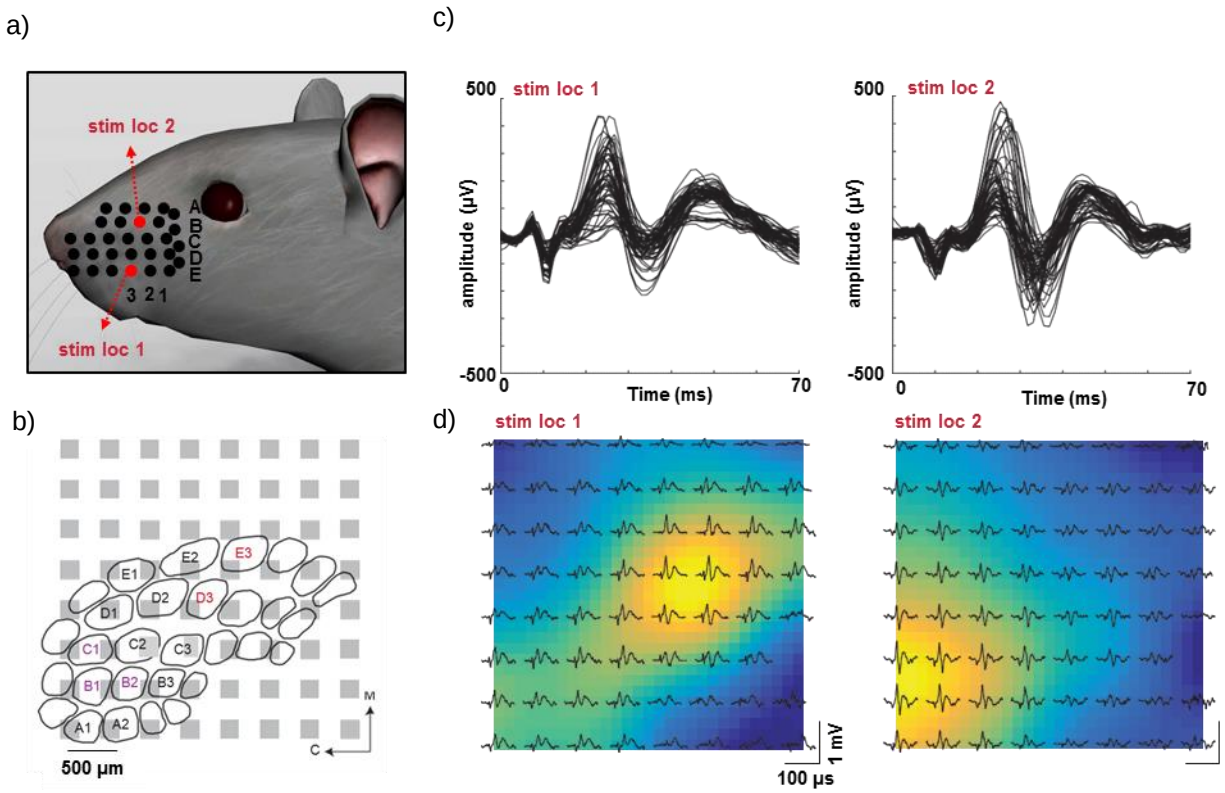

Figure 7.30 Whisker stimulation experiment. (a) Illustration of whisker pad and two stimulation locations in rat model. (b) Illustration of barrel cortex and hypothesized relative location of the recording array based on evoked potential results. Visibly-activated whiskers indicated by color corresponding to stimulation location. M = medial, C = caudal. C, Temporal characteristics of the potentials evoked by stimulation location 1 (left) and 2 (right). (c) Spatial distribution of the potentials evoked by stimulation location 1 (left) and 2 (right). (d) Color map indicates the evoked potential size, interpolated across the array.

7.7 References

[1] E. Niedermeyer and F.L. da Silva, *Electroencephalography: basic principles, clinical applications, and related fields* (Lippincott Williams & Wilkins, 2005).

[2] G.M. McKhann, J. Schoenfeld-McNeill, D.E. Born, M.M. Haglund, and G.A. Ojemann, Journal of neurosurgery **93**, 44-52 (2000).

[3] D. Whitmer, C. De Solages, B. Hill, H. Yu, J.M. Henderson, and H. Bronte-Stewart, Frontiers in human neuroscience **6**, 46 (2012)

[4] B. Litt *et al*., Neuron **30**, 51-64 (2001).

[5] M. Shapiro, T. Becske, D. Sahlein, J. Babb, and P.K. Nelson, American Journal of Neuroradiology **33**, 159-163 (2012).

[6] M. H. Wholey *et al*., Catheterization and Cardiovascular Interventions **50**, 160-167 (2000).

[7] R.T. Frizzel and W.S. Fisher III, Neurosurgery **37**, 1031-1040 (1995).

[8] J. Daube and D. Rubin, *Clinical Neurophysiology*. (Series Clinical Neurophysiology, 2009, Editor ed., City: Oxford University Press, New York, NY).

[9] X. G. Zhang, *Electrochemistry of Silicon and its Oxide*. (Kluwer Academic, New York, NY, 2001).

[10] R. C. Kelly *et al*., the Journal of Neuroscience **27**, 261–264 (2007).

[11] P. J. Rousche and R. A. Normann, the Journal of Neuroscience Methods **82**, 1–15 (1998).

[12] J. Du, T. J. Blanche, R. R. Harrison, H. A. Lester, S. C. Masmanidis, PLoS ONE **6**, e26204 (2011).

[13] D. R. Kipke, IEEE Transactions on Biomedical Engineering **51**, 896–904 (2004).

[14] M. Morita, T. Ohmi, E. Hasegawa, M. Kawakami, and M. Ohwada, Journal of Applied Physics **68**, 1272 (1990).

[15] H. Seidel, L. Csepregi, A. Heuberger, and H. Baumgartel, Journal of the Electrochemical Society **137**, 3612 (1990).

[16] P. Gentile, V. Chiono, I. Carmagnola, and P. V. Hatton, International Journal of Molecular Sciences **15**, 3640-3659 (2014).

[17] F.-Z. Shaw, Journal of Neurophysiology **91**, 63-77 (2004).

[18] P. S. Pearce *et al*., Epilepsy & Behavior **32**, 121-131 (2014).

[19] K. M. Rodgers, F. E. Dudek, and D. S. Barth, the Journal of Neuroscience **35**, 9194-9204 (2015).

[20] V. S. Polikov, P. A. Tresco, and W. M. Reichert, the Journal of Neuroscience Methods **148**, 1-18 (2005).

[21] S. I. Ryu and K.V. Shenoy, Neurosurgical Focus **27**, E5 (2009).

[22] R. Biran, D.C. Martin, and P.A. Tresco, Experimental neurology **195**, 115-126 (2005).

[23] R. Biran, D.C. Martin, and P.A. Tresco, Journal of Biomedical Materials Research Part A **82**, 169-178 (2007).

[24] S.-W. Hwang *et al*., Science **337**, 1640-1644 (2012).

[25] L. Yin *et al*., Advanced Functional Materials **24**, 645-658 (2014).

[26] S.-K. Kang *et al*., Advanced Functional Materials **7**, 9297-9305 (2015).

[27] S.-K. Kang *et al*., Advanced Functional Materials **24**, 4427-4434 (2014).

[28] S.-W. Hwang *et al*., ACS Nano **8**, 5843-5851 (2014).

[29] J. Viventi *et al*., Nature Neuroscience **14**, 1599-1605 (2011).

Chapter 8. HIGH DENSITY CAPACITIVE NEURAL INTERFACE USING ACTIVE CONFORMAL ELECTRONICS (HDC)

8.1 Introduction

High-resolution neural interfaces over a large area have previously been impossible owing to the infeasibility of connecting thousands of wires in the small intracranial space. Current systems have drawbacks associated with damage to tissue or gradual degradation of sensors and the structures are rigid [1-3] and cannot deform continuously as a brain swollen by insult changes shape. This may induce local damage that injures the patient and impedes signal collection. Direct contact of sensors to tissue without encapsulation offers improved signal-to-noise ratios but may promote biofouling, degradation of electrodes and other biocompatibility issues. We develop new devices that integrate flexible Si nano-membrane transistors and report high-density capacitive neural interfaces using active conformal electronics (HDC). Neural sensing from significant areas of the brain at high spatial and temporal resolution is demonstrated and tested. A high-density multiplexed array of 1,040 electrodes covering a moderate area maintains conformal contact even with moderate volumetric changes to the substrate. HDC's enabling technology will revolutionize understanding of motor circuits, decision making circuits, neuropsychiatric illness, and the complex interplay among them by enabling simultaneous recording and stimulation in large-area, distributed brain networks at high resolution. Previous neural interfaces [4-8] individually wire each passive sensor at the electrode-tissue interface, constraining density and area scaling. HDC combines capacitive detection schemes with conformal electronics and active multiplexing to provide biologically safe, spatially resolved, large-area devices that maintain excellent contact to

neural tissue and eliminate bundles of signal wires. We will demonstrate two applications in the near future: motor control and decision making using HDC.

8.2 Experimental

We have designed and fabricated several iterations of active, voltage sensing, capacitive electrode arrays using thermally grown SiO_2 as a dielectric layer of capacitor and encapsulation. The designs include active shielding to increase the recording gain and decrease noise as mentioned in the previous chapter (Figure 7.21 (b)). The latest design includes a simplified layout to improve yield, an increased electrode pad size to improve capacitive coupling and square unit cell design to provide equal resolution in the x and y axes (400 μm spacing). The active electrodes are built using a new inverse fabrication process that we have developed in Figure 8.1. In the previous fabrication process of the neural monitoring sensor, doped Si nanoribbons were transfer-printed from source Si-on-insulator (SOI) wafers after an undercut etch removed the middle SiO_2 layer. After transfer-printing onto a flexible polyimide substrate, subsequent metal layers were deposited on the flexible substrate, forming the circuit interconnections. But this process has several issues; for example, a relatively low temperature device processing causes poor device performance (i.e. threshold voltage shifting of transistors, high hysteresis of transistors, and uniformity of the site pixels), and building good encapsulation layers is impossible. In our new process, the complete circuit, including metal interconnection layers, is formed on the rigid SOI wafer, and high-temperature CMOS techniques in the industrial levels of fabrication can be used (Figure 8.1 step 1-4). A flexible base layer (kapton sheet (13 μm thick)) is attached on top of the metal interconnection layers (Figure 8.1 step 5) after forming transistors and interconnects in order to minimize the strain from the SiO_2 layer from the top. Finally, the device is flipped over and the bulk Si of the SOI wafer is etched away using deep reactive ion etching (RIE), leaving the SiO_2

and ultra-thin Si device layers behind (Figure 8.1 step 6). Two main steps, device layer fabrication and substrate preparation, are involved with the bonding process. First of all, devices can be fabricated on the SOI wafers as described in Figure 8.2. And then, the substrate layer can be prepared. Strain-free 25 µm or 13 µm thick Kapton film or liquid crystal polymer (LCP) is laminated onto the cured pdms on glass substrate. The spin-cast thin layer (5 µm) of PDMS is followed by SiO_2 layer deposition for bonding Kapton film or LCP and PDMS layer. We used bonding techniques to prevent device curling due to the large amount of strain, induced from exposed SiO_2 layer in Figure 8.3. Laminating the substrate layer onto the device layer and applying pressure and heat make strong O-Si-O bonding between the device layer and the substrate layer, which completes the device fabrication. The schematic cross section in Figure 8.4 (a) shows the complete device structure. Basically, the top 1 µm thick SiO_2 layer prevents bio-fluids penetration and protects the active device layer (i.e., transistors and metal interconnects). The backside is also well protected by Kapton, SiO_2, and PDMS layers. The combination of these encapsulation materials choices enables the long-term brain recording. The completed device shows high density electrodes arrays and flexibility (Figure 8.4. (b)).

We have designed a new hardware system that enables multiplexer control signals and output lines all to be voltage balanced to reduce the driving force for encapsulation breakdown. This suggest a greatly improved encapsulation lifetime. The design of the circuit became much simpler, which required a single multiplexing transistor for each electrode, further reducing the complexity of the design and potentially enabling higher density interfaces.

8.3 Results and Discussion

We have tested the devices in several ways. Testing consists of various electrical, mechanical and chemical tests *in vitro* designed to predict the ability of the system to function and withstand the solution environment. Figure 8.5 (a) is a photograph of a representative unit sensor of the electrode array. Figure 8.5 (b) summarizes the electrical properties of a representative n-type MOSFET, where the mobility and on/off ratio are ~380 cm^2 V^{-1} and ~10^7, respectively, as calculated from the slopes of the transfer curves and the ratio of maximum and minimum current outputs using standard field-effect transistor models. Different numbers of electrode arrays were fabricated. Mechanical testing was followed by device fabrication. Figure 8.6 summarizes the mechanical testing result for the device. Testing of active electrode arrays was done to ensure that they can accept repeated cyclical strains in ranges that would be expected during a traumatic brain injury (TBI) when the brain's volume and surface area are expected to deform significantly. Strain, twisting and deformation in multiple dimensions, uniaxially, biaxially or radially, were performed on the device. Figure 8.6 (a) is a photograph of a representative device, wrapped around the cylindrical rod. Mechanical testing was conducted using custom-built, automated mechanical bending apparatus (Figure 8.6 (b)). The transistor current-voltage curve only varied by a small amount while bent (Figure 8.6 (c)). Device performance was reliable and consistent after 5,000 bend cycles (Figure 8.6 (d)). Furthermore, the electrode arrays continued to function after being folded at a radius as sharp as 0.2 mm (Figure 8.6 (e)) and showed corresponding transistor current-voltage curve before and after folding (Figure 8.6 (f)).

The accelerated aging test is a good method to see the reaction rate with respect to the temperature in the solution environment. The test is closely related to the Arrhenius equation, which can be expressed as:

$$L\,(T) = Ae^{-\frac{E_a}{kT}}$$

where *L(T)* is the rate constant, *A* is the pre-exponential factor, E_a is the activation energy, *k* is the Boltzmann constant, and *T* is the absolute temperature (in kelvins). Based on this equation, the life time of the material can be calculated at certain temperature. Normal physiological temperature for animal is 37 ℃. By doing the accelerated aging test at high temperature (~90 ℃), we can predict how fast the materials degrade. The lifetime of encapsulating materials can be easily tested by coating Mg traces with encapsulation materials. Mg quickly dissolves in the phosphate buffered saline (PBS) at pH 7.4. Mg traces, coated with encapsulating materials, were soaked in the PBS pH 7.4 solution. We have rapidly screened 15 encapsulation designs to identify the strategy that survived for the longest duration in soak tests in PBS at 37 ℃ (Figure 8.7). A deposited Mg film provided visual indication of water ingress. Exposure to water causes the Mg to dissolve, indicating failure of the encapsulation. The Mg trace with SiO_2 encapsulation showed the longest life time without dissolution of Mg among the various encapsulation. The accelerated testing of Mg with SiO_2 encapsulation was performed as shown in the cross section (Figure 8.8 (a)). PDMS well is formed on the surface of the device to hold saline (Figure 8.8 (b)). The entire structure is heated to rapidly age the encapsulation and search for signals of failure (Figure 8.8 (c)). 300 nm thick SiO_2 encapsulation survived under accelerated aging soak tesing for 6 days at 90 ℃ in Figure 8.8, which is equivalent to ~9 months at body temperature (37 ℃). To test the durability of our encapsulation after bending, 5 hours of accelerated aging soak testing at 90 ℃, which was equivalent to 10 days at 37 ℃ based on the calculation using the Arrhenius equation, was performed (Figure 8.9 (a)), followed by 1000 cycles of bend testing (Figure 8.9 (b)). After bend testing, the devices were returned for an additional soak test (Figure 8.9 (c)). We verified that the encapsulation remained functional after soak testing and bend testing in Figure 8.9.

Figure 8.10 shows the dissolution kinetics of SiO_2 depend upon the temperature. At higher temperature, SiO_2 dissolves quickly based on the plot in Figure 8.10 (a), corresponding to the trend of Arrhenius equation. Figure 8.10 (b) shows the experimental results of the dissolution of SiO_2 with calculated results from Arrhenius equation. The experimental data and the overall calculation results exhibit good agreement.

We have investigated the mechanics of laminating the large-scale electrode array to the soft brain surface in Figure 8.11. Additional deformability may be required to enable full lamination of the active array to the brain surface. This deformability can be obtained by leaving small gaps between sub-arrays when molding the electrodes into the artificial dura. The stretchability of the artificial dura will allow each sub-array to have optimal conformal contact. For the current device structures, 1,040-channel electrodes will be molded together in the artificial dura (AD) to build the small-area and large-area electrode arrays depending upon the size of each electrode. For the artificial dura, the new chamber system in Figure 8.12 is designed for the device. The array was tested *in vitro* at the end (Figure 8.13). A optical micrograph image of the array shows in Figure 8.13 (a). The average gain and yield were 87% and 94%, respectively (Figure 8.14 (b)). Finally, the active arrays will be chronically implanted in non-human primates (NHP) in a near future.

8.4 Conclusion

As mentioned in the introduction, current systems have drawbacks associated with damage to tissue or gradual degradation of the sensors. The areal packing density and cell and neuron densities vary across the cortical sheet in a predictable manner across different primate species.

The primary motor cortex is characterized by lower neuron densities relative to other cortical areas but in non-human primate ranges 50,000-70,000 neurons/mm^2. In clinical devices of the current art, the packing density of sensors is so low that the ratio of sensors to neurons may be in the range of 10 million. In this system, the ratio might be close to 2500:1, unprecedented in large-area systems. We have developed nano-membrane logic-enabled multiplexing of dense arrays of amplified and multiplexed sensors occupying less volume. We will record spatial properties of feline brain activity *in vivo*, including sleep spindles, single-trial visually evoked responses and electrographic seizures in the near future. Such advances will enable new diagnostic and therapeutic brain-machine interfaces.

8.5 Figures

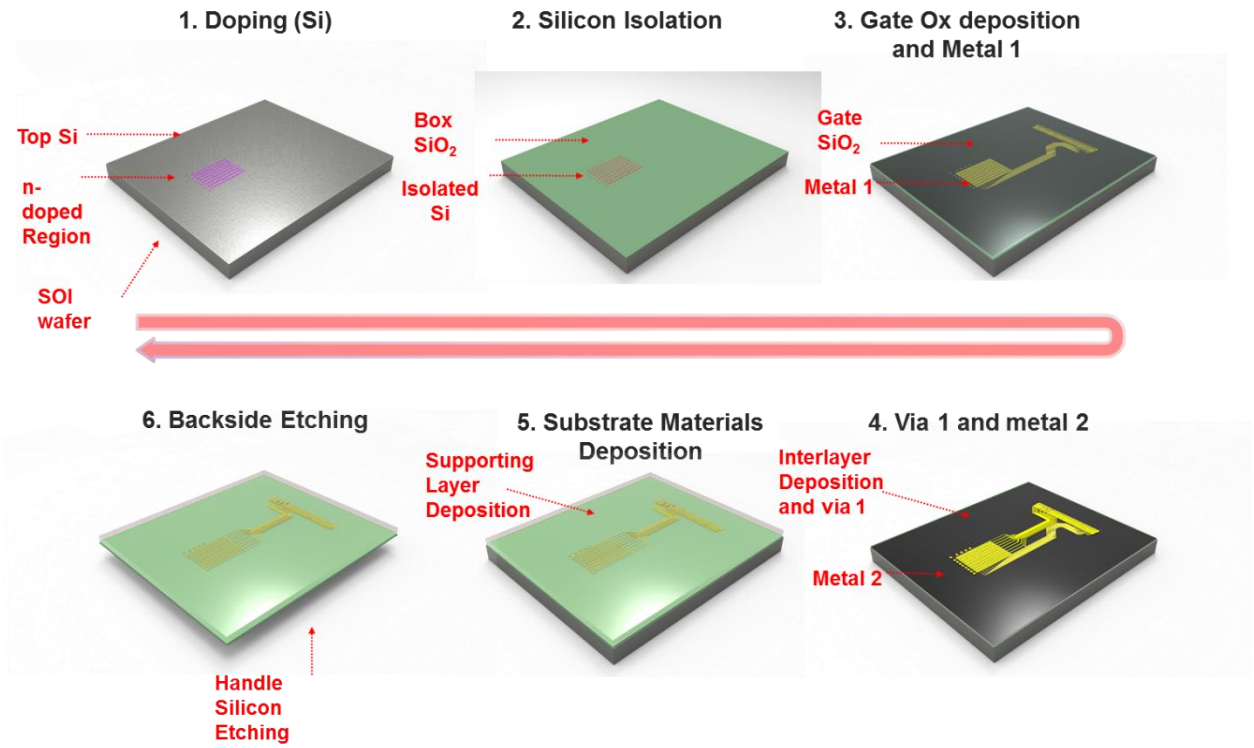

Figure 8.1 Inverse fabrication process for active electrodes with SiO_2 encapsulation.

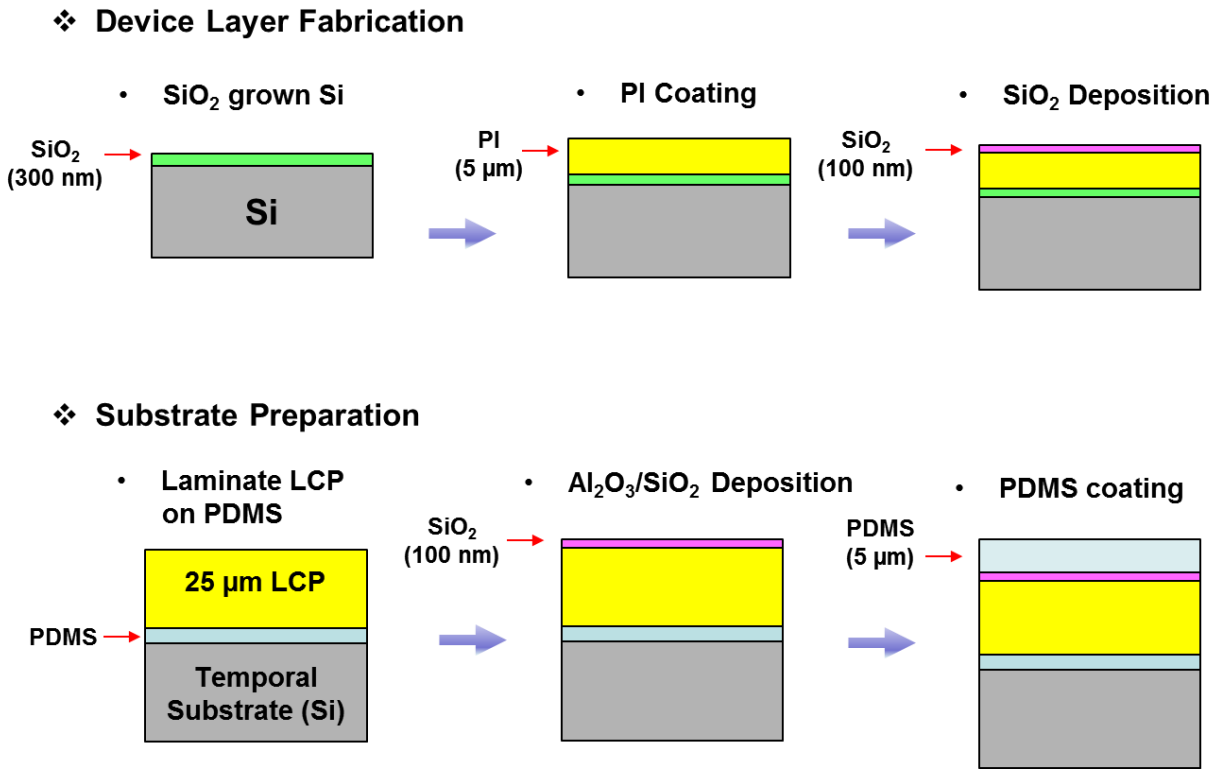

Figure 8.2 Detailed inverse fabrication steps include device fabrication and substrate preparation.

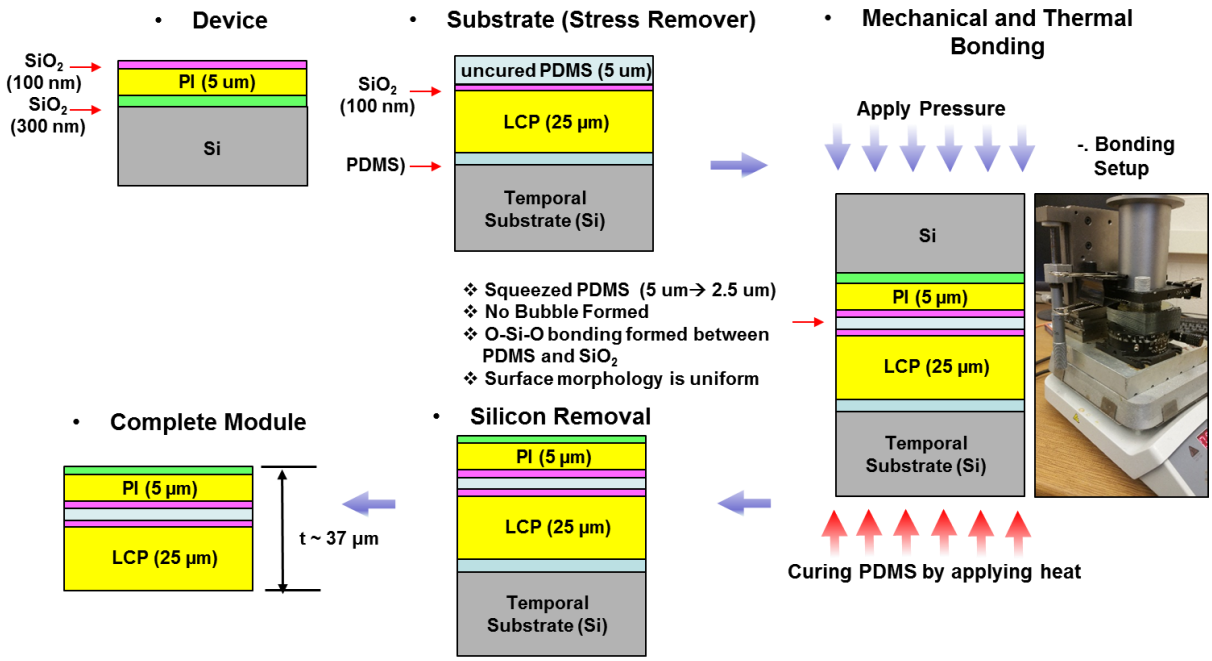

Figure 8.3 Mechanical and thermal bonding of the device and flexible substrate layers.

a)

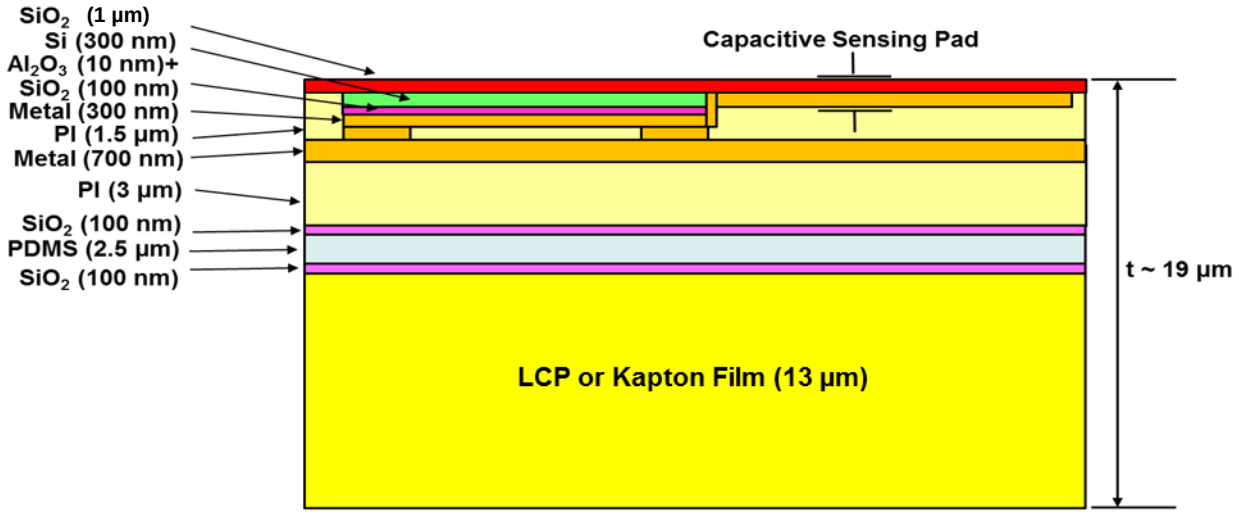

b)

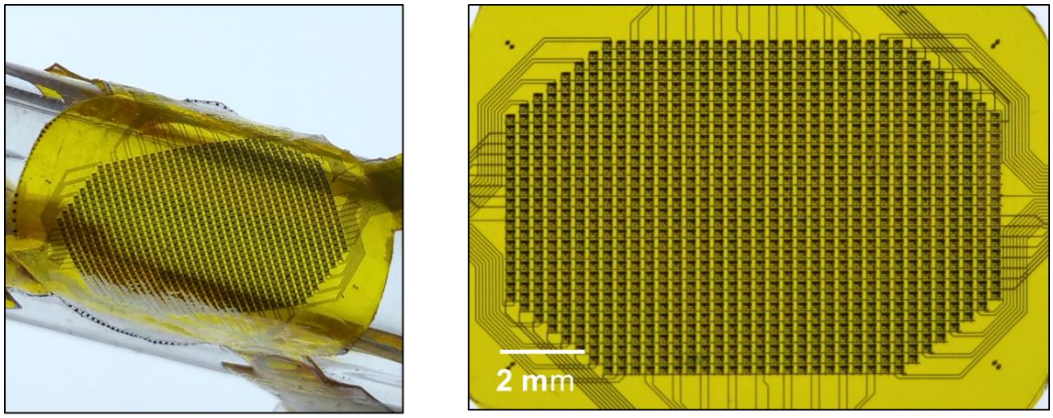

Figure 8.4 (a) Cross-section of 64-ch active, capacitive electrode array. (b) Photographs of 1,040-ch actively multiplexed neural array.

a)

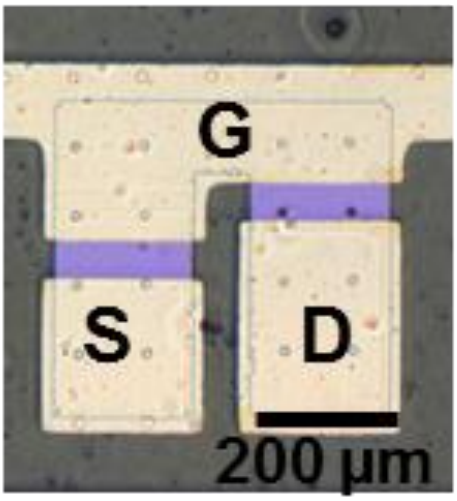

b)

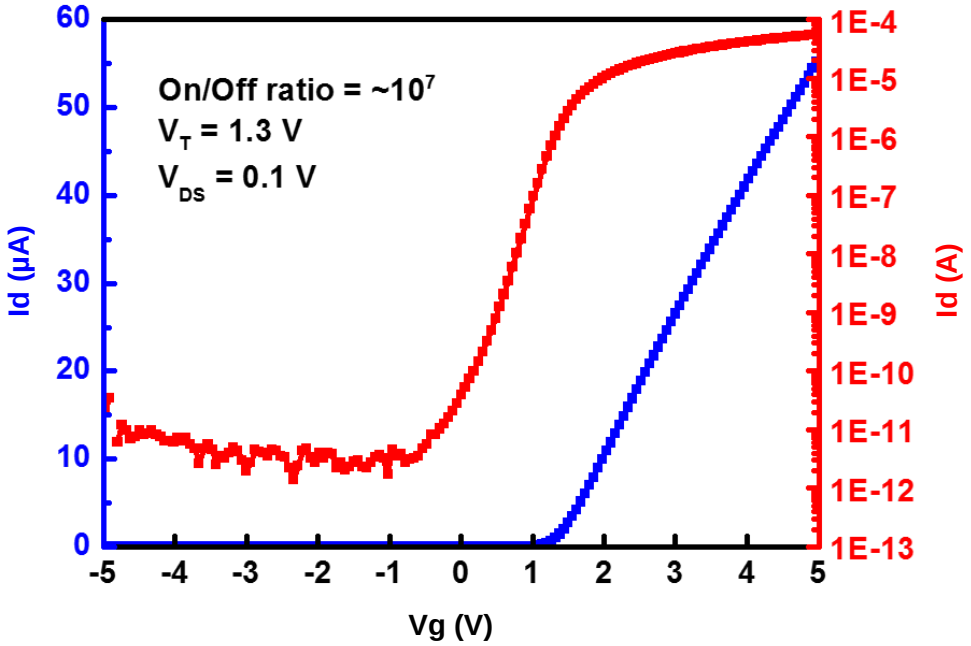

Figure 8.5 (a) Optical image of n-channel MOSFET. (b) The left frame shows linear (red) and log scale (blue) transfer curves for a representative n-channel MOSFET, for Vg swept from −5 to +5 V. The channel length (Lch), and width (W) are 20 µm and 200 µm, respectively. The threshold voltage, mobility and on/off ratio are 1 V, 350 $cm^2/V \cdot s$ and ~10^7, respectively.

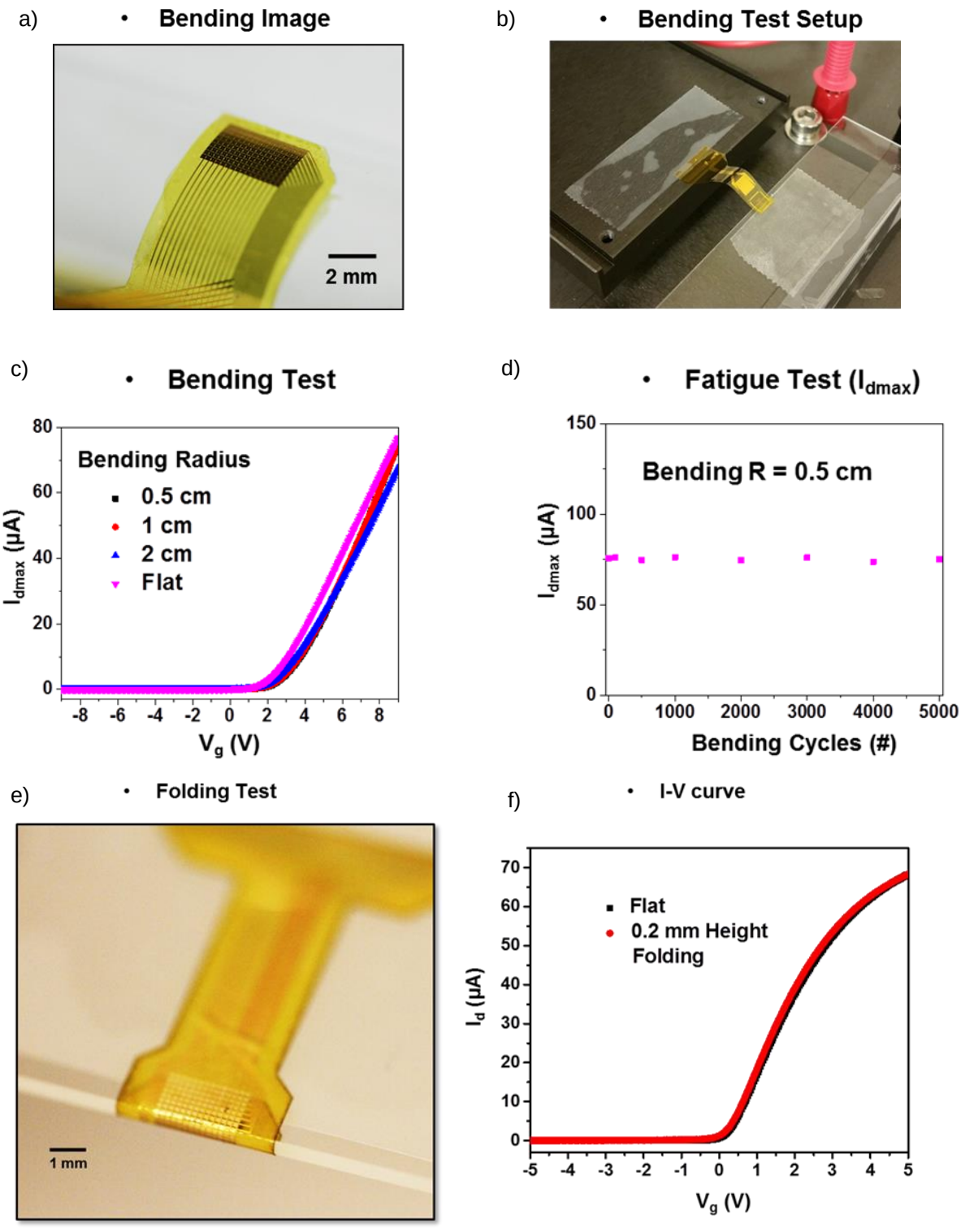

Figure 8.6 Photographs of (a) electrode array wrapped around a glass rod with a 1 cm bending radius, and (b) mechanical fatigue testing. (c) Plot of I-V curves of transistor with different bending radius. (d) Plot of Idmax vs bending cycles. (e) A photograph of electrode folded around a 0.9 mm thick glass. (f) Plot of I-V curves before and after folding.

➢ Test device structure:

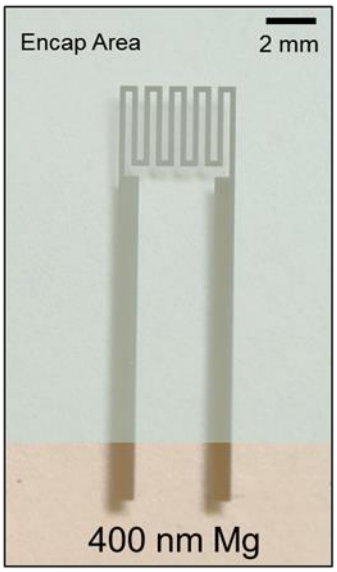

➢ Material combinations:

1. Al_2O_3 (40 nm)/ BCB (1 µm)
2. HfO_2 (40 nm)/ BCB (1 µm)
3. Al_2O_3 (40 nm)/ Parylene (1 µm)
4. HfO_2 (40 nm)/ Parylene (1 µm)
5. Al_2O_3 (40 nm)/ PI (1 µm)
6. HfO_2 (40 nm)/ PI (1 µm)
7. Al_2O_3 (40 nm)/ BCB (300 nm)/Al_2O_3 (40 nm)/ BCB (300 nm)/Al_2O_3 (40 nm)/ BCB (300 nm)
8. HfO_2 (40 nm)/ BCB (300 nm)/HfO_2 (40 nm)/ BCB (300 nm)/HfO_2 (40 nm)/ BCB (300 nm)
9. Al_2O_3 (40 nm)/ PI (300 nm)/Al_2O_3 (40 nm)/ PI (300 nm)/Al_2O_3 (40 nm)/ PI (300 nm)
10. HfO_2 (40 nm)/ PI (300 nm)/HfO_2 (40 nm)/ PI (300 nm)/HfO_2 (40 nm)/ PI (300 nm)
11. PI (1 µm)
12. Al_2O_3 (40 nm)
13. HfO_2 (40 nm)
14. Polysiloxane (750 nm)
15. *Transferred thin thermal SiO_2*

Figure 8.7 Screening different encapsulation strategies. Encapsulation test structures were initially screened by soaking in PBS solution with pH 7.4 @ 37 ℃.

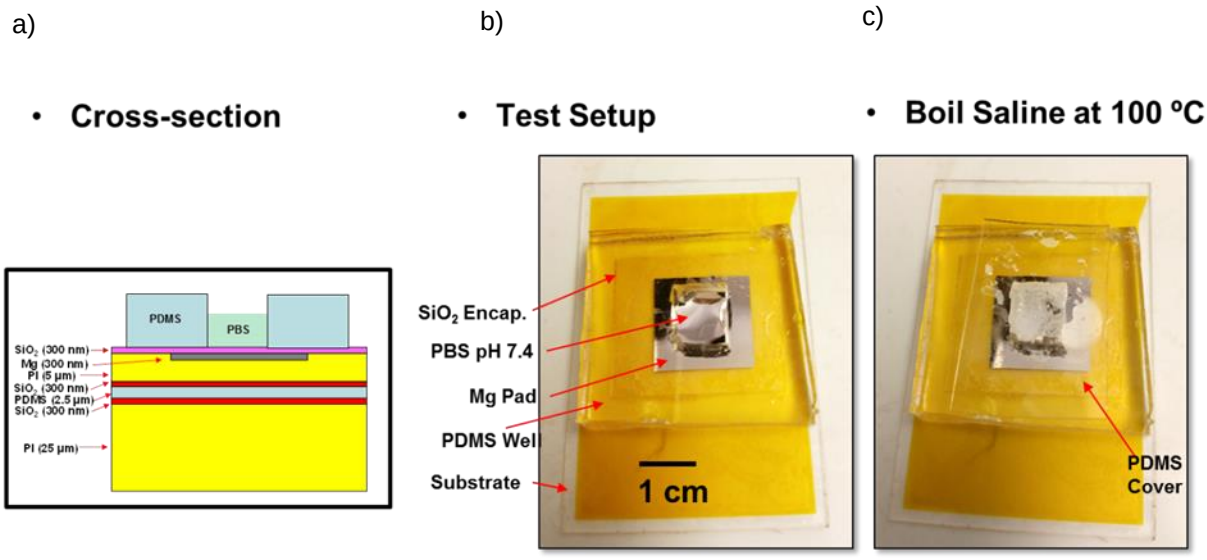

Figure 8.8 Mg soak test with PDMS well. (a) Cross section of encapsulation test device with deposited Mg film. (b) A PDMS well is formed on the surface of the device to hold saline. (c) The entire structure is heated to rapidly age the encapsulation and search for signals of failure. Dissolution of the Mg indicates that the encapsulation has failed.

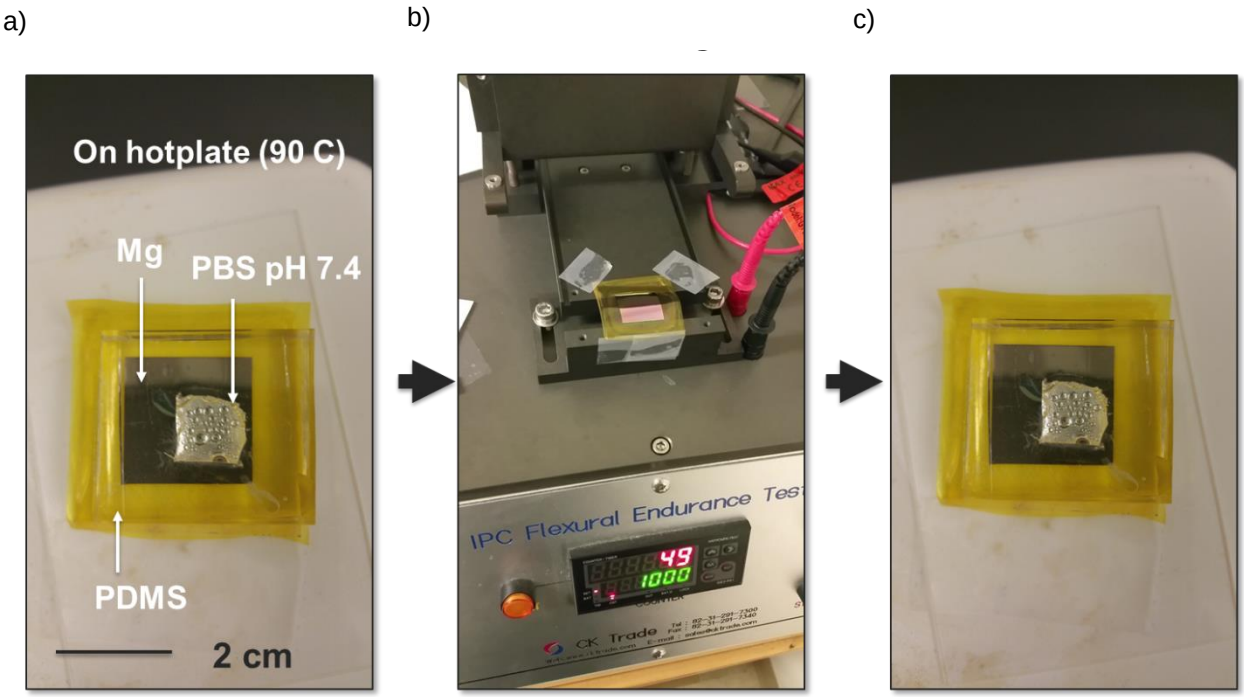

Figure 8.9 (a) Mg soak test with PDMS well at high temperature before mechanical testing. (b) 1000 cycles of mechanical fatigue testing. (c) Mg soak test again with the same conditions after mechanical testing.

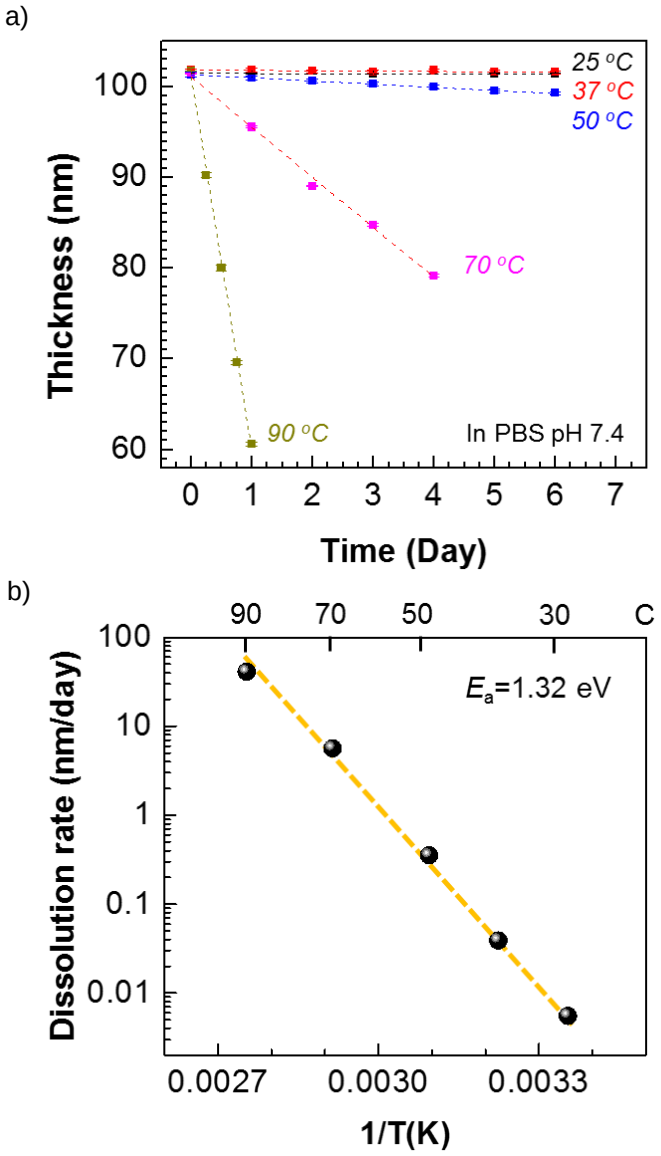

Figure 8.10 Results of dissolution kinetics of SiO_2. (a) Dissolution rate of SiO_2 with different temperature. (b) Experimental and fitting results based on the Arrhenius equation.at different temperatures.

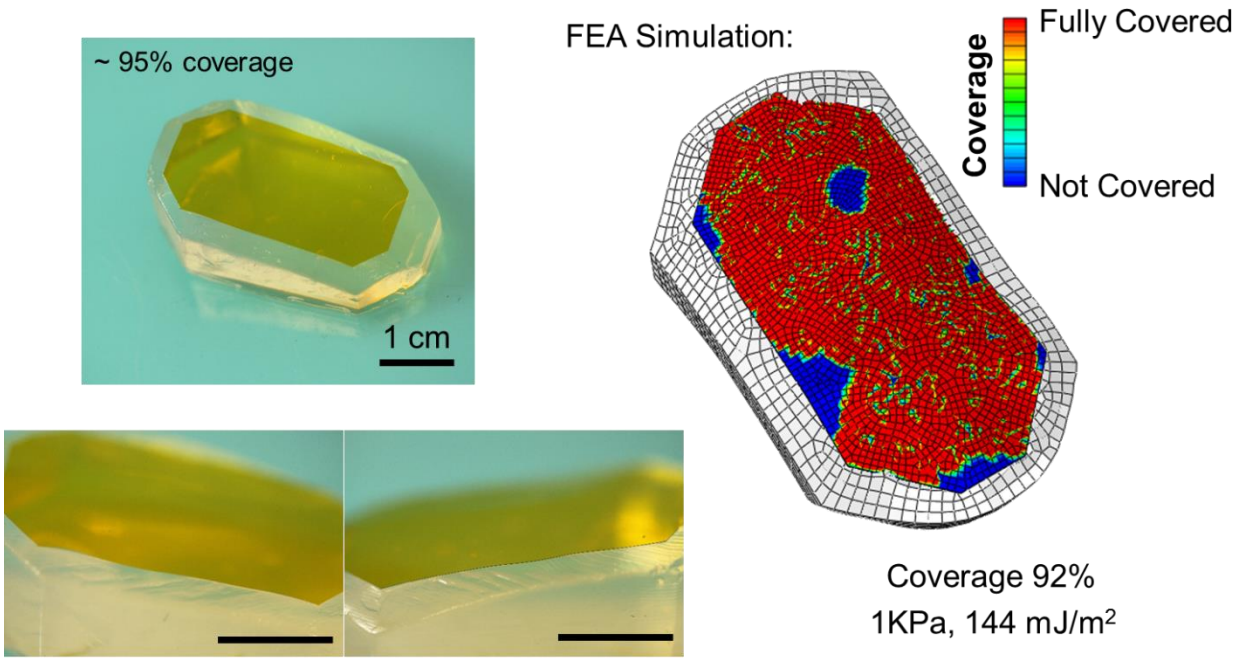

Figure 8.11 Mechanical modeling of large-area polyimide arrays laminating to the surface of brain models. (Left) Polyimide mockups laminating to a soft brain model derived from NHP MRI data. (Right) Computational modeling of the same electrode array geometry on a mechanical model of brain tissue. Some additional deformability in the electrode array design may be required to enable complete cortical surface coverage over the 3×2 cm^2 brain area.

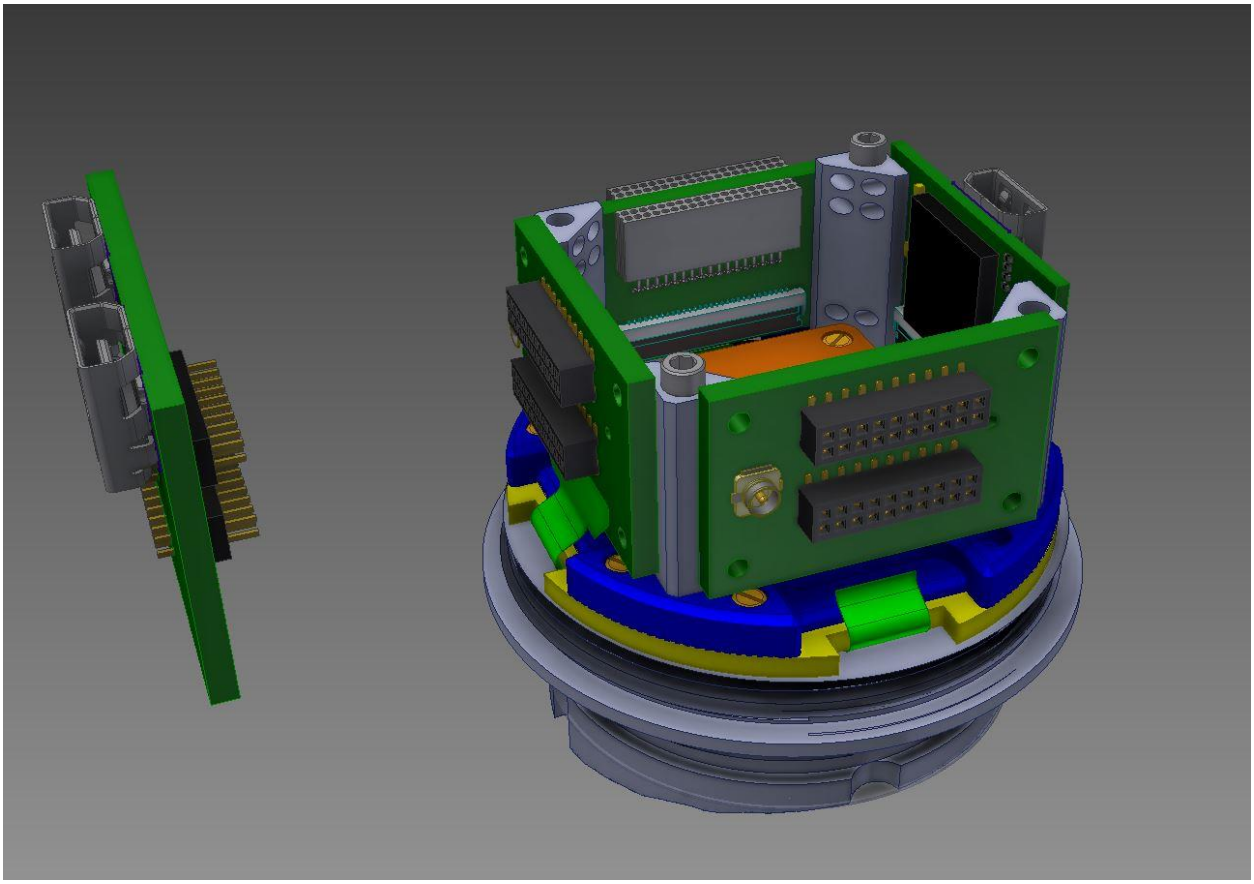

Figure 8.12 NHP Recording chamber with PCBs and adapters for 1,040-ch active electrode arrays.

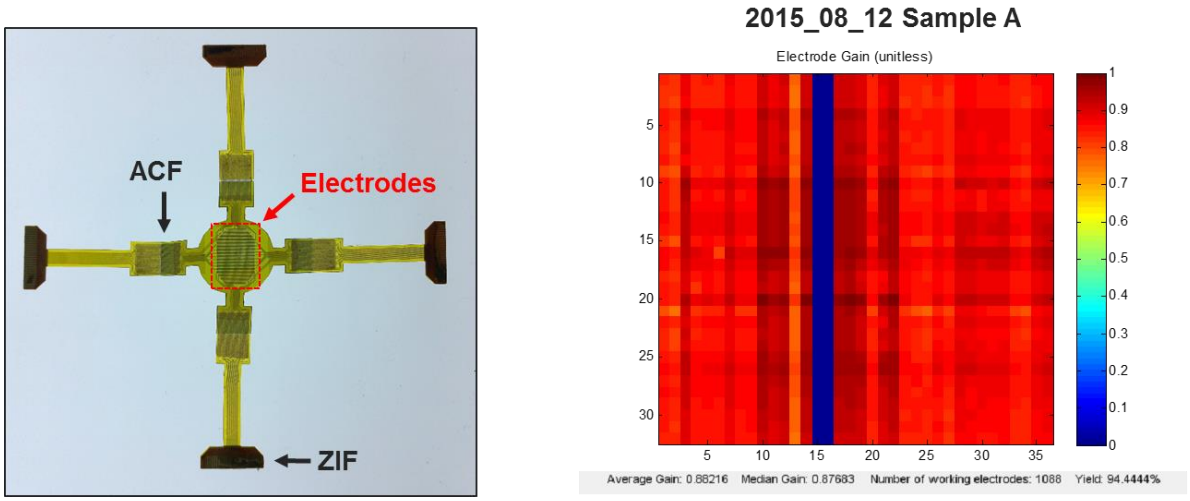

Figure 8.13 (a) An optical image of 1,040-ch active electrode array. (b) Color map illustrating the spatial distribution of the electrode response, demonstrating the spatial uniformity of the gain of an actively multiplexed, bioresorbable electrode array and leakage current over time.

8.6 References

[1] J. Du, T. J. Blanche, R. R. Harrison, H. A. Lester, S. C. Masmanidis, PLoS ONE **6**, e26204 (2011).

[2] D. R. Kipke, IEEE Transactions on Biomedical Engineering **51**, 896–904 (2004).

[3] P. J. Rousche and R. A., Normann, the Journal of Neuroscience Methods **82**, 1–15 (1998).

[4] E. Castagnola *et al*., *2013 6th International IEEE/EMBS Conference on. IEEE*, 2013.

[5] K. Matsushita *et al*., *Engineering in Medicine and Biology Society (EMBC)* (2013 35th Annual International Conference of the IEEE. IEEE, 2013).

[6] A. A. Schendel *et al*., Journal of neural engineering **11**, 046011 (2014).

[7] B. Rubehn, P. Fries, and T. Stieglitz, *4th European Conference of the International Federation for Medical and Biological Engineering* (Springer Berlin Heidelberg, 2009).

[8] C. Guillaume *et al*., *Engineering in Medicine and Biology Society (EMBC)* (2012 Annual International Conference of the IEEE. IEEE, 2012).

Chapter 9. OUTLOOK

Even though many new materials hold significant promise, opportunities continue to exist for Si electronic systems. In this regard, we have demonstrated the ability to develop unconventional types of ultrathin Si electronics by novel techniques. With the results from this thesis, ultrathin Si electronics can be fabricated into versatile modules with high performance and large scale that are not only flexible, but also stretchable. In this thesis, three types of new devices (photovoltaics, strain gauge, and electrocorticography (ECoG) sensor) are introduced in terms of applications, all based on the usage of ultra-thin single-crystalline Si as an active material. These specific applications are a result of their micro- and nanoscale design combined with the ability to manipulate the material, in a practical way, by using transfer printing and back-etching techniques. Collectively, the results show that the materials, design layout and performance are suitable for the fabrication of unconventional high-performance Si electronics, which cannot be achieved with conventional wafer-based electronics. Further investigation of ultrathin Si electronics will follow, and there will be many new and interesting discoveries as research in this area continues.